

Medizinische Fakultät der
Universität Duisburg-Essen

Aus der Abteilung Hochfeld und Hybride MR Bildgebung

Development and evaluation of new methods for the extension of clinical applications in PET/MR hybrid imaging

Inaugural-Dissertation

zur Erlangung des Doktorgrades

der Naturwissenschaften in der Medizin

durch die Medizinische Fakultät
der Universität Duisburg-Essen

Vorgelegt von

Maike Elisabeth Lindemann

aus Gladbeck

2020

Dekan:	Herr Univ.-Prof. Dr. med. J. Buer
1. Gutachter:	Herr Univ.-Prof. Dr. rer. medic. H. H. Quick
2. Gutachter:	Herr Univ.-Prof. Dr. med. Ch. Rischpler
3. Gutachter:	Herr Priv.-Doz. Dr. med. H. Kühl

Tag der mündlichen Prüfung: 4. November 2020

List of publications

The work on this dissertation thesis resulted in the following peer reviewed journal publications

- **Lindemann ME**, Guberina N, Wetter A, Fendler WP, Jacoby B, Quick HH. *Improving ^{68}Ga -PSMA PET/MRI of the prostate with un-renormalized absolute scatter correction.* J. Nucl. Med. (impact factor 6,7). 2019; 60(11):1642-1648.
- **Lindemann ME**, Nensa F, Quick HH. *Impact of improved attenuation correction on ^{18}F -FDG PET/MR hybrid imaging of the heart.* PLoS One (impact factor 2,8). 2019; 14(3):1-16.
- **Lindemann ME**, Stebner V, Tschischka A, Kirchner J, Umutlu L, Quick HH. *Towards fast whole-body PET/MR: Investigation of PET image quality versus reduced PET acquisition times.* PLoS One (impact factor 2,8). 2018; 13(10):1-15.
- **Lindemann ME**, Oehmigen M, Blumhagen JO, Gratz M, Quick HH. *MR-based truncation and attenuation correction in integrated PET/MR hybrid imaging using HUGE with continuous table motion.* Med. Phys. (impact factor 2,9). 2017; 44(9):4559-4572.

Table of contents

List of publications	3
1 Introduction	6
1.1 PET/MR hybrid imaging	6
1.1.1 Magnetic resonance imaging	6
1.1.2 Positron emission tomography	7
1.1.3 PET/MR hybrid imaging	8
1.2 Challenges in PET/MRI	10
1.2.1 Attenuation correction	10
1.2.2 Scatter correction	13
1.2.3 Fast imaging	15
1.3 Aims of this thesis	17
2 Materials and methods	18
2.1 Improved AC: Implementation of HUGE truncation correction	18
2.1.1 AC-map processing	18
2.1.2 Phantom measurements	20
2.1.3 Patient measurements	21
2.2 Improved AC including HUGE and bone model: Clinical application . .	23
2.2.1 Image acquisition and reconstruction	23
2.2.2 Image analysis	25
2.3 Improved SC using un-renormalized absolute scaling on ⁶⁸ Ga-PSMA PET/MRI	26
2.3.1 Image acquisition and reconstruction	26
2.3.2 Image analysis	26
2.4 Fast PET/MRI: PET image quality vs. PET acquisition time	27
2.4.1 Image acquisition and reconstruction	27
2.4.2 Image analysis	28

3	Results	29
3.1	Improved AC: Implementation of HUGE truncation correction	29
3.1.1	Phantom measurements	29
3.1.2	Patient measurements	31
3.2	Improved AC including HUGE and bone model: Clinical application . .	39
3.2.1	Quantitative cardiac PET/MRI	39
3.2.2	AC-map artifacts	42
3.3	Improved SC using un-renormalized absolute scaling on ⁶⁸ Ga-PSMA PET/MRI	44
3.3.1	Image quality and quantification	44
3.3.2	Lesion detection	47
3.4	Fast PET/MRI: PET image quality vs. PET acquisition time	49
3.4.1	Image quality parameters	49
3.4.2	Correlation with image quality determinants	53
4	Discussion	56
4.1	Attenuation correction	56
4.1.1	CT as a reference	56
4.1.2	HUGE truncation correction	57
4.1.3	MLAA truncation correction	60
4.1.4	Bone correction, artifacts and BMI	60
4.2	Scatter correction	62
4.2.1	Image quality and quantification	62
4.2.2	Lesion detection	64
4.3	Fast imaging	65
4.3.1	Decreased PET image quality	65
4.3.2	Correlation with image quality determinants	66
4.3.3	Dose reduction	67
5	Conclusions	69
6	Outlook	71
	Summary/Zusammenfassung	72
	References	74
	List of figures	90
	List of tables	91

1 Introduction

Since the introduction of the first clinical positron emission tomography (PET)/computed tomography (CT) in 2010 with simultaneously acquired data [Beyer et al., 2000], hybrid imaging became a success story. Nowadays, the combination of CT and PET is commonly used in clinical routine and presents an important part in diagnostic imaging. While the main application of CT is distinguishing anatomical structures with high spatial resolution, PET is required to visualize functional processes and changes in the metabolism in the human body. Combining both modalities into one hybrid system, thus provides diagnostic synergies superseding standalone PET systems.

In contrast to CT, magnetic resonance imaging (MRI) offers an excellent soft tissue contrast without using ionizing radiation. The emerging interest in combining these two modalities, MRI and PET, into one hybrid imaging system is obvious. Over the last decade, numerous technical challenges combining PET and MRI into one hybrid system could be solved and PET/MRI could demonstrate the potential diagnostic advantages in oncology, neurology, cardiology and paediatric imaging over PET/CT [Catana et al., 2006; Pichler et al., 2008b,a; Beyer and Pichler, 2009; Pichler et al., 2010; Delso et al., 2011; Drzezga et al., 2012; Wiesmüller et al., 2013; Quick et al., 2013; Quick, 2014].

1.1 PET/MR hybrid imaging

1.1.1 Magnetic resonance imaging

MRI provides high spatial resolution images in the sub-millimetre range and allows for various different soft tissue contrasts without using ionizing radiation. The physical basis of MRI is the nuclear spin. A strong static magnetic field, the \mathbf{B}_0 field, aligns the spin magnetization. The spins precess within the main magnetic field. The frequency of precession is proportional to the magnetic field \mathbf{B}_0 and is denoted as resonance or Larmor frequency.

The resonance frequency ω_0 is described as follows, where γ is the gyromagnetic ratio [Hendrix and Krempe, 2003]:

$$\omega_0 = \gamma \mathbf{B}_0. \quad (1.1)$$

In the following the main magnetic field, which is conventionally orientated along the z -axis, is referred to as $\mathbf{B}_0 = (0, 0, B_0)$. For MR signal excitation an additional magnetic radio frequency field is needed to deflect the spins from their equilibrium and let them precess in-phase. A third time-varying magnetic field allows for the spatial encoding of the MR signal. Three linear space-dependent gradient fields overlay the B_0 field. The spatial encoding of MR signal with linear space-dependent gradient fields (\mathbf{B}_G) is described by:

$$\mathbf{B}_G = \mathbf{G}r, \quad (1.2)$$

where r represents the position and $|\mathbf{G}|$ the gradient strength. Therefore, the resonance becomes space-dependent. After excitation the spins return to their equilibrium due to spin-spin and spin-lattice interactions, thus the magnetization return to its basic state. This process is called relaxation.

In MRI the signal is related to proton densities of soft tissue and the tissue dependent relaxation behaviour of spins in magnetic fields. The resulting complex MR signal is spatially encoded by the gradient field and can be described as follows:

$$S(t) = \int d^3r \rho(\mathbf{r}) e^{-i(\gamma \mathbf{G}t)r}, \quad (1.3)$$

where $\rho(\mathbf{r})$ is the spin density distribution. Eq. 1.3 is simplified by neglecting relaxation effects and assuming a homogeneous B_0 field and perfect gradient linearity and only valid for rectangular gradient pulses. Consequences of inaccuracies cases, where hardware restrictions causes B_0 inhomogeneities and gradient non-linearities, are discussed in the next section.

1.1.2 Positron emission tomography

PET provides quantitative information about biochemical processes, metabolism and function of organs and cell regions with a spatial resolution of 3-5 mm.

The patient is injected with a radiotracer, which is a biological molecule labelled with positron emitting radioactive isotopes. The most commonly used tracer in PET/MR is 18-fluor-labeled fluorodeoxyglucose (^{18}F -FDG), glucose marked with the positron emitter ^{18}F . The glucose accumulates in tissue with a high glucose consumption like the brain, the heart and additionally in pathologic areas such as inflammations or lesions. A highly specific tracer is e.g.

68-gallium-labeled prostate-specific membrane antigen (^{68}Ga -PSMA). PSMA is a cell surface protein, which is expressed at higher levels in prostate cancer compared to other tissues.

The emitted positron of the tracer annihilates with an electron, whereby two annihilation photons with an energy of 511 keV are emitted at an angle of almost 180° . The photons are detected in coincidence by two independent detectors of the PET detector ring. The PET raw data, the detected coincidence events, are grouped into the projection directions, and thus stored into so-called sinograms [Townsend, 2004]. The PET image is reconstructed with a filtered back projection or an iterative expectation-maximization algorithm. Due to interactions with the surrounding tissue the photons may be attenuated and scattered on their way to the PET detector (Fig. 1.1) [Saha, 2005]. Data correction, such as attenuation correction (AC) and scatter correction (SC) are essential steps to obtain accurate and quantitative PET images.

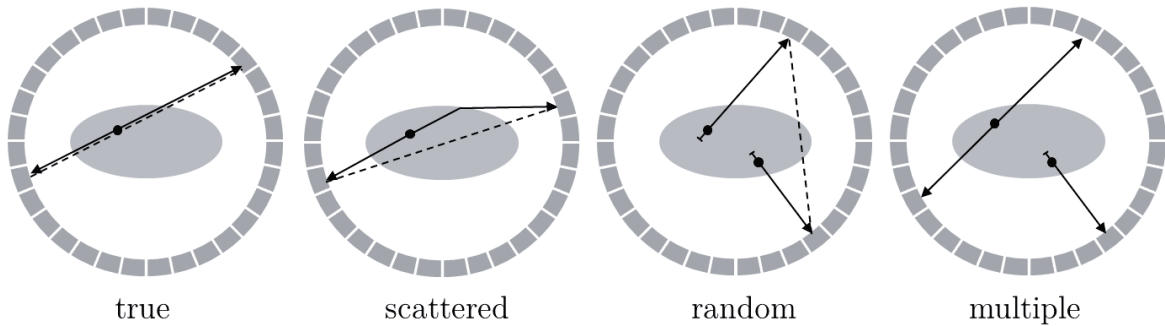


Fig. 1.1: Drawing of different coincidences detected by the PET detector ring. The dot symbolizes the position of photon annihilation, the arrows show the way of the two photons to the PET detector and the dotted line represents the resulting line-of-response. From left to right: true coincidence, scattered coincidence due to Compton interaction, random coincidence from different annihilations and multiple coincidence from three detected events. Note that only the true coincidences provide the true PET signal, while all other coincidences lead to bias in the true PET signal.

1.1.3 PET/MR hybrid imaging

The successful integration of MRI and PET into one whole-body PET/MR hybrid system with true simultaneous and independent PET and MRI data acquisition has shown great potential in various clinical applications over the last decade [Pichler et al., 2008b; Delso et al., 2011; Quick, 2014]. Especially the application fields of neuroimaging, cardiovascular imaging, whole-body oncology and prostate cancer benefit from PET/MR hybrid imaging [Boss et al., 2010; Bisdas et al., 2013; Rischpler et al., 2013;

Nensa et al., 2013; Schwenzer et al., 2012; Drzezga et al., 2012; Bouchelouche et al., 2010; Wetter et al., 2013]. Fig. 1.2 shows images from a whole-body PET/MRI examination.

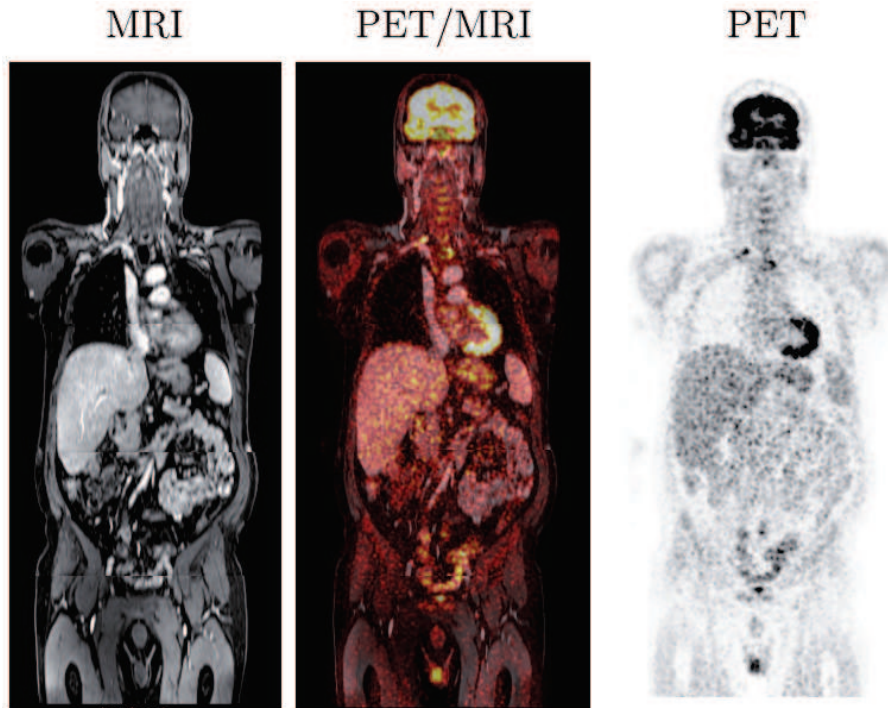


Fig. 1.2: Coronal images from a whole-body PET/MRI examination of a patient with bronchial carcinoma. For MR a T1-weighted VIBE MR sequence was used (left). Corresponding ^{18}F -FDG PET images (right) and PET/MR fusion images (middle) are given. The resulting hybrid image provides an anatomic map with high spatial resolution and high soft tissue contrast (provided by MRI) as well as a map of radiotracer distribution and metabolic information (provided by PET).

To fully integrate both systems, MRI and PET, several hardware and software solutions had to be developed. Conventional PET detectors without technical modifications are significantly affected by the strong magnetic and electromagnetic fields of the MRI. Photomultiplier tubes, which are often used in conventional PET, respectively PET/CT, detectors, are highly sensitive to magnetic fields. Replacing the photomultiplier tubes in the PET detectors with avalanche photo-diodes, which are insensitive to magnetic fields, was an essential step on the hardware side to combine both modalities [Pichler et al., 2006, 2008b].

Besides the hardware integration of MRI and PET into one system, MR-based AC of PET data is an additional technical challenge [Mehranian et al., 2016]. AC of PET data is an essential step in obtaining accurate and quantitative PET data.

In PET/CT, the CT values can be directly converted to linear attenuation coefficient (LAC) at 511 keV by a bilinear conversion [Kinahan et al., 2003; Carney et al., 2006]. In contrast to this established method, the MR signal is related to proton densities and spin relaxation, but not electron densities, and hence does not contain direct information of the photon attenuation magnitude. State of the art of MR-based AC in PET/MRI is a segmentation approach based on a Dixon-volumetric interpolated breath-hold examination (VIBE) MR sequence, which divides and segments the MR image into four tissue classes (background air, lung, fat and soft tissue) and assigns predefined LACs to the segmented tissue regions [Martinez-Möller et al., 2009]. The Dixon-VIBE approach works robust and provides reliable clinical results and is still established in clinical routine for AC in PET/MRI today. However, the Dixon-VIBE method has several limitations compared to CT-based as described in the next section [Beyer et al., 2016].

1.2 Challenges in PET/MRI

1.2.1 Attenuation correction

As described in section 1.1 the annihilation photons may be attenuated on their way to the PET detector due to additional MR hardware components (MR radiofrequency coils) in the PET gantry or the patients themselves. To achieve accurate quantitative PET imaging, it is essential to correct the attenuation of photons in human tissue. The attenuation correction factors (ACF) can be described as follows:

$$ACF = \exp \left\{ - \int \mu(r) dr \right\}. \quad (1.4)$$

The ACF for PET emission data are computed as the line of integrals of 511 keV photon attenuation μ along each line-of-response of the PET detector.

State of the art in PET/MRI is a segmentation approach for AC based on the Dixon-VIBE MR sequence [Martinez-Möller et al., 2009]. The established MR-based methods of creating AC-maps have certain limitations compared to CT-based AC, e.g. the substitution of bone as soft tissue, which may lead to a systematic underestimation in PET signal [Samarin et al., 2012]. Another constraint of MR-based AC is the limitation of the MR field-of-view (FOV) to a diameter of about 50 cm due to general hardware restrictions in MRI such as B_0 inhomogeneities and gradient non-linearities [Bakker et al., 1992]. Hence, truncation artifacts may occur at off-center positions and lead to bias in the entire AC-map, and thus in PET activity quantification [Delso et al., 2010]. In contrast to PET/CT, the majority of PET/MR patients were positioned with

arms along the body. Thus, truncation artifacts in PET/MRI frequently occur along the arms. However, several applications, e.g. quantitative cardiac perfusion imaging or MR-based radiotherapy treatment planning, require sufficient MR-based AC methods for accurate PET quantification even for very large MR FOVs [Rischpler et al., 2012; Tanner et al., 2000].

To provide AC for bone, a model-based bone segmentation approach including the LAC of the major bones (skull, spine, pelvis, upper femur) in the standard Dixon-VIBE AC-map was introduced [Koesters et al., 2016; Paulus et al., 2015]. The bone model is generated from a set of prealigned MR images and bone mask pairs for six major bones. After individual registration of the model to the Dixon-VIBE MR images of each patient, the major bones are then added to the Dixon-VIBE AC-map.

Regarding the FOV limitations of MRI, several methods have been explored to complement resulting truncation artefacts in the MR-based AC-map. One approach is based on joint estimation of emission and transmission data using the maximum likelihood estimation of activity and attenuation (MLAA) image reconstruction method, a PET-based method to calculate a truncation corrected AC-map [Nuyts et al., 1999, 2010]. This method assumes radiotracer uptake in the truncated parts of the arms to derive accurate body contouring from PET data and complements the truncated Dixon-VIBE AC-map with information from extended FOV. For the most commonly used radiotracer ^{18}F -FDG, this approach works robust and provides reliable results. A potential limitation of this method is that it requires unspecific radiotracer uptake in the skin. Thus, MLAA may fail in PET/MRI involving radiotracers, which has no unspecific radiotracer uptake, and precise contour detection based on PET data may not be possible.

A fully MR-based approach for truncation correction is B_0 homogenisation using gradient enhancement (HUGE), which optimizes the readout gradient to locally compensate the B_0 inhomogeneities, and thus the truncations [Blumhagen et al., 2013, 2014]. System specific field plots of the B_0 and the G_x fields are used to calculate a space-dependent optimal read-out (RO) gradient in x -direction (left-right) to reduce truncations and complement the Dixon-VIBE AC-map with information from extended FOV (Fig. 1.3).

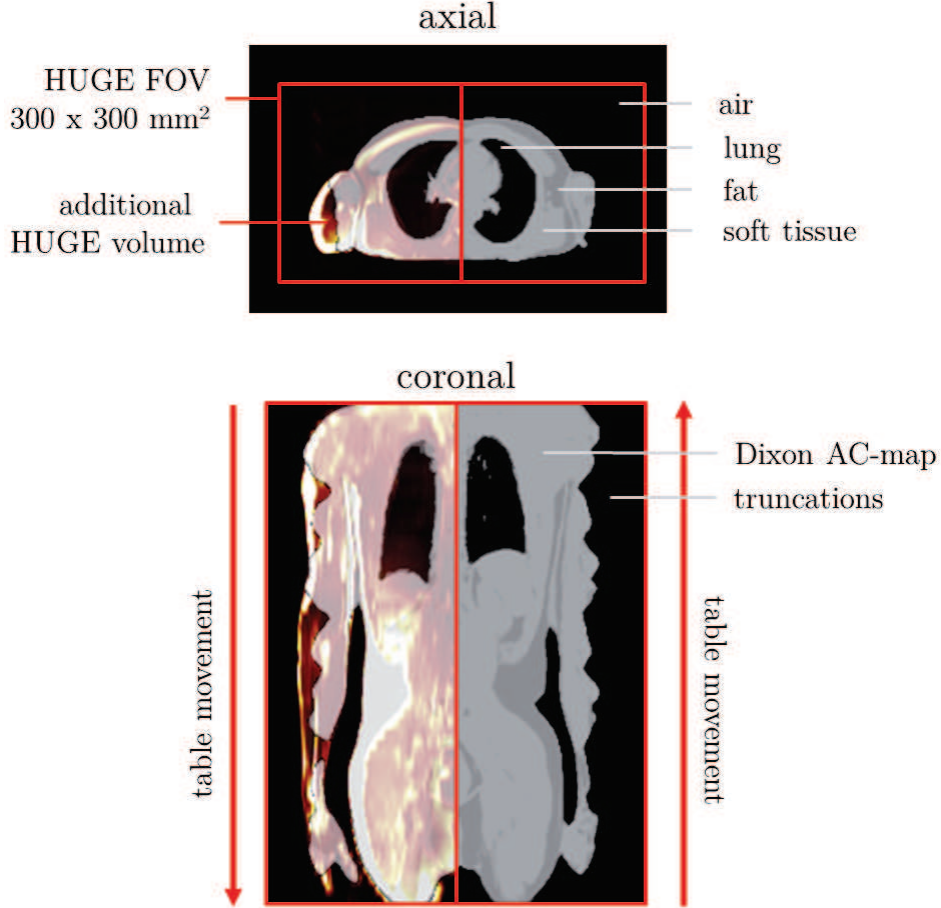


Fig. 1.3: Fused images in axial and coronal orientation of the Dixon-VIBE attenuation correction (AC) map and MR-based HUGE raw data from patient's right side (for demonstration purposes). The Dixon-VIBE AC-map provides segmentation into four tissue classes and shows truncation along the arms, where the patient's anatomy exceeds the constraints of the regular MR field-of-view (FOV). Note the added body volume along the arms when applying HUGE. HUGE uses continuous table motion in a two-step head-to-feet and back acquisition to acquire non-truncated data from the patient's left and right side with a FOV of 300 mm² in axial orientation resulting in a lateral (left-right) FOV coverage of 600 mm.

In a 2-dimensional spin-echo MR sequence the distorted pixel position x' in x -direction can be described as follows:

$$x' = x + \frac{\Delta B_{G_x}(x, y, z)}{G_x} + \frac{\Delta B_0(x, y, z)}{G_x}, \quad (1.5)$$

where x is the original pixel position, ΔB_0 represents the inhomogeneity of the main magnetic field, ΔB_{G_x} is the non-linearity of the gradient field and G_x describes the applied read-out gradient strength.

Based on Eq. 1.5, a space-dependent optimal read-out gradient can be calculated as follows:

$$G_{\text{RO,opt}}(x, y, z) = -\frac{\Delta B_0(x, y, z)}{c(x, y, z)}, \quad (1.6)$$

where $c(x, y, z) = \Delta B_{G_x}(x, y, z)/G_x$ is the relative error of the gradient field [Bakker et al., 1992]. This optimal read-out gradient compensates the total distortion, thus x' is equal to x . Blumhagen et al. [2013] showed that applying this optimal read-out gradient significantly reduces distortion. Therefore, the MR-based HUGE method has great potential to extend the MR FOV, and thus improves MR-based AC [Blumhagen et al., 2014].

The optimal read-out gradient is space dependent and may differ for every voxel position (Eq. 1.6). Blumhagen et al. [2013] showed that applying a single optimized read-out gradient for each patient side (left and right) and slice position with a multi-slice spin-echo-based implementation of the HUGE method was sufficient to significantly reduce distortion and extend the MR FOV. As a basis for calculation, HUGE uses PET/MR system specific (Biograph mMR, Siemens Healthcare GmbH, Erlangen, Germany) field plots of B_0 inhomogeneities ΔB_0 of the main magnet field and the non-linearities of the gradient field $c(x, y, z)$, which were previously measured once with a MR probe device [Blumhagen et al., 2013]. The actual implementation of HUGE used in this thesis was based on a modified half Fourier acquisition single shot turbo spin-echo (HASTE) spin-echo MR sequence proposed by Blumhagen et al. [2014]. The optimal gradient amplitude corresponding to zero-distortion applies automatically and successfully extends the MR FOV to 60 cm in x-direction (left-right). Each slice has to be acquired twice separately to optimize for both left and right side. An adapted version of HUGE is combined with continuous table movement (CTM), such that MR data is always acquired in the most homogeneous region of the magnet iso-center, where also the gradients provide best linearity [Braun et al., 2012, 2014]. The patient is moved continuously through the optimized slice at the iso-center, thus the magnitude of distortion does not vary with slice position and data acquisition is very effective.

1.2.2 Scatter correction

Due to interactions with the surrounding tissue, the photons may be attenuated and scattered on their way to the detector. The contribution of scattered events can yield 40 to 60 % of the total detected coincidences [Salomon et al., 2011]. To achieve accurate and quantitative PET images it is essential to correct these scattered events. The most common utilized SC method in clinical PET is the model-based single Compton

scatter simulation (SSS) [Watson et al., 1997; Watson, 2000]. This SC method uses the attenuation map obtained from a transmission scan, the emission data and a model of the system geometry to calculate the percentage of events, for which one photon has undergone a single Compton interaction. The main drawback of this method is an inability to correct for scatter events originating from radioactivity outside the FOV. SC algorithms in PET/MR hybrid imaging, thus, rely on an accurate AC-map of the patient tissues. Especially the truncations along patients' arms might be an important factor on the accuracy of SC [Afshar-Oromieh et al., 2017; Noto et al., 2017].

Recently, there is a high interest in ^{68}Ga -PSMA PET for staging, therapy and follow-up of prostate cancer [Afshar-Oromieh et al., 2016; Eiber et al., 2016; Schwarzenboeck et al., 2017]. Several studies showed promising results in the detection of prostate cancer using ^{68}Ga -PSMA with PET/CT [Afshar-Oromieh et al., 2015; Eiber et al., 2015a; Schwenck et al., 2017], and also PET/MRI [Afshar-Oromieh et al., 2014; Eiber et al., 2015b; Lütje et al., 2016]. A challenge of using ^{68}Ga -PSMA ligand as a PET radiotracer is a frequently observed photopenic artifact in the PET images, the so-called halo artifact. PSMA barely accumulates in abdominal fat and soft tissue. Most ^{68}Ga -PSMA is excreted by the urine, and thus concentrated within the urinary tract. Consequently, there are severe differences in activity concentration between the bladder/kidneys and surrounding background tissue. This may cause the halo artifact in PET/CT [Rauscher et al., 2016], but particularly in PET/MRI [Afshar-Oromieh et al., 2014; Lütje et al., 2016]. The halo artifact causes reduced signal intensity around the urinary bladder and at the level of the kidneys in scatter corrected PET images. Due to the PET signal extinctions, lesions in these artifact regions may be undetectable or may result in distorted SUVs, hampering accurate quantification of lesion activity. The halo artifact is caused by improper SC, and thus an optimized SC is important to reduce the presence of the halo artifact and ensure accurate PET image quality and quantification in ^{68}Ga -PSMA PET/MRI of the prostate (Fig. 1.4) [Afshar-Oromieh et al., 2014; Heußer et al., 2017; Lütje et al., 2016].

The implementation of SSS for highly specific PET tracers such as ^{68}Ga -PSMA results in scatter overestimation, which causes the halo artifact to be frequently observed in ^{68}Ga -PSMA PET/MRI. The absolute scaling of SSS seems to be less prone to the halo artifact than relative scaling [Heußer et al., 2017]. PET SC typically uses a SSS to compute a scatter sinogram, which is scaled to the emission data to account for multiple and possible external scatter from outside the system's FOV. Eliminating the sometimes problematic renormalizing (rescaling) of the PET emission image during the SC calculations for tracers like ^{68}Ga -PSMA, potentially minimizes the appearance of the halo artifact, and thus improve diagnostic image quality and PET quantification.

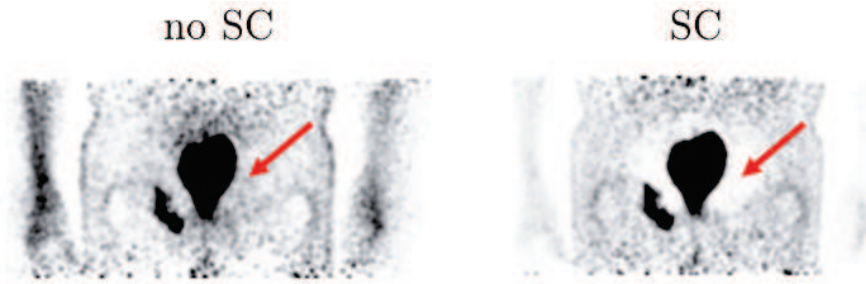


Fig. 1.4: Coronal ^{68}Ga -PSMA PET images of the pelvis of a patient example reconstructed without and with scatter correction (SC). In the scatter corrected PET images (single Compton scatter simulation with absolute scaling) a signal drop-out around the bladder, the so-called halo artifact, is observable. Non-SC images show no halo artifact, but lesions might be missed out and a quantitative assessment of radiotracer uptake is impossible.

1.2.3 Fast imaging

An inherent advantage of PET/MR over PET/CT is that MR provides a wide range of excellent soft tissue contrasts and potentially adds diagnostic information complementary to the PET data. However, in most PET/MR imaging protocols this comes at the cost of considerably increased PET/MR acquisition times when compared to PET/CT. MR requires the acquisition of multiple different imaging sequences (e.g. T1, T2, diffusion weighted imaging) to generate a choice of soft tissue contrasts per bed position. PET/CT data acquisition takes approximately 2 minutes per bed position with PET being the time limiting factor. Standard clinical whole-body MR protocols in PET/MRI today can last between 5–10 minutes per bed position or even longer depending on the clinical indication (Fig. 1.5). Rather lengthy MR protocols have been identified as the time limiting factor in PET/MRI [Drzezga et al., 2012; Quick et al., 2013; Wiesmüller et al., 2013].

The prolonged acquisition time has been identified as a main limitation of PET/MRI over PET/CT reducing patient comfort and patient throughput [Gückel et al., 2015]. Thus, shortening the PET/MR examination time and optimizing the workflow has been a subject of recent PET/MR studies [Grueneisen et al., 2015b, 2016, 2017; Kirchner et al., 2017b,a; Schwenzler et al., 2016].

In these studies, MR contrast weightings providing only redundant diagnostic information have been eliminated from the list of MR protocols while maintaining diagnostic information in specific clinical settings. Thus, in these updated fast whole-body PET/MR protocols the acquisition time per bed station could be reduced to 3 to 5 minutes, and therefore might be in the scope of PET being the time limiting factor in PET/MRI.

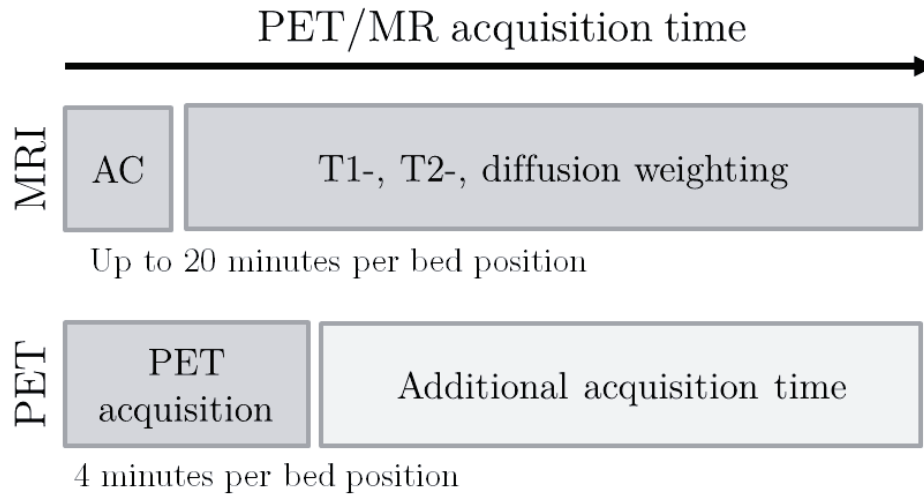


Fig. 1.5: Flow chart of simultaneous multi-step PET/MR data acquisition. Typically five bed positions are needed for a whole-body PET/MR examination. A standard MR protocol consists of a localizer, MR sequences for attenuation correction (AC) and MR sequences with different contrast weightings depending on the clinical indication. MR acquisition time will last up to 20 minutes per bed position. PET data will be acquired for approximately 4 minutes per bed position. Rather lengthy MR protocols are currently the time limiting factor in PET/MRI.

The ultimately fast PET/MR examination protocol was proposed by Eiber et al. [2011]. In this experimental study, the MR-based AC images were also used for clinical assessment without acquisition of further diagnostic MR sequences. The Dixon-VIBE MR images were used as anatomic correlate to the simultaneous PET data. Such an ultra-short PET/MR examination theoretically could only take 19 seconds per bed position and provides comparable results to a low-dose PET/CT examination [Eiber et al., 2011]. The diagnostic information gained from such a fast examination is, however, debatable. In this context and in preparation of future fast whole-body PET/MR imaging protocols PET might be the time limiting factor in PET/MRI and, consequently, the question arises whether short PET acquisition protocols allow for reduced acquisition time while providing adequate PET image quality and accurate PET quantification.

1.3 Aims of this thesis

The overarching aim of this thesis was the development and evaluation of new methods and imaging concepts to extend the clinical application spectrum in PET/MRI.

The first specific aim of this thesis deals with the implementation and subsequent evaluation of a MR-based truncation correction method called HUGE combined with continuous table motion to improve MR-based AC in whole-body PET/MRI. Optimized read-out gradients in x -direction (left-right) are used to reduce distortions at the extended MR FOV, and thus, reduce truncation artifacts in the resulting AC-map. The impact of the HUGE method on PET quantification was systematically tested in phantom measurements and subsequently in 24 whole-body PET/MRI patient datasets using different radiotracers. Various image quality and quantification parameters were systematically evaluated.

Especially in the context of quantitative cardiac perfusion PET/MRI a precise MR-based AC-map is important. Thus, to further extend the clinical application spectrum in PET/MRI, the second aim of the thesis was to evaluate the effect of improved MR-based AC including latest methods for truncation correction with HUGE and an additional bone segmentation approach on 32 ^{18}F -FDG cardiac PET/MRI patient datasets. The impact of improved AC was analysed for each cardiac segment.

The third aim of this thesis was to investigate the effect of improved SC on PET image quality and quantification in ^{68}Ga -PSMA PET/MRI of the prostate, evaluated in 100 patients with prostate cancer. Un-renormalized single Compton scatter simulation with absolute scaling was used to reduce the halo artifact around the bladder. Various image quality and quantification parameters were systematically evaluated.

In the context of preparing future fast whole-body PET/MRI protocols, the fourth aim of this thesis was to analyse the impact of reduced PET acquisition times on PET image quality and quantification. Therefore, the PET data of 51 patients with a whole-body PET/MR were retrospectively reconstructed into different time intervals to simulate reduced PET acquisition times. Various image quality and quantification parameters were systematically evaluated in whole-body ^{18}F -FDG PET/MRI data in this larger patient cohort.

2 Materials and methods

All PET/MR measurements in this thesis were performed on an integrated 3 Tesla whole-body PET/MR system (Biograph mMR, Siemens Healthcare GmbH, Erlangen, Germany). All studies in this thesis were conducted in conformance with the Declaration of Helsinki and approved by the Ethics Commission of the Medical Faculty of the University Duisburg-Essen. Patients provided written informed consent before examination. For AC of the patient tissues in all studies, the PET/MR acquisition protocol consists of a standard Dixon-VIBE MR sequence [Martinez-Möller et al., 2009]. Sequence parameters for the Dixon-VIBE were: image matrix $192 \times 126 \times 128$, resolution $2.6 \times 2.6 \times 3.1 \text{ mm}^3$, TE1 1.23 ms, TE2 2.46 ms, TR 3.6 ms, FA 10° , TA 19 s per bed position. The Dixon-VIBE MR images were divided into four tissue classes and assigned pre-defined LACs (background air 0.0 cm^{-1} , lung 0.0224 cm^{-1} , fat 0.0854 cm^{-1} and soft tissue 0.1 cm^{-1}) resulting in a standard Dixon-VIBE AC-map. All PET reconstructions in the presented studies were performed retrospectively with e7 tools (Siemens Molecular Imaging, Knoxville, USA) using the ordinary Poisson ordered-subsets expectation maximization (OP-OSEM) algorithm with 3 iterations, 21 subsets and 4 mm Gaussian filter. The resulting PET images have matrix dimensions of $344 \times 344 \times 127$ with a resolution of $2.09 \times 2.09 \times 3.01 \text{ mm}^3$ per bed position. For statistical analysis *t*-tests were performed. Calculated *p*-values < 0.05 were considered to be statistically significant.

2.1 Improved AC: Implementation of HUGE truncation correction

2.1.1 AC-map processing

Standard MR-based AC is based on the Dixon-VIBE MR imaging technique and subsequent tissue classification (sequence parameters see above) resulting in the Dixon-VIBE AC-map [Martinez-Möller et al., 2009]. The HUGE MR sequence combined with CTM is based on a modified HASTE sequence and was acquired separately for patients' left

and right side [Blumhagen et al., 2013, 2014; Lindemann et al., 2017]. Sequence parameters for HUGE were: image matrix 128×128 , resolution $2.3 \times 2.3 \text{ mm}^2$, 8 mm slice thickness in z -direction, TE 34 ms, TR 1610 ms, FA 180° , CTM with 27.4 mm/s. The HUGE AC-map is based on the Dixon-VIBE AC-map complemented with HUGE information from the extended FOV.

The completion of the truncated Dixon-VIBE AC-map with HUGE information from extended FOV is performed semi-automatically with Matlab R2013b (MATrix LABoratory, Mathworks, Natick, MA, USA). From HUGE raw MR data a binary mask was generated including the arms. Mask pixel values of 1 were assigned to the LAC of soft tissue. The extended HUGE AC-map was completed pixel-wise by fusing the Dixon-VIBE AC-map with segmented HUGE AC-map using landmark-based registration. The complete workflow to generate the extended AC-map with HUGE information is shown in Fig. 2.1 [Lindemann et al., 2017].

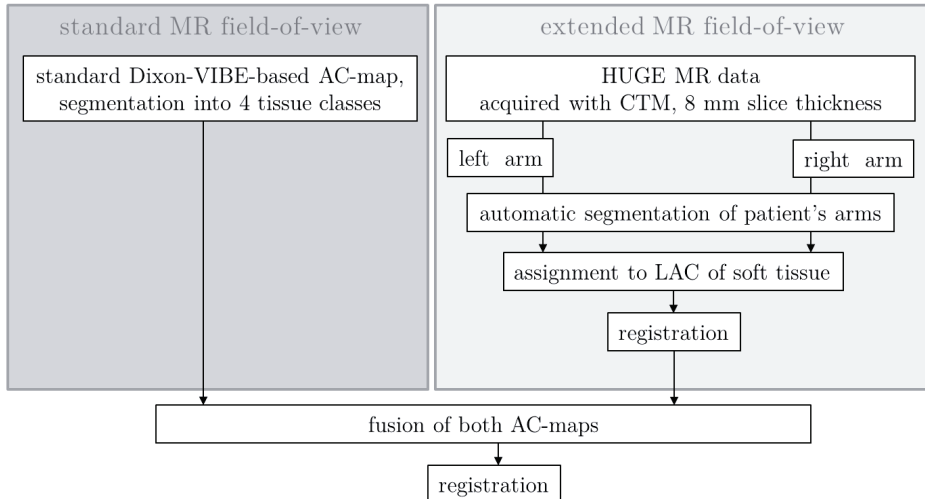


Fig. 2.1: Flow chart of the main steps for calculating the extended MR-based attenuation correction map (AC-map) from the standard Dixon-VIBE MR AC-map and HUGE raw data. HUGE is acquired with continuous table motion (CTM). The segmented HUGE raw data is assigned to a linear attenuation coefficient (LAC) of soft tissue [Lindemann et al., 2017].

For an intra-individual reference a MLAA AC-map was reconstructed. The PET-based MLAA approach assumes radiotracer uptake in the truncated parts of the arm to derive accurate body contours from PET data [Nuyts et al., 1999, 2010]. The activity and attenuation maps were reconstructed with one iteration and a single subset of the OSEM and 20 iterations and 9 subsets of MLAA algorithm. The matrix size of the completed AC-map was $344 \times 344 \times 127$ with a resolution of $2.09 \times 2.09 \times 2.03 \text{ mm}^3$ per

bed position. The MLAA AC-map is based on the Dixon-VIBE AC-map complemented with MLAA information from the extended FOV.

2.1.2 Phantom measurements

To systematically validate the impact of truncation correction using the HUGE method, NEMA image quality (IQ) phantom measurements were performed, which allows for standardized PET quantification [NEMA, 2007]. Two cylindrical arm phantoms (diameter 12.5 cm) were placed on the left and right side of the NEMA phantom. All phantoms were filled with MR-signal-producing fluid (5 g sodium chloride per 1000 ml distilled water) and placed on a low-attenuating Styrofoam block to ensure exact and reproducible repositioning. The phantom setup is shown in Fig. 2.2 [Lindemann et al., 2017].

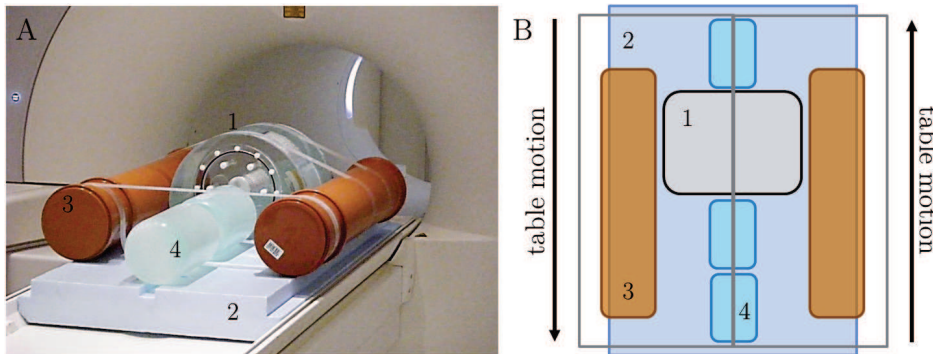


Fig. 2.2: Phantom setup consisting of a NEMA image quality phantom (1) on a Styrofoam positioning block (2) with two cylinders simulating arms (3) and additional MR signal adjustment bottles (4) (A). Draft of the phantom setup in coronal orientation (B). The two frames cover a lateral field-of-view of 300 mm for each side (left and right). HUGE is acquired with continuous table motion, the arrows display the direction of the table motion for both sides [Lindemann et al., 2017].

A CT-based AC-map including the NEMA phantom, the arm phantoms and the adjustment bottles was generated and served as a reference standard in this phantom study. The phantom setup was measured by a dual-source CT system (SOMATOM Definition Flash, Siemens Healthcare GmbH, Erlangen, Germany) with following parameters: energy 140 keV, tube current 400 mA, matrix 512×512 , resolution $0.3 \times 0.3 \times 0.5 \text{ mm}^3$. CT data was converted to PET energy level at 511 keV with a bilinear function using Matlab R2013b (MATrix LABORatory, Mathworks, Natick, MA, USA) [Kinahan et al., 2003; Carney et al., 2006]. For better comparability between CT- and MR-based AC the phantom housing was removed from the CT-based AC-map.

PET measurements were performed according to NU 2-2007 standard (sphere-background-ratio 8:1, 4 hot (injected with activity) spheres 10–22 mm and 2 cold (filled with water) spheres 28–37 mm, total activity 51.32 MBq and 12 min PET acquisition per bed position) [NEMA, 2007].

To validate the impact of truncation correction, PET data was reconstructed 4 times with different AC-maps: 1. CT AC serving as a reference, 2. Dixon-VIBE only, 3. Dixon-VIBE with additional HUGE truncation correction and 4. Dixon-VIBE with additional MLAA truncation correction. Region-of-interests (ROIs) in all PET reconstruction were placed as defined by the NEMA standard in all spheres and in the background [NEMA, 2007]. Signal-to-noise-ratio (SNR) and relative differences were calculated to quantify the impact of truncation correction. Statistical significance and *t*-test were performed.

2.1.3 Patient measurements

In this study, 23 patients with a whole-body ^{18}F -FDG PET/MRI and one patient with a whole-body 124-iodine (^{124}I) PET/MRI were included. The patient population consists of 13 female and 11 male patients (mean \pm standard deviation (SD) age 50.9 ± 17.4 years, mean body mass index (BMI) 25.8 ± 4.6 kg/m²). An average radiotracer dose of 235.4 ± 57.0 MBq for the ^{18}F -FDG examinations and 45.2 MBq for the ^{124}I examination were administered. All ^{18}F -FDG patients first underwent a clinically indicated PET/CT and subsequently an additional PET/MRI examination without further radiotracer injection. The PET/MRI measurements started 129 ± 40 minutes post injection for the ^{18}F -FDG patients and for the ^{124}I patient directly after injection. Patients were referred to whole-body PET/MRI because of staging/re-staging of malignant diseases (9 lymphoma, 5 gynaecological carcinoma, 5 bronchial carcinoma and 5 others). Arms were positioned along the body and PET data was acquired for 4 minutes. The whole-body PET/MRI was acquired in 4–5 bed stations. Detailed patient information is listed in Tab. 2.1.

# Patient	Sex	Age [years]	BMI [kg/m ²]	Tracer	Activity [MBq]	Minutes p.i.	Type of malignancy
1	M	54	22,4	¹⁸ F-FDG	339	140	bronchal carcinoma
2	F	63	19,5	¹⁸ F-FDG	275	169	bronchal carcinoma
3	F	26	20,1	¹⁸ F-FDG	138	122	Crohn's disease
4	F	52	23,8	¹⁸ F-FDG	268	135	bronchal carcinoma
5	F	69	29,4	¹⁸ F-FDG	138	53	uterus carcinoma
6	F	37	23,2	¹⁸ F-FDG	208	157	lymphoma
7	F	33	25,9	¹⁸ F-FDG	140	86	vulva carcinoma
8	F	77	22,2	¹⁸ F-FDG	187	119	lymphoma
9	M	59	22,2	¹⁸ F-FDG	268	146	lymphoma
10	M	22	21,6	¹⁸ F-FDG	148	60	bone cancer
11	M	77	26,5	¹⁸ F-FDG	251	122	Morbus Hodgkin
12	M	46	26,5	¹⁸ F-FDG	269	203	lymphoma
13	F	58	23,7	¹⁸ F-FDG	223	172	adenom carcinoma
14	M	64	33,1	¹⁸ F-FDG	278	98	lymphoma
15	F	50	37,2	¹⁸ F-FDG	212	41	uterus carcinoma
16	M	52	27,8	¹⁸ F-FDG	228	142	bronchal carcinoma
17	F	28	20,3	¹⁸ F-FDG	210	126	uterus carcinoma
18	F	74	32,1	¹⁸ F-FDG	245	148	mamma carcinoma
19	M	46	26,3	¹⁸ F-FDG	289	137	Non-Hodgin lymphoma
20	M	22	33,3	¹⁸ F-FDG	344	112	Morbus Hodgkin
21	M	71	23,0	¹⁸ F-FDG	262	139	Morbus Hodgkin
22	F	40	28,7	¹⁸ F-FDG	223	160	cancer of unknown primary
23	M	66	28,7	¹⁸ F-FDG	272	183	bronchal carcinoma
24	F	39	22,8	¹²⁴ I	45,2	0	ganglioneuroblastom
mean	13 F	51,9	25,8		235,4	129,1	
± SD	11 M	± 17,4	± 4,6		± 57,0	± 39,7	

Tab. 2.1: Statistically relevant data of the patient population including e.g., the body mass index (BMI). The start of measurement is given in minutes post injection (p.i.). Patients first underwent a clinically indicated PET/CT and subsequent a PET/MR. Patients # 5, # 7, # 10 and # 15 underwent a PET/MR only, thus, in those cases the post injection time is comparably short. Note that the mean \pm standard deviation (SD) for injected activity and minutes p.i. are for ¹⁸F-FDG patients only.

To validate the impact of truncation correction, all PET data was reconstructed three times with different AC-maps: 1. Dixon-VIBE only serving as a reference, 2. Dixon-VIBE with additional HUGE truncation correction and 3. Dixon-VIBE with additional MLAA truncation correction.

The truncation of body volume in the Dixon-VIBE AC-map was quantified to use this as a basis of assessment of performance of the truncation correction methods

HUGE and MLAA. Non-attenuation corrected (NAC) PET data was segmented to determine the true body volume of each patient. For quantitative evaluation standardized uptake values (SUVs), respectively the mean SUV_{mean} , the maximal SUV_{max} and the standard deviation SUV_{SD} , were measured in the primary lesion and in the myocardium (as a reference) in all reconstructed PET data for each patient. Additionally, SUVs in patients with visible radiotracer injection sites (located at patients' arm) were measured to further quantify the assessment of regions in the truncated areas. All volume-of-interests (VOIs) were copied in identical planes and position in each reconstructed dataset for each patient. Relative difference images between standard and improved SC were calculated using Matlab R2013b (MATrix LABoratory, Mathworks, Natick, MA, USA). Statistical significance and t -test were performed.

2.2 Improved AC including HUGE and bone model: Clinical application

2.2.1 Image acquisition and reconstruction

In this study, 32 patients with a cardiac ^{18}F -FDG PET/MRI were included. The patient population consists of 8 female and 24 male patients (mean \pm SD age 56.8 ± 13.7 years, mean BMI $26.9 \pm 4.6 \text{ kg/m}^2$). An average radiotracer dose of $184.7 \pm 63.4 \text{ MBq}$ was administrated and the PET/MRI started 72 ± 21 minutes post injection. Patients were referred to cardiac PET/MRI because of suspected cardiac sarcoidosis ($n = 11$), myocarditis ($n = 9$), endocarditis ($n = 6$), cardiac lesions ($n = 3$) and myocardial ischemia ($n = 3$). To suppress the cardiac glucose metabolism, thus to suppress ^{18}F -FDG enhancement in the normal myocardium, 29 patients fasted before PET/MRI (24 hours of low-carb diet and additional heparin administration). Three patients with suspected myocardial ischemia are studied with a viability protocol, hence they were administrated additional glucose to enhance the cardiac glucose metabolism, respectively to achieve myocardial ^{18}F -FDG enhancement (Fig. 2.3 F, I) [Lindemann et al., 2019b]. Arms were positioned along the body and PET data was acquired for 10 minutes in the thorax (single bed station).

Based on the implementation and validation of HUGE truncation correction combined with CTM in the previous section 3.1, HUGE now is available as commercial product for MR-based AC on the Biograph mMR (Siemens Healthcare GmbH, Erlangen, Germany) [Lindemann et al., 2017]. The HUGE AC-map is now automatically generated by the PET/MR system by fusing the Dixon-VIBE AC-map with HUGE data from extended FOV. In this section the clinical impact of improved AC with the

latest version of MR-based AC featuring HUGE truncation correction is tested in the thoracic region, where the impact of truncation correction is expected to be highest [Lindemann et al., 2019b]. Specific parameters of the HUGE MR sequence and the reconstruction of the MLAA AC-map are the same as mentioned earlier.

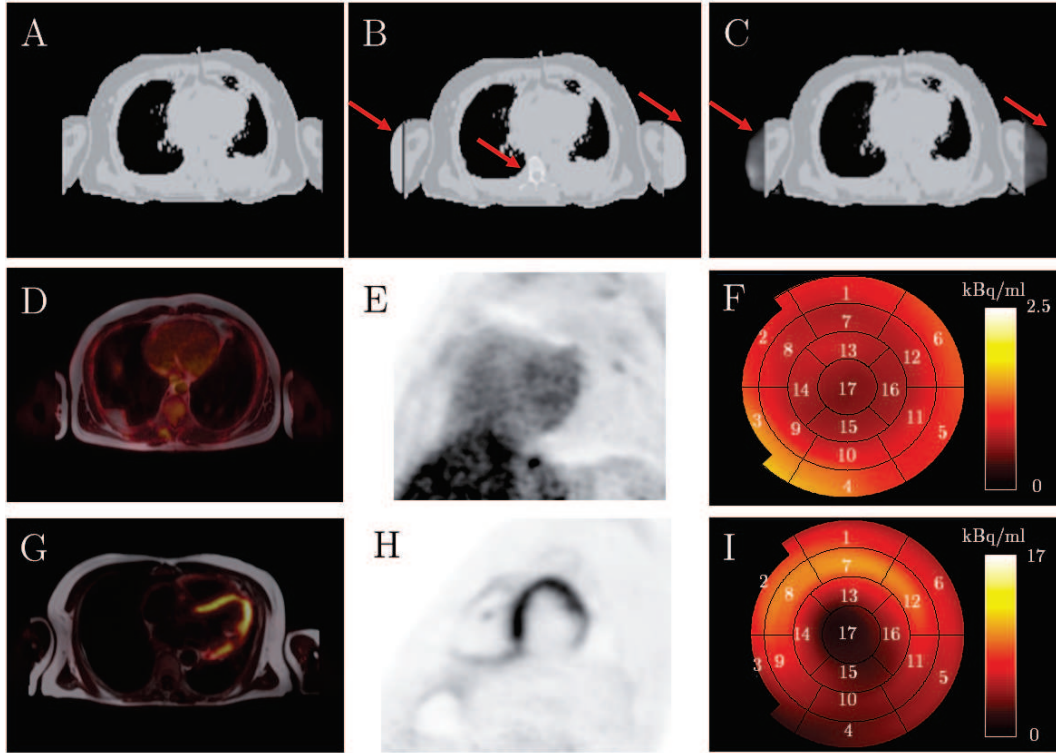


Fig. 2.3: Attenuation correction (AC) maps based on Dixon-VIBE sequence (A), the extended Dixon-VIBE sequence additionally using HUGE truncation correction and bone information (B), and the extended Dixon-VIBE sequence additionally using PET-based MLAA information (C). Red arrows depict differences between Dixon-VIBE only AC and improved AC-maps. Patient example studied in the fasted state (D-F) and patient example studied with a viability protocol (G-I) are shown. PET/MR fusion image (D, G) and PET short axis view (E, H) of the heart. A 17-segment polar plot (F, I) was generated for each patient and each PET data reconstruction to evaluate the quantitative effect of improved AC on cardiac PET imaging. Numbers 1–17 are assigned to cardiac segments according to the American Heart Association standard for cardiac polar plots [Lindemann et al., 2019b].

The latest version of MR-based AC also includes a bone model approach [Koesters et al., 2016; Paulus et al., 2015]. The bone model is generated from a set of pre-aligned MR images and bone mask pairs for six major bones from a database with more than 200 samples. The model includes the skull, the spine, the pelvis and the upper femur with continuous LACs from 0.1 cm^{-1} up to 0.2485 cm^{-1} . The bone model is

individually registered to the Dixon-VIBE MR images of each patient and the major bones are then added to the Dixon-VIBE AC-map.

To validate the impact of truncation correction and bone segmentation on cardiac PET/MRI, all PET data were reconstructed three times with different AC-maps: 1. Dixon-VIBE only, 2. Dixon-VIBE with additional HUGE truncation correction and bone segmentation and 3. Dixon-VIBE with additional MLAA truncation correction. The Dixon-VIBE AC-map served as a reference for all three comparisons of reconstructed PET data (Fig. 2.3 A-B) [Lindemann et al., 2019b].

2.2.2 Image analysis

All AC-maps were evaluated for artifacts. The truncation of body volume in the Dixon-VIBE AC-map was quantified to use this as a basis of assessment of performance of the truncation correction methods HUGE and MLAA. Non-attenuation corrected PET data was segmented to determine the true body volume of each patient.

According to the 17-segment model of the American Heart Association [Cerqueira et al., 2002] polar plots of the left ventricles in short-axis orientation were generated using Carimas v2.9 [Nesterov et al., 2009]. To ensure the uptake is always measured at identical location within the thickness of the end-systolic myocardium for all reconstructions, the left ventricle myocardium was segmented from generated short-axis MR images. To compare polar plots from different reconstructions using different AC-maps, it was refrained from normalizing the polar plots. This is motivated by the fact that regional uptake from a specific location defined as a reference for normalization might change for different reconstructions and distorts the results [Lindemann et al., 2019b].

Segment-wise, relative differences between standard Dixon-VIBE AC and improved AC was calculated to evaluate the quantitative impact of truncation correction and bone segmentation on cardiac PET/MRI. For statistical analysis of added body volume in the AC-map and PET signal per cardiac segment in the polar plots Bland-Altman plots were generated and statistical significance and *t*-test were performed.

2.3 Improved SC using un-renormalized absolute scaling on ^{68}Ga -PSMA PET/MRI

2.3.1 Image acquisition and reconstruction

In this study, 100 male patients with a pelvic ^{68}Ga -PSMA PET/MRI were included. The patient population (mean \pm SD age 69.3 ± 7.8 years, mean BMI 27.1 ± 3.5 kg/m²) was administrated an average radiotracer dose of 117.2 ± 29.7 MBq and the PET/MRI measurement started 138 ± 69 minutes post injection. Patients also received 20 mg of furosemide 15 minutes after injection and were referred to pelvic ^{68}Ga -PSMA PET/MRI because of either suspected primary prostate carcinoma or biochemical recurrence.

All patients were asked to empty their bladder directly before the PET/MRI examination. Arms were positioned along the body and PET data was acquired for 10 to 40 minutes in the pelvis (single bed station). For AC the latest MR-based methods including HUGE truncation correction and bone segmentation were used [Lindemann et al., 2017; Paulus et al., 2015; Oehmigen et al., 2017]. To compare PET data from all patients, a 10 minute time interval from the start of the PET examination was obtained from the list-mode PET data for each patient. To validate the impact of improved SC on pelvic ^{68}Ga -PSMA PET/MRI, all PET data were reconstructed twice with different SC: 1. standard SC serving as a reference and 2. un-renormalized SC serving as an improved version of SC. Both SC methods are implemented as SSS with an absolute scaling of estimated scatter. The difference between both SC methods is that improved SC (un-renormalized SC) excludes the last scaling (renormalizing) step of the PET emission image during the SC calculation. Default parameters for both SC methods are: number of iterations 2, maximum scatter fraction 75 %, scale factor 1.0. These parameters were kept constant for all reconstructions [Lindemann et al., 2019a].

To validate the impact of shorter PET acquisition time on PET image quality and lesion detectability, PET data of two patients with lesions inside the halo margin were additionally reconstructed with a 4 minute time interval (with standard and improved SC) and compared to the standard 10 minute time interval.

2.3.2 Image analysis

In most cases the margin of the halo artifact is inhomogeneous, and thus an accurate measurement of the halo volume is not feasible [Afshar-Oromieh et al., 2014]. Therefore, the halo presence and visibility were rated in five grades: 0 = no halo artifact, 1 = slight halo artifact, 2 = moderate halo artifact, 3 = strong halo artifact, 4 = severe

halo artifact (Fig. 2.4) [Lindemann et al., 2019a]. All PET images were analysed for lesion detectability. Therefore, a 4-point detectability score was defined [Noto et al., 2017] 0 = not detectable, 1 = equivocal, 2 = discernible, 3 = clearly visible. For quantitative evaluation SUV_{mean} , SUV_{max} and SUV_{SD} were measured in the halo margin, the bladder, the gluteus maximus and all detected lesions in all reconstructed PET data for each patient. All ROIs and VOIs were copied into identical planes and positions in each reconstructed dataset for each patient. Relative difference images between standard and improved SC were calculated using Matlab R2013b (MATrix LABoratory, Mathworks, Natick, MA, USA). Image quality parameters (SNR, image noise, organ-to-background-ratio (OBR)) were calculated and statistical significance and t -test were performed.

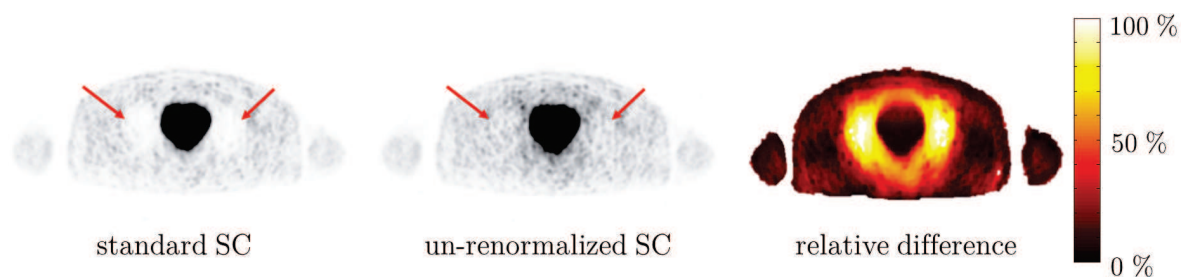


Fig. 2.4: PET images reconstructed using standard and un-renormalized scatter correction (SC) and relative difference image between both SC methods. In standard corrected PET image a severe halo artifact is observable (grade 4, red arrows), whereas the un-renormalized corrected image shows no halo artifact (grade 0, red arrows). Relative differences in PET activity up to 100% in this example are maximal in the halo margin; the differences between standard and un-renormalized SC in bladder and surrounding tissue are below 5% [Lindemann et al., 2019a].

2.4 Fast PET/MRI: PET image quality vs. PET acquisition time

2.4.1 Image acquisition and reconstruction

In this study, 51 patients with a whole-body ^{18}F -FDG PET/MRI were included. The patient population consists of 27 female and 24 male patients (mean \pm SD age 45.5 ± 20.3 years, mean \pm SD BMI 25.5 ± 5.6 kg/m²). An average radiotracer dose of 218.8 ± 59.1 MBq was administered. 22 patients were referred to PET/MRI examination only and the measurement started 65 ± 14 minutes post injection. 29 patients first underwent a clinically indicated PET/CT and subsequently an additional PET/MRI

examination without further radiotracer injection. The PET/MRI measurements subsequently to the PET/CT started 144 ± 36 minutes post injection. Patients were referred to whole-body PET/MRI because of staging/re-staging of malignant diseases (17 lymphoma, 10 gynecological carcinoma, 7 cancer of unknown primary, 6 breast cancer, 5 rectal carcinoma and 8 others).

On average 4-5 bed positions per patient were acquired to cover the whole body. PET and MR data were acquired simultaneously for 4 minutes per bed position. For AC the latest MR-based methods including HUGE truncation correction and bone segmentation were used [Lindemann et al., 2017; Paulus et al., 2015; Oehmigen et al., 2017]. To validate the impact of shorter PET acquisition time on PET image quality, PET list-mode data was reconstructed with a 4, 3, 2 and 1 minute time interval from the start of the measurement for each patient. The 4 minute time interval served as a reference standard.

2.4.2 Image analysis

All PET datasets for each patient were analysed with regard to image quality and lesion detection. Therefore, a 4-point image quality score (IQS) was defined: 0 = non-diagnostic, 1 = poor, 2 = moderate, 3 = good [Lindemann et al., 2018]. For quantitative evaluation SUV_{mean} , SUV_{max} and SUV_{SD} were measured in the liver, the spleen, the gluteus maximus, the blood pool and in all detected lesions in all reconstructed PET data for each patient. All ROIs and VOIs were copied in identical planes and position in each reconstructed dataset for each patient. Image quality parameters (SNR, contrast-to-noise-ratio (CNR), image noise) were calculated and statistical significance, *t*-test and correlation were performed.

3 Results

3.1 Improved AC: Implementation of HUGE truncation correction

3.1.1 Phantom measurements

The Dixon-VIBE AC-map shows truncations along the arm phantoms at the edges of the MR FOV (Fig. 3.1 A), whereas CT-based AC-map serving as a reference covers the entire phantom setup (Fig. 3.1 B). Here, no distortions at the extended FOV are visible. HUGE AC-map significantly reduces the truncations along the arm phantom (Fig. 3.1 C). The arm phantom volume of the HUGE AC-map is qualitatively comparable with the CT-based AC-map. The MLAA AC-map also reduces the truncations at the edges of the MR FOV, but the arm phantom volume is slightly overestimated (Fig. 3.1 D).

Fig. 3.1 E shows the relative difference in activity concentration in the hot spheres in the NEMA IQ phantom for Dixon-VIBE, HUGE and MLAA AC compared to the CT AC reference standard. The deviation in activity concentration compared to CT AC is, as expected, highest in Dixon-VIBE corrected PET data with mean \pm SD $-6.5 \pm 1.1\%$ (range -8.3% to -5.5%). The percentage deviation in activity concentration could be reduced to $-3.0 \pm 1.4\%$ (range -4.7% to -0.8%) using HUGE information and $-4.9 \pm 1.8\%$ (range -8.0% to -2.9%) using MLAA information from extended FOV. The results with HUGE are closest to the reference CT AC, while the MLAA corrected PET data show comparably higher deviations in activity concentration compared to CT reference. The 17mm sphere, which is closest to the arm phantoms and therefore affected most by attenuation, benefits the most from truncation correction. Here, barely any difference (-0.8%) between HUGE and CT AC is measurable [Lindemann et al., 2017].

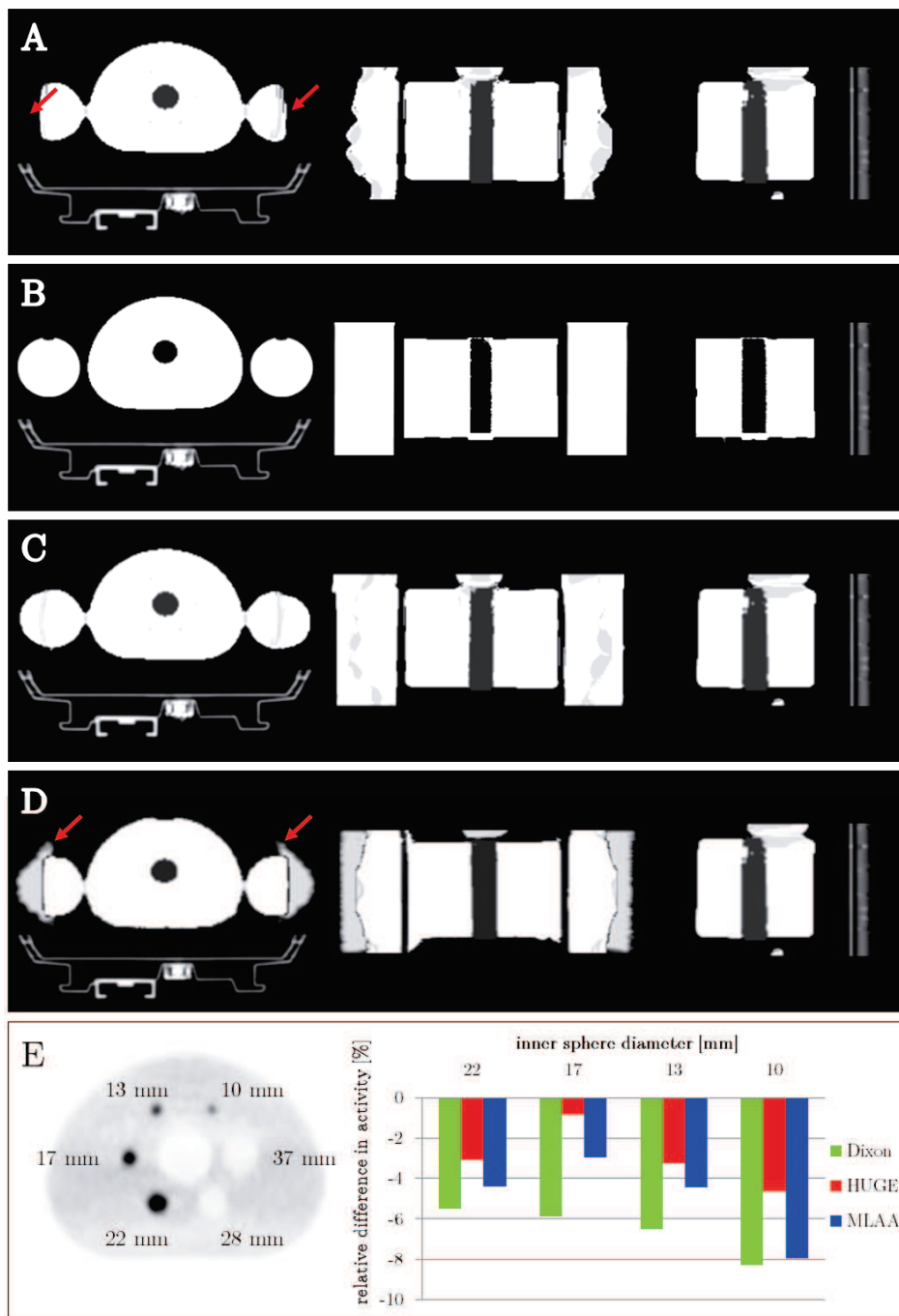


Fig. 3.1: Combined attenuation correction maps (AC-maps) consisting of the CT-based hardware AC-map of the patient table and the phantom AC-map in axial (left), coronal (middle) and sagittal (right) orientations. The phantom AC-map is based on the Dixon-VIBE sequence (A), CT-based without phantom housing (B), the extended Dixon-VIBE sequence additionally using MR-based HUGE information (C) and the extended Dixon-VIBE sequence additionally using PET-based MLAA information (D). PET image of the NEMA phantom with 6 spheres aligned radially around the lung insert, 4 spheres are injected with activity (hot, dark) and 2 are filled with water (cold, bright) (E, left). Calculated relative difference in activity in hot spheres for Dixon- (green), HUGE- (red) and MLAA-based (blue) AC in comparison to the CT reference. Note the truncations along the arm phantoms in the Dixon-VIBE AC-map (arrows). The MLAA AC-map shows regional volume overestimation (arrows) [Lindemann et al., 2017].

3.1.2 Patient measurements

Fig. 3.2 shows Dixon-VIBE, HUGE and MLAA AC-maps of three patients with a different BMI (lowest, medium and highest BMI included in the patient cohort). The Dixon-VIBE AC-map shows truncations along the arms in each patient, even in the patient with the lowest BMI (Fig. 3.2). HUGE and MLAA truncation correction significantly reduce the amount of truncation in the Dixon-VIBE AC-map in each patient regardless of the BMI. HUGE qualitatively provides accurate and robust contour detection. No signal drop-outs, artifacts or overestimations could be observed in the HUGE AC-maps. MLAA applies reduced LAC to the truncated areas in the AC-map and shows regional overestimation around the arms due to improper body contour detection [Lindemann et al., 2017].

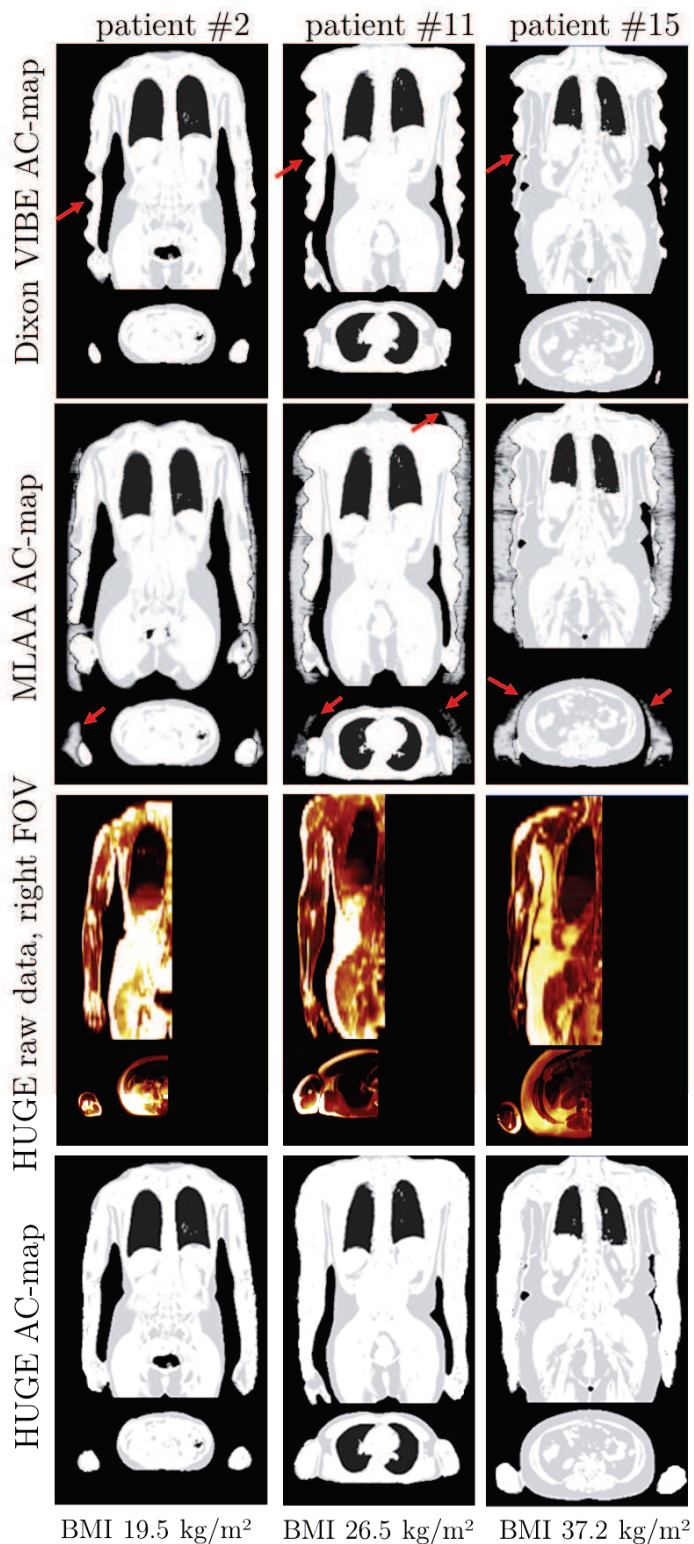


Fig. 3.2: Different attenuation correction maps (AC-maps) of three selected patients that provide a range of different body mass indices (BMIs). Dixon-VIBE AC-maps showing truncations along the arms (arrows). MLAA AC-maps show added volume along the arms, arrows mark the overestimated arm volume and artifacts from inaccurate contour detection with PET-based MLAA. HUGE raw data from the patient's right field-of-view (FOV, for demonstration purposes) and the resulting MR-based HUGE AC-map show the added body volume along the arms [Lindemann et al., 2017].

Fig. 3.3 shows the percentage volume deviations of the patients' arms in the Dixon-VIBE, HUGE and MLAA AC-maps compared to the patients' arms segmented in the NAC PET data. Patients in Fig. 3.3 are sorted by increased BMI. Using the Dixon-VIBE AC-map, body volume truncations of mean \pm SD $-11.5 \pm 8.0\%$ (range -40.1% to -3.1%) were observed. Using the HUGE AC-map, body volume truncations of $-1.0 \pm 3.2\%$ (-5.7% to 6.6%) were observed. Using the MLAA AC-map, body volume truncations of $8.9 \pm 7.7\%$ (-1.5% to 26.1%) were observed. All patients showed truncations in the Dixon-VIBE AC-map, whereas the truncated volume tends to be higher in patients with a high BMI. The truncations could be significantly reduced using HUGE, independent of patients' BMI. The volume of HUGE AC-maps and segmented NAC PET data is quantitatively comparable. In patients with a lower BMI, MLAA could reduce truncations in the AC-map. Whereas in patients with higher BMI, MLAA tends to overestimate the body contour compared to segmented NAC PET data.

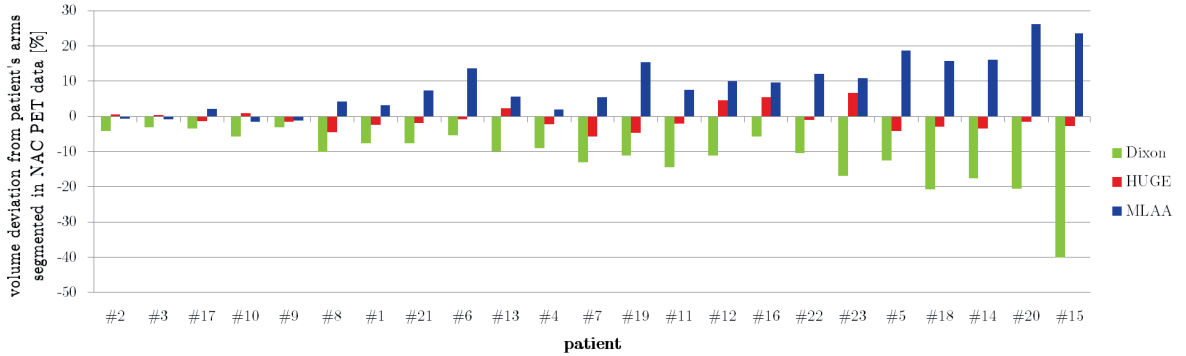


Fig. 3.3: Percentage volume deviations of the patients' arms in the Dixon-VIBE (green), HUGE (red) and MLAA (blue) attenuation correction maps (AC-maps) compared to the patient's arms segmented in the non-AC PET data. All 23 ^{18}F -FDG patients are sorted by increasing body mass index (BMI) from left to right. Note the tendency of increased body volume truncation percentage in the Dixon-VIBE AC-maps for patients with higher BMI.

Fig. 3.4 shows the relative deviation in AC-map volume and SUV_{mean} in patients' primary lesion and myocardium with HUGE (red), respectively MLAA (blue), truncation correction compared to standard Dixon-VIBE AC for 23 ^{18}F -FDG patients. The increase in AC-map volume due to HUGE is mean \pm SD $5.8 \pm 3.4\%$ (range 1.5% to 14.1%) and for MLAA $9.7 \pm 4.0\%$ (4.9% to 20.2%). The increase in SUV_{mean} in patients' primary lesion due to HUGE is mean \pm SD $4.2 \pm 2.9\%$ (range 0.4% to 9.1%) and for MLAA $4.6 \pm 3.3\%$ (0.5% to 11.9%). The increase in SUV_{mean} in patients' myocardium due to HUGE is mean \pm SD $3.6 \pm 2.9\%$ (range 0.3% to 12.4%) and for MLAA $3.9 \pm 3.1\%$ (0.5% to 14.3%). Each patient benefits from truncation correction, either HUGE or MLAA. Maximal relative differences occur in lesions close

to truncations (e.g. Fig. 3.4 B patient # 10 bone cancer in left femur, patient # 12 lymphoma in left shoulder) or patients with a high BMI (e.g. Fig. 3.4 B patient # 15 BMI 37.2 kg/m², patient # 20 BMI 33.3 kg/m²). A high BMI is often associated with overall large body dimensions exceeding the constraints of the conventional MR FOV [Lindemann et al., 2017].

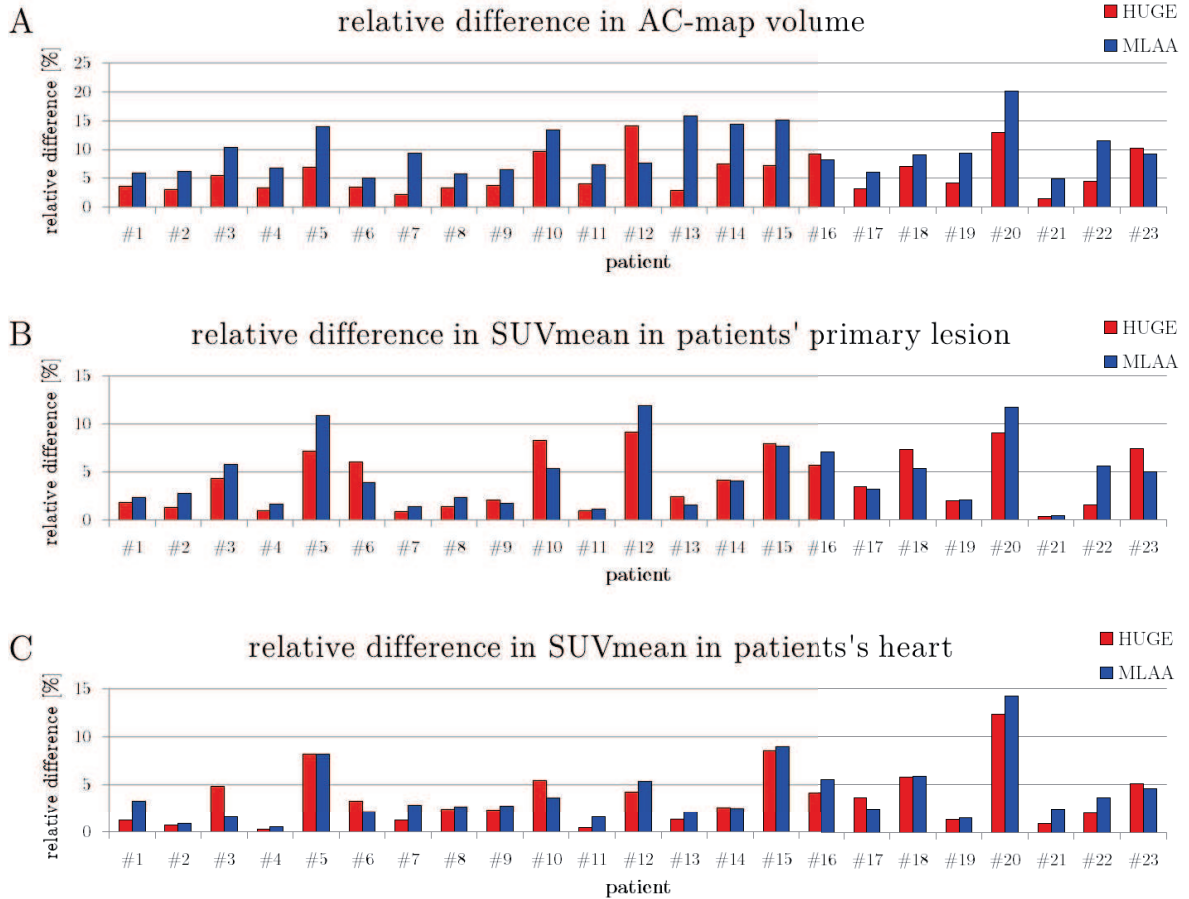


Fig. 3.4: Quantitative impact of applying truncation correction with the HUGE and the MLAA method. The relative difference in attenuation correction map (AC-map) volume (A), SUV_{mean} of the primary lesion (B) and SUV_{mean} of myocardium (C) of each ¹⁸F-FDG patient is compared for HUGE-based (red) and MLAA-based (blue) AC in comparison to standard Dixon-VIBE AC [Lindemann et al., 2017].

Bland-Altman plots in Fig. 3.5 show the comparison between HUGE and MLAA truncation correction in AC-map volume and SUV_{mean} in patients' primary lesion compared to Dixon-VIBE AC. Nearly all patients gain more AC-map volume with MLAA than with HUGE truncation correction. Whereas, corresponding SUV_{mean} results depict that the impact of both truncation correction methods are qualitatively and quantitatively comparable, thus nearly equal.

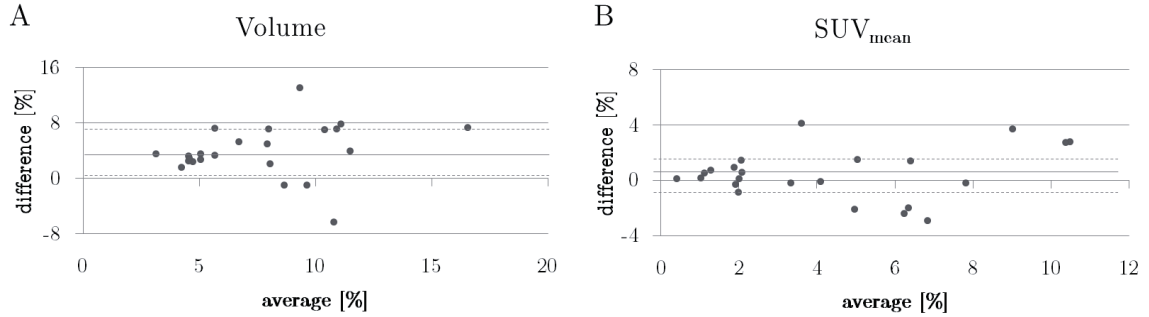


Fig. 3.5: Bland-Altman plots depict the comparison between HUGE and MLAA attenuation correction (AC) on AC-map volume (A) and SUV_{mean} in patients' lesions (B) in contrast to standard Dixon-VIBE AC serving as reference. Nearly all patients gain more AC-map volume with MLAA than with HUGE. Whereas, corresponding SUV_{mean} results in the lesions show a nearly equal impact of both truncation correction methods.

Fig. 3.6 shows AC-maps, relative difference images and PET/MR fusion images with marked primary lesion of two ^{18}F -FDG patient examples. In both examples, the Dixon-VIBE AC-map shows truncation along the arms (red arrow). HUGE and MLAA AC-maps both qualitatively improve AC by correcting the distortions at the edges of the MR FOV. While HUGE results in plausible body contouring, MLAA tends to overestimate the arm volume in both examples (red arrow). The relative difference images of both patient examples show that the impact of truncation correction, either with HUGE or MLAA, is highest in the arms, where body volume was added. Also in the pelvis and thoracic region a gain in PET signal due to improved AC is observable. The increase in AC-map volume due to HUGE is 9.6% for patient # 10 and 9.2% for patient # 16. The gain in PET signal in the primary lesion due to HUGE is 8.3% for patient # 10 and 5.7% for patient # 16 [Lindemann et al., 2017]. While both patients have comparable gain in AC-map volume, patient # 10 benefits more from improved AC. The lesion is closer relative to truncations, thus the quantitative impact of truncation correction is higher.

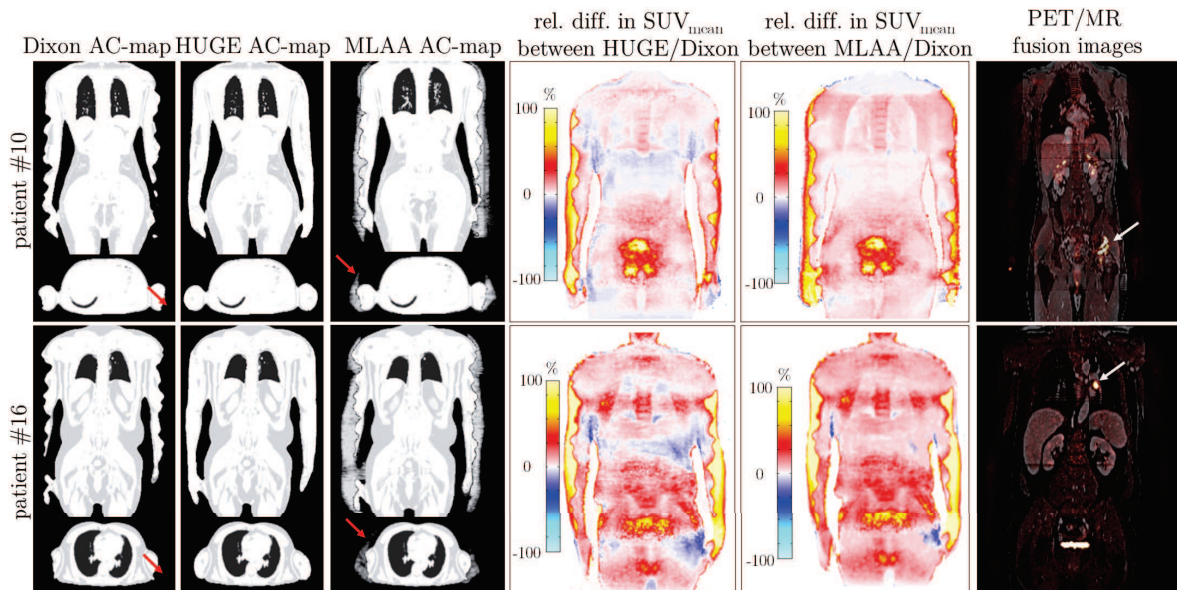


Fig. 3.6: Dixon-VIBE-, HUGE- and MLAA-based attenuation correction maps (AC-maps) of two ^{18}F -FDG patients are shown. Relative difference (rel. diff.) PET images between HUGE, respectively MLAA, and standard Dixon-VIBE AC were calculated. In PET/MR fusion images the primary lesion is marked. Discrete stripe artifacts in MR images result from coronal reformats at the positions where the transaxially acquired slice stack of two neighboured bed positions are merged. Maximal relative differences in activity are observable along the arms of both patients [Lindemann et al., 2017].

Tab. 3.1 depicts the relative differences between HUGE, respectively MLAA, compared to Dixon-VIBE AC in the SUV_{mean} in the heart and at radiotracer injection sites of eight patient examples with visible radiotracer injection sites. The mean \pm SD increase in SUV_{mean} in the heart is $3.5 \pm 2.7\%$ for HUGE and $3.9 \pm 2.7\%$ for MLAA compared to standard Dixon-VIBE AC. The average increase in SUV_{mean} in the injection site is $13.3 \pm 10.5\%$ for HUGE and $14.6 \pm 12.6\%$ for MLAA compared to standard Dixon-VIBE AC. Maximal relative differences of more than 40% due to truncation correction could be measured in patient example # 15. The quantitative impact of truncation correction is much higher in the injection sites, which are located in or near by truncation artifacts, as in the heart, which is located in the middle of the body.

rel. difference [%] in SUV_{mean} compared to Dixon				
Patient	Heart		Injection site	
	HUGE	MLAA	HUGE	MLAA
# 2	0.74	0.86	7.98	8.20
# 4	0.25	0.50	8.11	8.31
# 10	5.46	3.63	9.95	7.87
# 12	4.27	5.36	10.87	12.99
# 13	1.27	2.06	7.63	6.97
# 15	8.53	9.01	40.01	46.81
# 18	5.76	5.89	15.82	17.04
# 22	2.05	3.67	6.09	8.66

Tab. 3.1: Comparison of the relative quantitative impact of HUGE and MLAA truncation correction compared to standard Dixon attenuation correction on mean standardized uptake value (SUV_{mean}) in eight patients with visible radiotracer injection sites. The table provides the percentage relative difference of the SUV_{mean} in the heart (located in the mid-thorax) and at the tracer injection site in the arms (located off-centre in truncated regions) [Lindemann et al., 2017].

Fig. 3.7 shows AC-maps, relative difference image and PET/MR fusion image with five marked lesions of a non-FDG patient example. The patient was injected with radiotracer iodine ^{124}I . PET-based contour detection with MLAA failed in this example, while HUGE truncation correction works robust and independent of the choice of radiotracer. HUGE adds 5.7% body volume to the Dixon-VIBE AC-map in this non-FDG patient. The corresponding gains in SUVs due to truncation correction for the five marked lesions are listed in Tab. 3.2. In lesion 1 the relative difference in SUV is

minimal. In this region hardly any volume was added to the AC-map due to truncation correction. In lesion 4, which is very close to truncations, the quantitative impact of truncation correction is maximal [Lindemann et al., 2017].

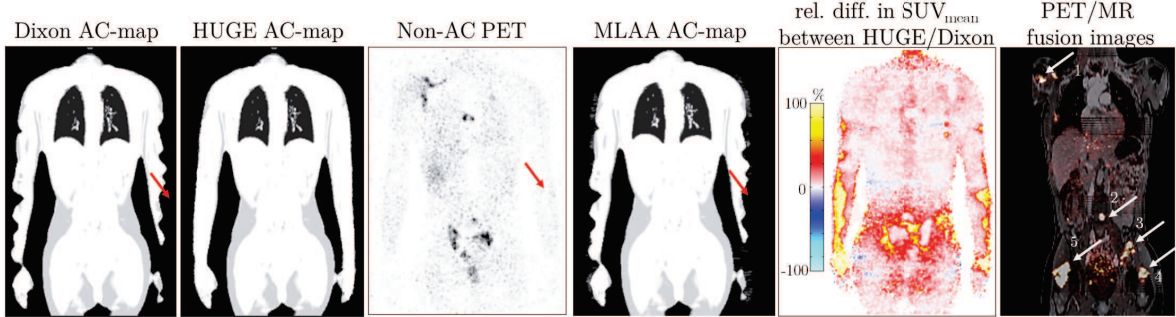


Fig. 3.7: Dixon- and HUGE-based attenuation correction maps (AC-maps), non-AC PET image and MLAA-based AC-map of the ^{124}I patient are shown. In this non-FDG example PET contour detection of the patient’s body is not possible, accordingly, the application of PET contour detection methods using MLAA failed in this example. Consequently, no truncated volume was added to the Dixon AC-map. Relative difference (rel.diff.) PET images between HUGE and standard Dixon-VIBE AC were calculated. In PET/MR fusion images five lesions are marked. Discrete stripe artifacts in MR images result from coronal reformats at the positions where the transaxially acquired slice stack of two neighboured bed positions are merged. Maximal relative differences in activity are observable along the arms.

Lesion	SUV_{mean}			SUV_{max}		
	Dixon	HUGE	rel. difference [%]	Dixon	HUGE	rel. difference [%]
1	5.9	5.9	0.9	9.9	9.9	0.2
2	6.2	6.4	3.4	10.3	10.5	2.2
3	6.6	7.0	6.5	11.9	12.7	6.4
4	4.6	5.3	14.0	8.2	9.2	13.2
5	7.6	8.1	7.8	14.5	15.3	5.5

Tab. 3.2: Standard uptake values (SUV_{mean} and SUV_{max}) measured in Dixon-VIBE and HUGE attenuation corrected PET data of five active lesions (Fig. 3.7) in a non-FDG patient example (^{124}I) [Lindemann et al., 2017].

3.2 Improved AC including HUGE and bone model: Clinical application

3.2.1 Quantitative cardiac PET/MRI

The percentage volume deviations of patients' arms in the Dixon-VIBE, HUGE and MLAA AC-maps compared to the patients' arms segmented NAC PET data was calculated. The Dixon-VIBE AC-map shows truncations along the arms in each patient ($-12.7 \pm 7.1\%$). MLAA tends to overestimate the arm volume ($7.8 \pm 8.3\%$), while HUGE truncation correction works robust and results in reliable body contouring ($-1.9 \pm 3.9\%$) [Lindemann et al., 2019b].

Fig. 3.8 shows the statistical analysis over all patient data sets of the impact of improved AC, respectively HUGE truncation correction and bone segmentation or MLAA truncation correction, compared to standard Dixon-VIBE AC for added AC-map volume and global activity in the entire myocardium. Considering all 32 patients, the average increase in AC-map volume due to HUGE is mean \pm SD $5.4 \pm 2.0\%$ (range 1.4% to 9.2%) and $8.5 \pm 3.4\%$ (3.0% to 16.2%) due to MLAA truncation correction. Relative differences in AC-map volume are statistically significant for both truncation correction methods. The average increase over all patients and segments in PET activity in the left ventricle myocardium using HUGE + bone AC is mean \pm SD $6.1 \pm 3.0\%$ (range 0.4% to 18.8%) and $8.3 \pm 4.3\%$ (0.9% to 19.8%) using MLAA AC. Relative differences in global PET activity are statistically significant for both AC methods. Nearly all patients gain more AC-map volume due to MLAA truncation correction. However, the relative gains in global PET activity for both improved AC methods are quantitatively comparable. MLAA AC leads to a systematically higher count statistic due to the overestimation of body contour [Lindemann et al., 2019b].

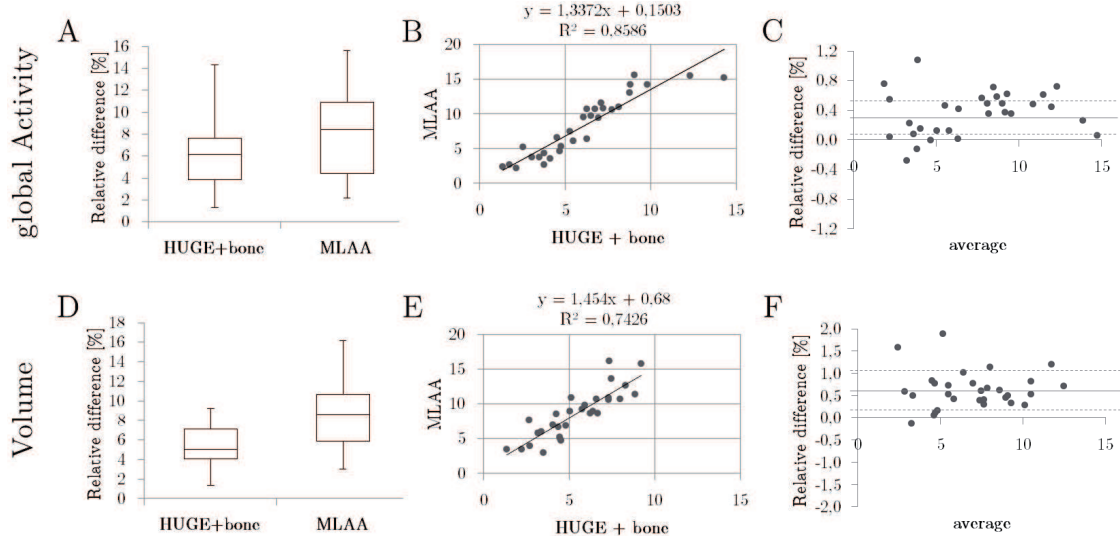


Fig. 3.8: Statistical analysis of quantitative impact of HUGE field-of-view extension, bone segmentation and MLAA field-of-view extension on global PET signal over all segments of the left ventricle (A-C). The increase of attenuation correction (AC) map volume (D-F) relative to AC-map volume as provided by standard Dixon-VIBE imaging is given. Boxplots (A, D) show the statistical distribution in relative gain of activity and volume from applying improved AC. Correlation graphs (B, E) and Bland-Altman plots (C, F) depict the comparison between HUGE + bone and MLAA in contrast to standard Dixon-VIBE AC serving as reference. In the correlation graphs (B, E) the linear equation with the coefficient of determination (R^2) is given [Lindemann et al., 2019b].

In Fig. 3.9 relative difference polar plots are shown depicting the quantitative impact per cardiac segment of improved AC compared to standard Dixon-VIBE AC in all 32 PET data sets. In all difference polar plots a slight increase in PET signal from base to apex is noticeable, thus maximal relative differences between standard and improved AC occur in segment 17 (apex). Fig. 3.9 A shows the impact of truncation correction on cardiac PET/MRI. Both difference polar plots exhibit a slight decrease in relative difference of PET signal compared to Dixon-VIBE AC inferior-medial (segments 3, 4 and 9, 10) due to missing bone information. The relative difference over all segments and patients for HUGE corrected data is 6% and 8% for MLAA corrected data. Fig. 3.9 B shows the impact of additional bone segmentation in AC. In 7 patients the bone segmentation failed and were not included in the analysis. Incorporating the bone model approach of the 25 patients with proper bone correction in the AC results in a homogeneous increase in relative difference across all cardiac segments. Comparing the distribution of gains in relative differences in Fig. 3.9 A and C, the relative difference polar plots are qualitatively comparable. Thus, the patient preparation seems to have no impact on signal distribution in the left ventricle [Lindemann et al., 2019b].

Maximal relative differences between improved AC and standard Dixon-VIBE AC could be measured in a patient with a BMI of 36.7 kg/m^2 . The increase in AC-map volume was 9.2 % for HUGE and 15.7 % for MLAA truncation correction, the maximal values in this patient cohort. The global increase in relative difference in PET signal over all segments was 14.3 % for HUGE + bone and 15.2 % for MLAA. The maximal relative differences occurred in the apex with 18.8 % for HUGE + bone and 19.8 % for MLAA [Lindemann et al., 2019b].

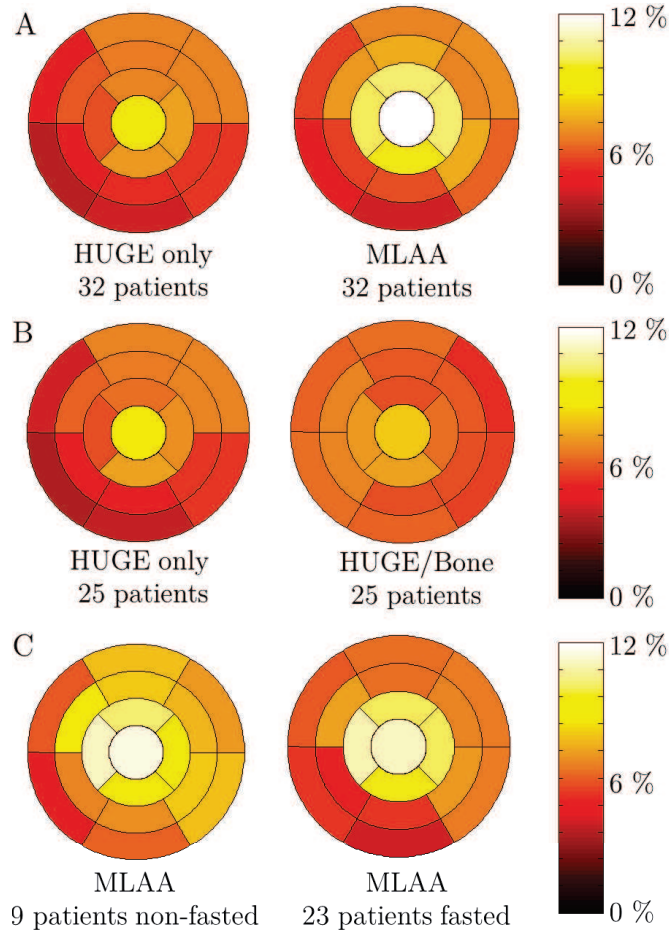


Fig. 3.9: Relative difference polar plots between improved and standard Dixon-VIBE attenuation correction (AC) serving as the reference standard show the impact of truncation correction (A) and bone AC (B) on cardiac PET/MRI. Average relative difference per segment in MLAA corrected data in patients with fasted preparation and non-fasted preparation are shown (C). Note the homogeneous gain in relative difference due to HUGE and bone AC of 6 % across all cardiac segments (B), whereas in MLAA and HUGE-only corrected data a slight decrease in relative difference inferior-medial is noticeable due to missing bone information (A). The relative difference over all segments and patients for MLAA is 8 %. The patient preparation seems to have rather low impact on overall signal distribution in the left ventricle (C) [Lindemann et al., 2019b].

3.2.2 AC-map artifacts

In Tab. 3.3 five categories of AC-map artifacts and their origin as well as their frequency of appearance are listed. Fig. 3.3 shows examples of these five AC-map artifacts. In three patients metal wire cerclage leads to misclassification of surrounding tissue as background air in the Dixon-VIBE AC-map. In seven patients the bone model approach failed. Only one single arm in one patient could not be segmented due to insufficient MR signal in the HUGE raw data. In every patient the MLAA approach overestimates the arm volume [Lindemann et al., 2019b].

AC method	Type of artefact	Origin	Frequency
Dixon-VIBE	tissue misclassification	metal artifact due to metallic implants, metallic clips or wire cerclages	3/32
Bone	missing bone segmentation	no reference for registration of bone model	3/32
Bone	mismatched bone segmentation	wrong reference for registration of bone model	4/32
HUGE	missing HUGE information	no segmentation of arms due to insufficient signal in MR sequence	1/32
MLAA	volume overestimation	insufficient estimation of PET contour detection	32/32

Tab. 3.3: Classification of five different attenuation correction (AC) map artifacts in 32 patients [Lindemann et al., 2019b].

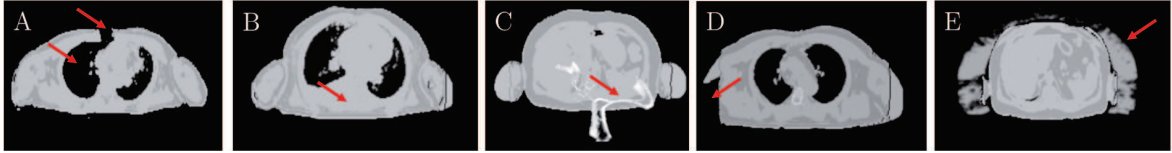


Fig. 3.10: Red arrows show attenuation correction (AC) map artifacts. In 3/32 patients metal artifacts in Dixon-VIBE AC-map leads to misclassification of surrounding tissue as “air” (A). Note that in this example the thorax is virtually opened due to the metal artifact. In 3/32 AC-maps no bone was segmented (B). In 4/32 patients the bone segmentation mismatches the anatomy (C). In 1/32 patient missing arm segmentation in HUGE imaging occurred (D), and in all 32/32 patients overestimation of AC-map volume in MLAA AC-maps was observed (E) [Lindemann et al., 2019b].

In Fig. 3.11 a patient example with failed bone segmentation in the AC-map is shown. Corresponding relative difference polar plots between improved and standard Dixon-VIBE AC are given. The HUGE + bone corrected data shows a global increase in PET signal of 5.5% across the entire left ventricle myocardium. In segments 2, 3 and 9, 10 an increased relative difference is noticeable due to wrong bone segmentation. Maximal relative differences comparing bone (HUGE + bone) and non-bone (HUGE only) AC was measured with 6% in segment 9 [Lindemann et al., 2019b].

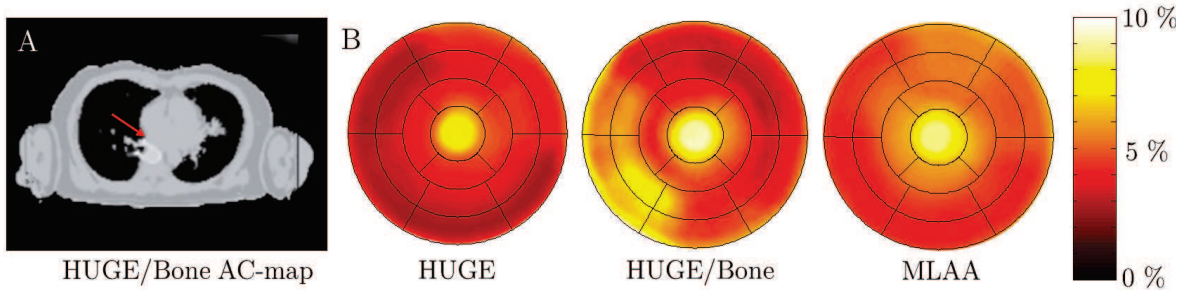


Fig. 3.11: Patient example with a bone artifact (red arrow) in the HUGE + bone AC-map (A). Corresponding difference polar plots of HUGE only, HUGE + bone and MLAA corrected PET data in comparison to standard Dixon-VIBE attenuation correction (AC) (B). Note that HUGE only and MLAA corrected PET data show a slight decrease in relative difference inferior-medial, whereas, in HUGE and bone corrected data (middle polar plot) an increase in relative difference in segments 2–3 and 8–9 is observable due to the bone artifact [Lindemann et al., 2019b].

3.3 Improved SC using un-renormalized absolute scaling on ^{68}Ga -PSMA PET/MRI

3.3.1 Image quality and quantification

The presence of halo artifacts was rated in five grades (0-4) in all 100 PET data sets (Tab. 3.4). The average grade in standard SC images was 2 (moderate halo presence), while halo grade in PET data corrected with improved SC was rated in average as 0.9 (slight halo presence). The presence of halo artifact could inherently be reduced using un-renormalized SC, no severe halo (grade 4) could be observed any more and 23 data sets had no halo artifact (grade 0) at all. While in standard scatter corrected PET data 3 patients had a severe halo artifact (grade 4) and only one patient had no halo artifact (grade 0) [Lindemann et al., 2019a].

Halo grade	standard SC	un-renormalized SC
0	1	23
1	31	66
2	39	10
3	26	1
4	3	0
mean \pm SD	2.0 \pm 0.9	0.9 \pm 0.6

Tab. 3.4: The presence of halo artifacts was rated in 5 grades as follows: 0 = no halo artifact, 1 = slight halo presence, 2 = moderate halo presence, 3 = strong halo presence, and 4 = severe halo. Data are the number of patients with respective grades. The halo intensity can be reduced by using un-renormalized scatter correction (SC) over standard SC [Lindemann et al., 2019a].

Fig. 3.12 shows Bland-Altman plots of relative differences in SUV_{mean} and SUV_{max} in the gluteus maximus, the bladder, the halo margin and all detected lesions using standard or improved SC. In each region, SUVs increase using improved SC. Especially in the halo margin, a remarkable gain in SUVs was measured. Considering all 100 PET data sets, the SUV_{mean} in the gluteus maximus increased by mean \pm SD 23.0 \pm 9.2 % (range 9.9 % to 75.7 %) and the SUV_{max} increased by 15.8 \pm 7.9 % (0.2 % to 50.9 %) using un-renormalized SC compared to standard SC. The increase in SUV_{mean} in the bladder was mean \pm SD 7.1 \pm 4.5 % (range 0 % to 16.7 %) and in SUV_{max} 5.9 \pm 3.8 % (0.1 % to 14.7 %) with improved SC. The increase in SUV_{mean} in the halo margin was mean \pm SD 325.4 \pm 748.5 % with a median of

127.3% (range 35.5% to 5463.4%) and in SUV_{\max} $163.0 \pm 250.5\%$ with a median of 77.3% (12.6% to 1327.4%) with improved SC. The increase in SUV_{mean} in all 74 detected lesions was $\text{mean} \pm \text{SD}$ $12.4 \pm 16.8\%$ with a median of 7.4% (range -6.3% to 105.6%) and in SUV_{\max} $5.5 \pm 6.1\%$ (-1.7% to 33.8%) with improved SC. Relative differences in SUVs in the gluteus maximus, the bladder and the lesions were statistically significant and relative differences in SUVs for the halo margin were statistically highly significant ($p < 0.01$) [Lindemann et al., 2019a].

To evaluate the impact of improved SC on PET image quality, OBR, image noise and SNR in the gluteus maximus, the bladder, the halo margin and all detected lesions were calculated. The OBR decreased remarkably with improved SC compared to standard SC from $\text{mean} \pm \text{SD}$ 434.0 ± 698.3 to 137.9 ± 182.3 , the median decreased from 171.6 to 82.6. Changes were statistically highly significant ($p < 0.01$). The image noise slightly decreased and the SNR in all regions slightly increased with improved SC compared to standard SC. Changes in image noise and SNR are statistically not significant [Lindemann et al., 2019a].

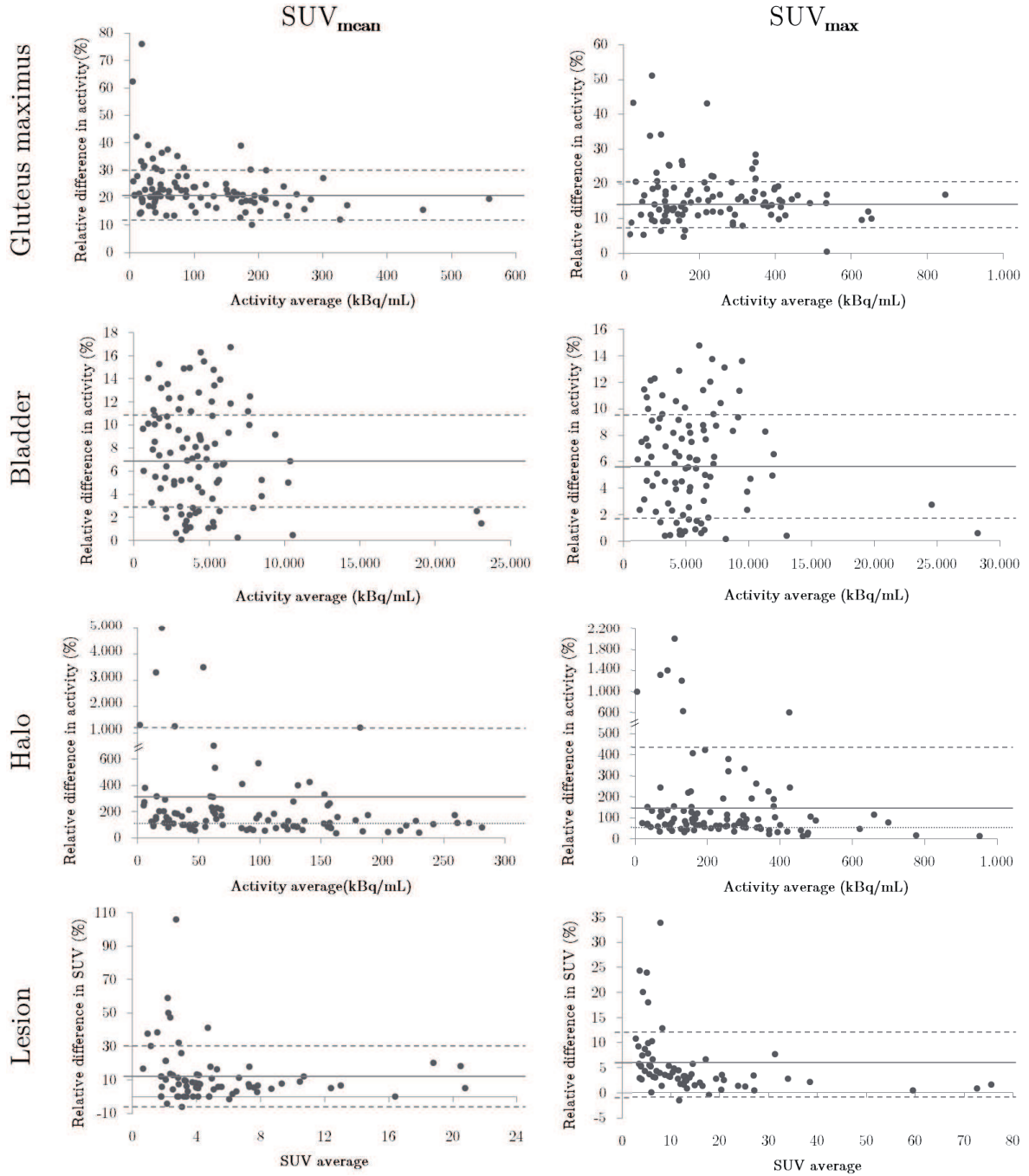


Fig. 3.12: Bland-Altman plots show the relative difference in measured standardized uptake values (SUV_{mean} , SUV_{max}) in the gluteus maximus, the bladder, the halo margin and in all 74 detected lesions using standard and un-renormalized scatter correction (SC). The solid lines mark the mean value, the dashed lines represent the limits of agreement (standard deviation) and the dotted lines mark the median. Note the overall gain in SUV values due to un-renormalized SC, especially with considerable gain in SUV within the halo margin [Lindemann et al., 2019a].

3.3.2 Lesion detection

In total, 74 congruent lesions could be detected in all 100 data sets for both reconstructions. Thus, no lesion was completely missed due to improper SC. The lesion detectability score was rated equally as mean \pm SD 2.5 ± 0.6 (discernible to clearly visible) in both reconstructions, regardless of the halo artifact. Using standard or un-renormalized SC seems to have no impact on lesion visibility or lesion detection .

The location of the lesions were characterized as detected inside (38 lesions) or outside (36 lesions) the halo margin. Relative differences in SUV_{mean} and SUV_{max} between standard and improved SC were calculated for both categories. The mean \pm SD increase in SUV_{mean} was $17.5 \pm 20.5\%$ for lesions inside the halo margin and $6.9 \pm 8.7\%$ for lesions outside the halo margin. The mean increase in SUV_{max} was $7.4 \pm 7.4\%$ for lesions inside the halo margin and $3.5 \pm 3.1\%$ for lesions outside the halo margin [Lindemann et al., 2019a].

Fig. 3.13 shows a patient example with three detected lesions inside the halo margin. The halo artifact could be reduced from a severe halo presence (grade 4) to no halo presence (grade 0) using improved SC compared to standard SC. Therefore, image quality could be inherently increased, whether there is no impact on lesion detectability and visibility with improved SC. The relative difference in SUV_{mean} was 47.7% for the lesion at the right ischium, 32.0% for the lesion at the right pubis and 50.0% for the lesion at the left pubis [Lindemann et al., 2019a].

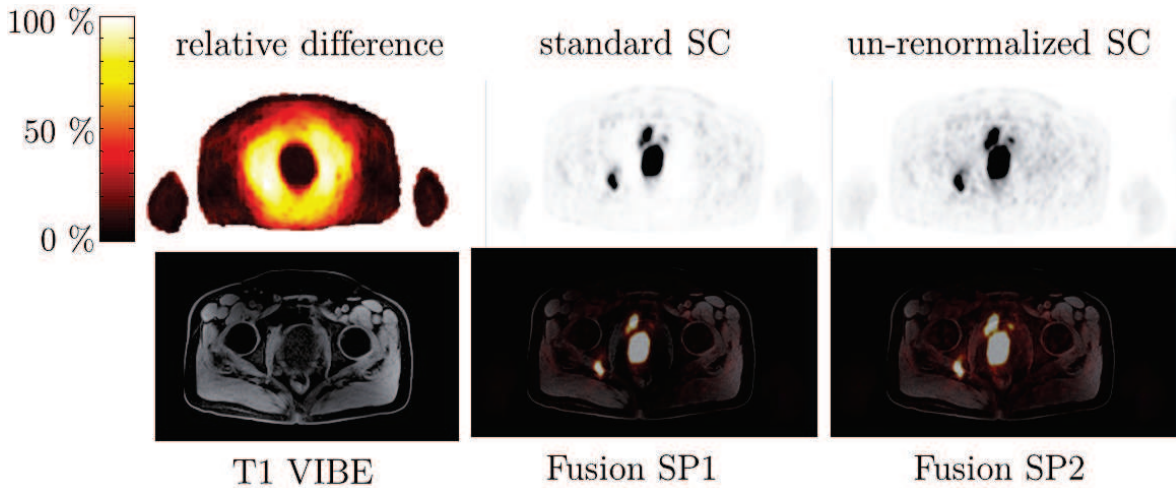


Fig. 3.13: Patient example with three detected lesions in PET data, an axial T1-weighted VIBE MR sequence and fusion images with PET data. Relative difference between standard and un-renormalized scatter correction (SC) show the artifact-reducing impact of un-renormalized SC. The halo artifact was reduced from severe halo presence (grade 4) to no halo artifact (grade 0) using improved SC. Relative differences up to 50% in SUV_{mean} in the lesions were calculated [Lindemann et al., 2019a].

In Fig. 3.14 PET images of two patient examples are shown reconstructed with a 4 and 10 minute time interval using standard and improved SC. The halo artifact could be reduced in both patient examples and in both time intervals using un-renormalized SC. All lesions could be detected in both patients in all reconstructions. However, comparing the lesion visibility of the marked lesion in each patient at the 4 minute time interval, the lesion is more faint in the PET image corrected with standard SC than in the PET image corrected with improved SC. The visibility score decreased from discernible to equivocal in patient example 1 and from clearly visible to discernible in patient example 2 in the 4 minute time interval using standard SC [Lindemann et al., 2019a].

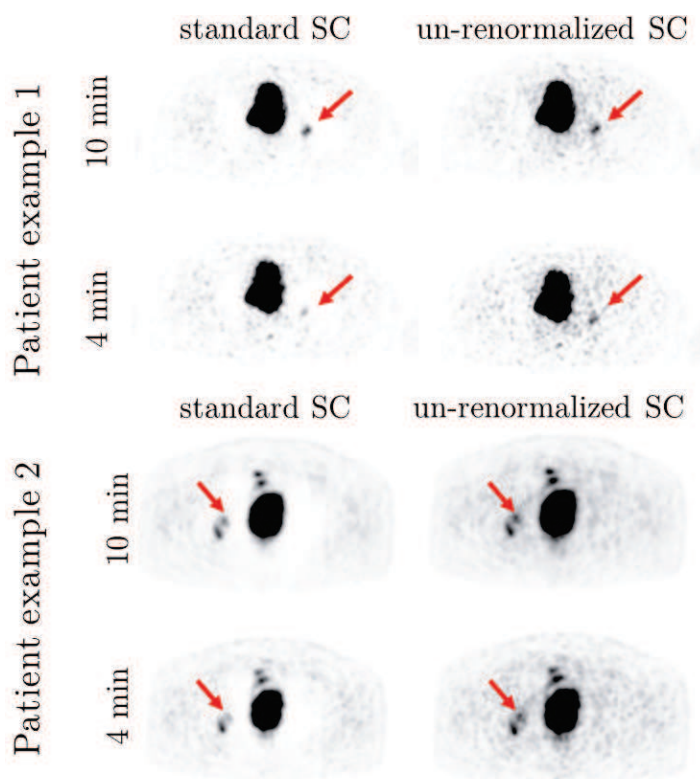


Fig. 3.14: Evaluation of the impact of PET acquisition time on lesion visibility. Axial PET images of two patient examples with lesions present in the halo margin. For each patient 10 and 4 minute PET time intervals were reconstructed using both standard and un-renormalized scatter correction (SC). In both time intervals for both patients, the halo artifact was significantly reduced with improved SC. While all lesions could be detected in all reconstructions, in the 4 minute time interval the visibility of the marked lesions (red arrow) decreased in the standard scatter corrected PET image compared to improved scatter corrected data and compared to the 10 minute interval [Lindemann et al., 2019a].

3.4 Fast PET/MRI: PET image quality vs. PET acquisition time

3.4.1 Image quality parameters

In Tab. 3.5 the analysis of PET image quality including the image quality score, image noise for different regions, SNR, CNR and SUVs in all lesions for different PET time intervals are shown. While the image noise increased with shorter PET acquisition times, the image quality score, SNR and CNR decreased with shorter PET acquisition time. SNR, CNR and image noise show no significant changes between 3 and 4 minutes per bed PET acquisition time, but with shorter PET time intervals the changes in image quality are significant. SUV_{mean} exhibits no significant changes between 1 and 4 minutes per bed PET acquisition time, while changes in SUV_{max} are significant between 1 and 4 mpb [Lindemann et al., 2018].

In all patients, a total of 91 congruent lesions were detected in the 4 minute PET time interval serving as a reference. 20 lesions are located in the head/neck area, 39 lesions in the thorax, 8 lesions in the abdomen and 24 lesions in the pelvis or upper thighs. An equal number of congruent lesions were also detected in the 3 and 2 minute PET time interval. Due to poor image quality, in total 2 lesions in 2 patients could not be detected in the 1 minute PET time interval. One lesion, which could not be detected in the 1 minute PET time interval, was a lymph node lesion in the left mammaria flow area. The patient had a BMI of 32 kg/m^2 , 3.1 MBq/kg radiotracer activity was applied and the PET/MRI measurement of this patient started 148 minutes post injection. The CNR is with 10.3 at 4 mpb significant lower than the average CNR over all patients (26.6). The other lesion, which could not be detected in the 1 minute PET time interval, was a lymph node lesion left cervical. The patient had a BMI of 22 kg/m^2 , 3.5 MBq/kg radiotracer activity was applied and the PET/MRI measurement of this patient started 114 minutes post injection. The image noise with 58% (blood pool) at 1 mpb is significant higher than the average image noise over all patients (42%) [Lindemann et al., 2018].

PET acquisition time [mpb]	image quality score (grading 0-3)	image noise (blood pool) [%]	image noise (liver) [%]	image noise (spleen) [%]	image noise (gluteus maximus) [%]	SNR	CNR	SUV _{mean}	SUV _{max}
4	2,4 ± 1,1	22,2 ± 10,3 (3,2 - 60,0)	18,2 ± 6,8 (5,9 - 40,0)	16,4 ± 7,8 (6,1 - 51,3)	19,3 ± 10,1 (7,8 - 45,1)	13,1 ± 2,7 (3,2 - 22,1)	26,6 ± 8,1 (7,7 - 69,3)	7,2 ± 2,4 (1,8 - 27,1)	9,4 ± 6,2 (1,9 - 36,5)
3	2,1 ± 1,2	26,0 ± 12,2 (10,0 - 71,4)	19,3 ± 7,1 (7,1 - 40,0)	19,0 ± 6,9 (5,7 - 47,7)	23,7 ± 9,0 (10,1 - 51,0)	12,9 ± 2,1 (4,2 - 19,6)	22,9 ± 11,7 (5,5 - 57,1)	6,9 ± 1,7 (1,7 - 22,2)	9,4 ± 6,4 (1,9 - 36,5)
2	2,0 ± 1,2	33,6 ± 10,6 (11,1 - 83,3)	25,0 ± 9,9 (10,5 - 60,0)	22,6 ± 10,4 (12,5 - 50,8)	32,6 ± 11,5 (12,0 - 61,3)	10,4 ± 1,6 (2,7 - 16,0)	20,8 ± 9,2 (4,1 - 61,0)	7,0 ± 2,8 (1,1 - 17,4)	9,7 ± 6,4 (1,9 - 37,8)
1	1,8 ± 1,3	42,1 ± 14,9 (16,7 - 90,9)	32,9 ± 12,0 (13,3 - 60,0)	30,5 ± 13,1 (12,5 - 60,0)	49,5 ± 16,7 (18,3 - 70,4)	9,3 ± 1,9 (1,9 - 13,3)	20,5 ± 9,9 (3,4 - 51,6)	6,8 ± 2,2 (1,1 - 20,1)	10,2 ± 6,4 (2,0 - 37,0)

Tab. 3.5: Lesion characterization and image quality analysis for different PET list-mode data reconstruction intervals. Values are presented in mean ± standard deviation (SD) and (range). PET acquisition time is given in minutes per bed (mpb). Image quality was graded from 0 = non-diagnostic to 3 = good image quality. Signal-to-noise ratio (SNR), contrast-to-noise ration (CNR) as well as standardized uptake value (SUV_{mean}), SUV_{max}) were calculated [Lindemann et al., 2018].

In Fig. 3.15 a patient example with consistently high image quality over all PET time intervals is shown. The patient is a 14-year-old child with a rather low BMI of 16.2 kg/m^2 , the PET/MRI examination started with 63 minutes early after radiotracer injection and a rather high radiotracer activity was applied with 5.4 MBq/kg . The image quality score is rated as good (IQS 3) even for shorter PET time intervals. The image noise (blood pool) slightly increased with shorter PET acquisition times (18.7% at 4 mpb, 20.0% at 3 mpb, 22.3% at 2 mpb, 23.7% at 1 mpb). The SNR slightly decreased with shorter PET acquisition times (14.8 at 4 mpb, 13.7 at 3 mpb, 10.3 at 2 mpb, 10.0 at 1 mpb). Also the CNR slightly decreased with shorter PET acquisition times (28.3 at 4 mpb, 23.1 at 3 mpb, 22.0 at 2 mpb, 19.9 at 1 mpb). No significant changes in SUV_{mean} and SUV_{max} are measurable in all PET time intervals. The marked lesion with the lowest SUV_{max} of 9.0 is detectable in all PET reconstructions. In this patient example, the image noise was lower than the average over all patients, while CNR and SNR were higher than the average over all patients. The same trend of decreased image noise and increased CNR and SNR was also measured in five other patients. These patients have all a BMI lower than 20 kg/m^2 and post injection times lower than 80 minutes [Lindemann et al., 2018].

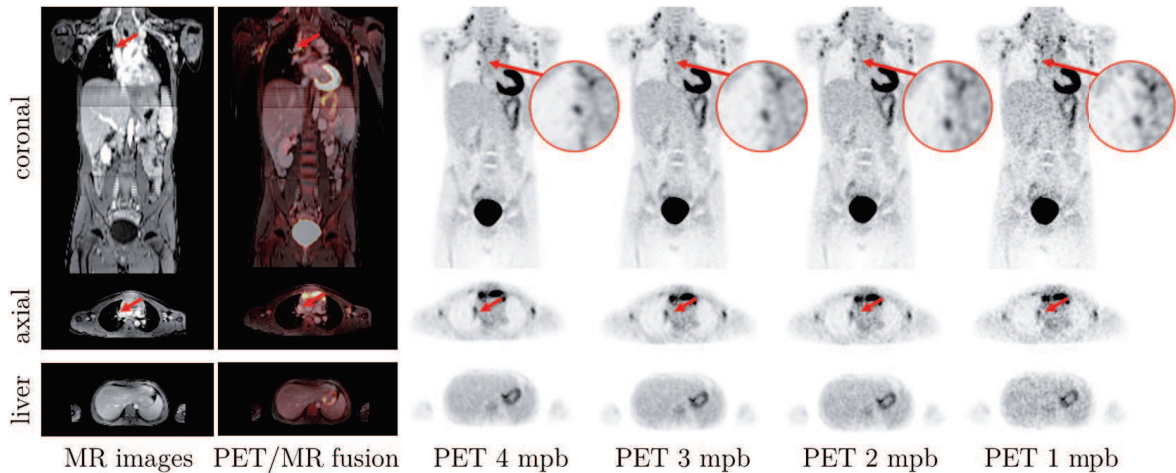


Fig. 3.15: Patient example of consistently good image quality. MR images, PET/MR fusion images and PET images with 4, 3, 2 and 1 minutes per bed (mpb) PET acquisition time are shown in coronal and axial orientation. The lesion is marked (red arrow). In addition an axial slice of the liver is shown. Discrete stripe artifacts in MR images result from coronal reformats at the positions where the transaxially acquired slice stack of two neighbored bed positions are merged. Image noise (blood pool) increases from 18.7% at the 4 mpb to 23.7% in 1 mpb reconstruction. The CNR decreases from 28.3 at 4 mpb to 19.9 at 1 mpb. The SNR decreases from 14.8 at 4 mpb to 10.0 at 1 mpb [Lindemann et al., 2018].

In Fig. 3.16 a patient example of significantly decreasing PET image quality with shorter PET acquisition times are shown. The patient is 74 years old with a rather high BMI of 32.1 kg/m^2 , the PET/MRI examination started with 148 minutes late after radiotracer injection and a rather low radiotracer activity was applied with 3.1 MBq/kg . The image quality score decreased for shorter PET time intervals from moderate (IQS 2) to non-diagnostic (IQS 0). The image noise (blood pool) considerably increased with shorter PET acquisition times (28.1% at 4 mpb, 38.9% at 3 mpb, 42.3% at 2 mpb, 58.1% at 1 mpb). The SNR decreased with shorter PET acquisition times (6.6 at 4 mpb, 5.3 at 3 mpb, 3.6 at 2 mpb). Also the CNR significantly decreased with shorter PET acquisition times (21.1 at 4 mpb, 19.7 at 3 mpb, 15.4 at 2 mpb). The marked lesion with a SUV_{max} of 9.0 in the 4 minute time interval is not detectable in the 1 mpb reconstruction. In this patient example, the image noise was higher than the average over all patients, while CNR and SNR were lower than the average over all patients. [Lindemann et al., 2018].

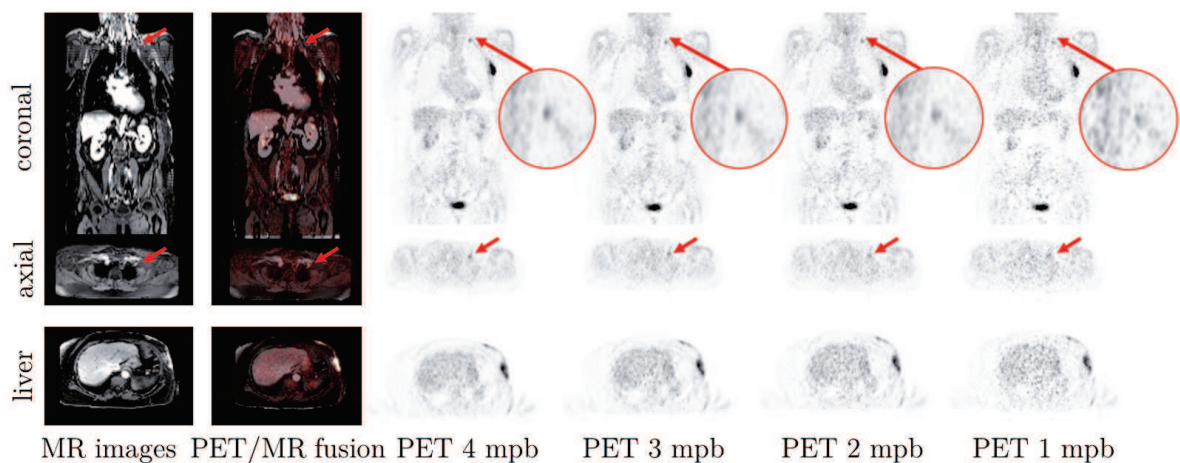


Fig. 3.16: Patient example of decreasing image quality. MR images, fusion images and PET images with 4, 3, 2 and 1 minutes per bed (mpb) PET acquisition time are shown in coronal and axial orientation. In addition an axial slice of the liver is shown. The lesion is marked (red arrow). Note that the marked lymph node lesion is not well detectable in PET images with 1 min timeframe. Discrete stripe artifacts in MR images result from coronal reformats at the positions where the transaxially acquired slice stack of two neighbored bed positions are merged. Image noise (blood pool) increases from 28.1% at the 4 mpb to 58.1% in 1 mpb reconstruction. The CNR decreases from 21.1 at 4 mpb to 15.4 at 2 mpb. The SNR decreases from 6.6 at 4 mpb to 3.6 at 2 mpb [Lindemann et al., 2018].

3.4.2 Correlation with image quality determinants

The patient cohort in this study is heterogeneous, thus the variance of some important biological image quality determinants is large. Besides PET acquisition time and applied activity, patients' BMI and the time between injection and examination (post injection time) might also have an impact on PET image quality. Tab. 3.6 shows the quantitative impact of different determinants/subgroups (BMI, post injection time, applied activity) on PET image quality for different PET time intervals. The subgroups are built by arranging the PET data in three categories: BMI, post injection time and applied radiotracer activity. Each value in each category is compared to the "mean value" and the PET data is arranged in "category $> \emptyset$ " or "category $< \emptyset$ ". For each subgroup the image quality parameters were analysed for different PET acquisition times. Tab. 3.6 depicts that a low BMI, a short time interval between activity injection and PET/MR examination and a higher applied activity are optimal conditions to obtain high PET image quality, regardless PET acquisition times. Considering the image noise for example, the mean value over all patients at 1 mpb is 42.1 %. The image noise decrease with BMI $< \emptyset$ (25.5 kg/m²) to 39.6 %, while image noise increase in patients with BMI $> \emptyset$ to 43.1 %. Another example is the effect of shorter post injection times on PET image quality with regard to SNR. Shorter post injection times in primary PET/MR examinations increase the SNR from mean value 9.3 to 10.6 at 1 mpb PET time interval, and thus results in better PET image quality. A further example is the effect of applied activity on CNR. The CNR decreases from mean value 20.5 to 20.0 at 1 mpb PET time interval with activity $< \emptyset$ [Lindemann et al., 2018].

	1 min			2 min			3 min			4 min		
	image noise (blood pool) [%]	SNR	CNR	image noise (blood pool) [%]	SNR	CNR	image noise (blood pool) [%]	SNR	CNR	image noise (blood pool) [%]	SNR	CNR
BMI < \emptyset	39,6 ± 12,9	9,7 ± 1,6	20,8 ± 6,9	31,8 ± 10,1	11,3 ± 1,4	22,0 ± 6,5	24,5 ± 13,1	13,3 ± 1,9	23,8 ± 10,3	20,2 ± 11,1	13,9 ± 2,9	27,4 ± 8,1
primary PET/MR	40,0 ± 14,1	10,6 ± 1,9	21,5 ± 6,1	31,5 ± 10,3	10,9 ± 2,0	21,4 ± 8,0	25,6 ± 12,8	12,9 ± 2,1	23,1 ± 9,8	21,0 ± 10,7	13,3 ± 2,7	27,4 ± 7,7
activity > \emptyset	39,2 ± 12,2	9,9 ± 1,9	20,6 ± 9,0	30,6 ± 11,6	11,1 ± 1,9	20,8 ± 8,2	23,8 ± 11,9	14,0 ± 2,4	23,3 ± 10,7	19,7 ± 11,0	13,6 ± 3,0	26,9 ± 8,0
mean value	42,1 ± 14,9	9,3 ± 1,9	20,5 ± 9,9	33,6 ± 10,6	10,4 ± 1,6	20,8 ± 9,2	26,0 ± 12,2	12,9 ± 2,1	22,9 ± 11,7	22,2 ± 10,3	13,1 ± 2,7	26,6 ± 8,1
BMI > \emptyset	43,1 ± 11,3	7,8 ± 1,2	18,9 ± 11,7	33,9 ± 12,7	9,2 ± 1,8	19,1 ± 10,4	29,1 ± 13,6	12,7 ± 2,0	20,8 ± 11,4	24,9 ± 12,9	11,8 ± 2,5	26,0 ± 10,1
non primary PET/MR	43,9 ± 13,9	9,1 ± 1,5	19,0 ± 10,6	33,2 ± 10,3	10,0 ± 1,4	19,0 ± 11,1	26,9 ± 14,4	12,8 ± 1,7	21,1 ± 11,4	22,9 ± 12,2	12,0 ± 2,9	25,9 ± 9,3
activity < \emptyset	48,0 ± 13,1	8,9 ± 0,9	20,0 ± 11,2	34,6 ± 10,6	9,9 ± 1,4	19,7 ± 10,1	28,4 ± 12,3	11,7 ± 1,8	22,5 ± 12,2	25,1 ± 11,8	12,6 ± 2,1	26,4 ± 9,6

Tab. 3.6: Image quality parameters given in mean \pm standard deviation (SD) for different PET reconstruction times are shown. The row “mean value” represents the average over all patients. Subgroups are built to show the impact of different body-mass-indexes (BMI), post injection times and applied activity of the image quality parameters image noise, signal-to-noise ratio (SNR) and contrast-to-noise ratio (CNR) [Lindemann et al., 2018].

Tab. 3.7 lists the correlation coefficients between image quality determinants PET acquisition time, applied activity, post injection time and BMI on PET image quality parameters SNR, CNR and image noise (blood pool). PET acquisition time and applied activity showed a highly significant ($p < 0.01$) positive correlation on SNR and CNR and a highly significant ($p < 0.01$) negative correlation on image noise. Post injection times exhibited no significant correlation between any of the image quality parameters, while the BMI showed a significant negative correlation on SNR and a significant positive correlation on image noise.

	acquisition time	activity	post injection time	BMI
SNR	0.746	0.756	-0.173	-0.584
CNR	0.616	0.560	-0.236	-0.319
image noise	-0.741	-0.648	0.311	0.661

Tab. 3.7: The correlation coefficients between the image quality determinants PET acquisition time, applied activity, post injection time and body-mass-index (BMI) on PET image quality parameters signal-to-noise ratio (SNR), contrast-to-noise ratio (CNR) and image noise (blood pool) are given [Lindemann et al., 2018].

4 Discussion

4.1 Attenuation correction

There is a growing interest in PET/MRI for several clinical applications such as whole-body oncology, cardiovascular imaging, the detection of prostate cancer or even MR-based radiotherapy treatment planning [Schaarschmidt et al., 2015; Grueneisen et al., 2015a; Schwenzler et al., 2012; Rischpler et al., 2013; Nensa et al., 2013; Afshar-Oromieh et al., 2014; Wetter et al., 2013; Bouchelouche et al., 2010; Tanner et al., 2000; Paulus et al., 2014, 2016]. Proper MR-based AC in clinical PET/MRI is essential to ensure best possible diagnostic image quality and accurate PET quantification also for very large FOVs. Furthermore, other PET correction methods like the SC rely on accurate AC. An inherent limitation of currently established MR-based AC methods is the limited MR FOV. Most often patients' arms are truncated in the MR-based AC-maps, which systematically limits accurate PET quantification in PET/MRI [Delso et al., 2010]. The aim of this study was to implement and evaluate a MR-based truncation correction method called HUGE for whole-body ^{18}F -FDG PET/MRI. To further extend the clinical application spectrum in PET/MRI the quantitative impact of improved AC including HUGE truncation correction and an additional bone model approach was demonstrated on ^{18}F -FDG cardiac PET/MRI data.

4.1.1 CT as a reference

A major limitation for the evaluation of improved MR-based AC methods in PET/MRI is the missing reference for a "real" AC-map and therefore, accurate PET values. To investigate the effect of truncation correction using HUGE on PET phantom data a CT-based AC-map was used serving as a reference standard for an accurate AC-map. The phantom housing in the CT-based AC-map was removed for comparability reasons, since in MR-based AC phantom housing is not considered. Both truncation correction methods, HUGE and MLAA, reduced the distortion artifacts in the Dixon-VIBE AC-map. While HUGE AC-map resulted in plausible phantom contouring, MLAA tended to overestimate the phantom arms. Both methods increased the PET signal

compared Dixon-VIBE AC. Whereas the increase in PET signal due to HUGE was in a good agreement to the CT-based reference, MLAA corrected PET data led to higher differences compared to the CT-based reference. Remaining differences between HUGE AC and CT AC could be explained by the general limitations of MR-based AC. Phantom fluids are not equivalent to MR signal in body tissue. Thus, fat-water swaps, signal drop-outs or segmentation with incorrect LAC might lead to divergent PET signal compared to the CT reference. The phantom setup is with 58 cm comparably large in length (left-right extend) and thus, close to the limit of the extended MR FOV of 60 cm. HUGE truncation correction compensates B_0 inhomogeneities with an optimized read-out gradient in x -direction (left-right). Bias caused in y -direction (anterior-posterior) are not compensated by HUGE. In the HUGE AC-map the phantom arms with their large diameter are not perfectly round in shape compared to the CT reference [Lindemann et al., 2017].

In patient examinations CT data could not be used as a reference for several reasons: A CT-based AC-map from a preceded PET/CT is often not available. Further, the patient positioning between PET/MR and PET/CT is different. Data acquisition in PET/CT is performed with the patients' arms up (in a position above the heads) and in PET/MR the data is acquired with the patients' arms down (arms resting beside the bodies). Thus, a registered CT-based AC-map without arms could not be referred to as a ground truth. Furthermore, radiotracer kinetics, enhancement and washout over time due to different post injection times makes an accurate quantitative comparison between PET/MR and PET/CT data challenging, if not impossible. In patient measurements a relative comparison between standard and improved MR-based AC was made. One advantage of this method is that identical PET data was used for all reconstructions eliminating changes in tracer kinetics over time and no registration issues between AC-maps and PET data can occur. To quantify the impact of truncation correction on PET data compared to standard MR-based AC, the NAC PET data was segmented to determine the true body volume. This served as a basis of assessment of the performance of HUGE and MLAA.

4.1.2 HUGE truncation correction

Independent of patients' BMI, the Dixon-VIBE AC-maps in all patient datasets (whole-body and cardiac PET/MRI study) showed truncation artifacts along the arms. Due to truncation correction using HUGE all AC-maps increased in volume and distortion artifacts at the edges of the MR FOV were reduced. Based on the segmentation of NAC PET data serving as the reference for non-truncated body volume, the truncation in the AC-maps was reduced from ca. -12 % using standard Dixon-VIBE AC to ca. -1.5 %

using HUGE. Thus, HUGE AC resulted in a high accuracy with a slight underestimation in body volume.

Not only providing accurate and reliable body contouring, HUGE performed robust in each patient. One single arm in one patient (cardiac study) was missed out in the HUGE AC-map. After qualitative visual inspection of HUGE MR raw data in this specific case, the truncation correction itself performed well. The automatic segmentation of the HUGE MR raw data by the PET/MR system failed. Further, HUGE is a fully MR-based approach to improve AC in PET/MRI, thus it is independent of the choice of radiotracer and its distribution and kinetics. Consequently, HUGE provided accurate truncation correction in a ^{124}I patient example.

The average gain in AC-map volume compared to standard Dixon-VIBE AC is 5.5% for HUGE and 9.0% for MLAA (whole-body and cardiac PET/MRI study), which is in good agreement with previous studies [Blumhagen et al., 2014]. Comparing the quantitative impact of truncation correction on PET signal in whole-body PET/MRI, the PET signal increased by 4.2% for HUGE and 4.6% for MLAA. Despite the systematic overestimation in AC-map volume due to MLAA, the impact of both truncation correction methods on gains in PET signal is comparable. Relative difference images in the whole-body PET/MRI study already exhibited, that especially in the thorax a gain in PET signal due to truncation correction is noticeable, and thus might have potential impact on PET quantification in cardiac PET/MRI studies in the future. This assumption was confirmed with regard to the results of the cardiac study. Comparing the increase in global activity between standard Dixon-VIBE AC and HUGE AC (6.1%), respectively MLAA AC (8.3%), in the heart with the increase in PET signal in the whole-body PET/MRI study, it is obvious that the thoracic region benefits more from enhanced AC. Adding volume of soft tissue in patients' arms relative to the less attenuating large volume of lung tissue leads to substantial relative gains in total tissue attenuation in the thorax. Therefore, cardiac PET/MRI profits from the impact of both truncation correction methods, either HUGE or MLAA [Lindemann et al., 2019b].

When considering each patient individually, the increase in PET signal due to truncation correction, either HUGE or MLAA, strongly depends on the position of the lesion in patients' body and relative to the distorted regions. The highest relative increase in PET signal occurred in lesions close to added tissue volume along the, otherwise, truncated arms. In the whole-body study, maximal relative differences in SUV_{mean} between standard Dixon-VIBE AC and improved AC were measured in lesions close to truncations (9.3% for HUGE, 11.9% for MLAA). The quantitative evaluation of the radiotracer injection sites, which are (mostly) located in truncated areas in patients' arm, showed maximal relative differences up to 40%. The same trend was exhibited

in the cardiac study. Here, maximal relative differences of 18.8% for HUGE + bone AC and 19.8% for MLAA AC were observed in the apical segment. The slight increase of relative difference in PET signal from base to apex may emerge from patients' arm posture in the PET/MR system. The upper arm body region exceeds the limited MR FOV more often, and therefore more tissue volume is added by applying HUGE in the AC-map here [Lindemann et al., 2019b]. A similar dependency on lesion position and increased PET signal was presented in a study, where the impact of additional bone information in the AC-map in PET/MRI was investigated [Paulus et al., 2015].

The MR-based truncation correction method HUGE combined with CTM worked robust and effectively reduced distortions along patients arms by extending the MR FOV in x -direction tested in whole-body PET/MRI examinations including patients with a broad range of body constitution, oncological findings and examinations with non-FDG radiotracers. Thus, the implementation of HUGE presented in the first study improves the MR-based AC, and therefore PET quantification in whole-body PET/MRI. The robustness of the method and the straightforward workflow adding only 40 to 90 seconds to the overall whole-body PET/MRI protocol now allows for routine clinical use of HUGE truncation correction on integrated PET/MR hybrid systems. The results of this study proved that especially in the thorax a gain in PET signal due to truncation correction is noticeable, and thus might have potential clinical impact on PET/MRI studies in the future, namely quantitative cardiac PET/MRI, breast cancer imaging or tumour and metastases staging of bronchial carcinoma [Rischpler et al., 2013; Schindler, 2016; Grueneisen et al., 2015a; Tabouret-Viaud et al., 2015; Schaar-schmidt et al., 2015; Huellner et al., 2016].

The successful integration of HUGE truncation correction in MR-based AC was the basis of further investigations on clinical impact in quantitative cardiac PET/MRI presented in the second study [Lindemann et al., 2017]. While currently cardiac PET/MR studies are mostly analysed qualitatively in clinical routine, PET is well known to yield accurate quantification of global and regional myocardial perfusion and blood flow at stress and rest using PET/CT [Lautamäki et al., 2009]. The quantitative assessment of cardiac PET/MR studies depends on a precise and accurate MR-based AC method to ensure best possible diagnostic image quality and PET quantification [Schindler, 2016; Hunter et al., 2016; Rischpler et al., 2012; Bravo et al., 2018; O'Doherty et al., 2017]. It was shown in our study that improved AC including HUGE truncation correction and bone segmentation increase the overall gain in PET signal in the left ventricle myocardium and results in a homogeneous PET signal distribution across the myocardium [Lindemann et al., 2019b].

4.1.3 MLAA truncation correction

Due to truncation correction using MLAA all AC-maps increased in volume and distortion artifacts at the edges of the MR FOV were reduced. Based on the segmentation of NAC PET data serving as the reference for non-truncated body volume, the truncation in the standard AC-maps was reduced to ca. 8% using MLAA. Whereas HUGE resulting in plausible body contouring, MLAA overestimated the truncated AC-map volume in every patient (whole-body and cardiac PET/MRI study). The systematic overestimation of AC-map volume due to inaccurate PET contour detection using MLAA is in agreement with previous studies [Blumhagen et al., 2014]. This overestimation is partly compensated by applying reduced LAC values to the added regions in the AC-map.

Another restriction of the PET-based MLAA AC in the whole-body PET/MRI study was the failure of reconstructing an AC-map in a non-FDG patient. MLAA truncation correction relies on the accumulation of radiotracer in patients' skin to reliably derive patients' body contour based on PET data. In patients examined with a non-FDG radiotracer, as in this case ^{124}I , PET-based AC might be limited due to improper contour detection from emission data.

The Siemens Biograph mMR PET/MR system is not time-of-flight (TOF) capable. Several studies showed that MLAA benefits from TOF capability [Rezaei et al., 2012; Mehranian and Zaidi, 2015; Boellaard et al., 2014], and thus the implementation of the MLAA algorithm evaluated in these studies (whole-body and cardiac PET/MRI study) may only provide results with intermediate accuracy with regard to PET-based contour detection. Applying TOF reduces the sensitivity of PET reconstruction to AC errors and in this context of MLAA. TOF information also has the ability to stabilize the joint estimation problem [Rezaei et al., 2012]. To estimate the attenuation from PET data has the advantage to ensure a correct match regarding to photon energy, patient position and probably a good match in the presence of motion blurring (breathing and heart motion) [Lindemann et al., 2019b]. In this context, the overestimation in AC-map volume due to MLAA and the failure to reconstruct an AC-map in the non-FDG example might be overcome using additionally TOF information.

4.1.4 Bone correction, artifacts and BMI

Besides a limited MR FOV, another limitation in MR-based AC is the substitution of bone as soft tissue leading to a systematic underestimation in PET signal. For quantitative PET imaging, especially for myocardial PET perfusion imaging, a precise MR-based AC is important. Paulus et al. [2015] presented a bone model approach for AC in PET/MRI, which was also evaluated in this thesis on cardiac patient data. The decreased relative differences in polar plot segments 3, 4 and 9, 10 for HUGE only or

MLAA corrected data arise from missing bone information in the AC-map. Including the bone model in the MR-based AC, the PET signal distribution was homogeneous across the entire left ventricle myocardium. Seven patients showed bone artifacts in the AC-maps. No bone segmentation or mismatched bone segmentation might be caused by missing reference for registration of the bone model in the Dixon-VIBE MR images of these patients. In a patient example with failed bone segmentation, regional differences up to 6 % within the myocardium were measured when comparing bone AC to non-bone AC and thus, may affect the clinical reading [Lindemann et al., 2019b]. Lassen et al. [2017] also showed that AC-map artifacts affect quantitative assessment of patient data in PET/MRI. Here, regional differences up to 100 % were measured in the myocardium due to AC-map artifacts. Therefore, readers are advised to check the AC-maps for artifacts during cardiac PET/MR image assessment.

While truncation correction with HUGE worked relatively robust, MLAA tends to overestimate the AC-map volume in almost all patient data. Nevertheless, the majority of these observed AC-map artifacts did not affect clinical reading, but definitely had an impact on quantitative assessment of PET data.

While all Dixon-VIBE AC-maps showed truncation along the arms, these truncation artifacts tended to be higher in patients with a large BMI. A high BMI is often associated with overall large body dimensions exceeding the constraints of a conventional MR FOV. Thus, the general impact of truncation correction with HUGE or MLAA is intuitively larger in patients with a higher BMI compared to standard Dixon-VIBE AC, which is in agreement with previous studies [Blumhagen et al., 2014]. However, regarding the truncated AC-map volume and potential impact of HUGE or MLAA truncation correction on PET quantification, the overall patient dimension, and not exclusively the BMI, is the decisive factor [Lindemann et al., 2019b, 2017]. Truncation artifacts could be reduced with MR-based HUGE AC independent of patients' BMI. MLAA AC tended to perform better in patients with a lower BMI, while in patients with larger BMI the PET-based MLAA AC tended to overestimate the arm volume. This might suffer from improper random correction. The density distribution from random coincidences slightly increases towards the borders of the axial PET FOV, and thus random coincidences might be considered as true coincidences in the PET emission data, the base of MLAA reconstructions [Salomon et al., 2011].

4.2 Scatter correction

^{68}Ga -PSMA PET showed promising results in the detection of prostate cancer [Afshar-Oromieh et al., 2014; Noto et al., 2017; Lütje et al., 2016]. A challenge with highly specific radiotracers like PSMA is the halo artifact, which causes reduced PET signal around the urinary system. Inaccurate SC is a significant factor in the origin and extend of the halo artifact [Afshar-Oromieh et al., 2014; Heußer et al., 2017]. To ensure quantitative PET/MRI of prostate cancer using ^{68}Ga -PSMA, while maintaining best possible diagnostic image quality and accurate PET quantification a proper SC is needed. Therefore, the impact of improved SC was evaluated in ^{68}Ga -PSMA PET/MRI data of patients with prostate cancer.

4.2.1 Image quality and quantification

Improper SC is believed to be the reason for halo artifacts in ^{68}Ga -PSMA PET/MRI [Afshar-Oromieh et al., 2014]. By assessing non-scatter-corrected PET images, and thus virtually omitting the halo artifact, runs the risk of missing lesions. Furthermore, a quantitative assessment of the radiotracer uptake is impossible. Draining the bladder directly before PET examination might also reduce the presence of halo artifact. Both methods showed no relevant improvements with respect to the halo artifact [Afshar-Oromieh et al., 2017]. Therefore, a improved version of SC is essential to ensure best possible image quality and quantification.

The SC algorithms rely on an accurate AC-map of the patient. Especially the truncation artifacts along patients' arms in a standard Dixon-VIBE AC-map seem to have an impact on the presence of halo artifacts. Inaccurate AC due to the limited MR FOV, and thus truncation artifacts in the AC-map, leads to an increased appearance of the halo artifact [Afshar-Oromieh et al., 2017; Noto et al., 2017]. Therefore, the latest MR-based AC methods including HUGE truncation correction and bone segmentation [Oehmigen et al., 2017], are used as a proper foundation for the SC algorithm and further reduce the appearance of halo artifacts in this study [Lindemann et al., 2019a].

Using un-renormalized SC inherently improved PET image quality. The presence of halo artifact could be reduced from moderate-strong (grade 2-3) to slight-none (grade 0-1) with improved SC over standard SC. Also the quantitative assessment exhibited a strong improvement using un-renormalized SC. The average SUV_{mean} in the halo margin increased by 325%. This considerably affect the quantitative assessment of prostate cancer in ^{68}Ga -PSMA PET/MRI, especially lesions inside the halo margin benefit from improved SC with average relative differences in SUV_{mean} of 17.5%.

The high interest in ^{68}Ga -PSMA PET for staging, therapy and follow-up of prostate cancer is impaired by the presence of the halo artifact [Afshar-Oromieh et al., 2016; Eiber et al., 2016; Schwarzenboeck et al., 2017]. Using improved SC is an important pre-condition for the qualitative and quantitative clinical assessment of prostate cancer. Even if quantitative ^{68}Ga -PSMA PET including SUV measurements is not yet fully established for clinical lesion quantification and treatment response assessment, the results of this study using un-renormalized SC are promising and could be a proper foundation for quantitative assessment. The PET signal correlates with the absolute PSMA expression level. Recently, several groups proposed standardized interpretation criteria and lesion follow-up for PSMA PET. Therefore, reliable SUV measurements may become a critical part of future interpretation systems and clinical assessment [Lückerath et al., 2018; Eiber et al., 2018; Rowe et al., 2018]. The reduction or even elimination of the halo artifact is an important precondition for accurate quantification and standardization in this context [Lindemann et al., 2019a].

Halo artifacts can occur in both hybrid systems, PET/CT and PET/MR, but particularly challenges the PET/MRI of the prostate. The implementation of the SSS with absolute scaling and un-renormalized estimated scatter presented in this study is a robust SC method relevant for ^{68}Ga -PSMA PET/MRI, but might be also relevant for PET/CT to further reduce the halo artifact. Multi-scatter methods, which are still under development, might further improve ^{68}Ga -PSMA PET/MRI and might support the clinical assessment of prostate cancer in the future [Watson et al., 2018].

Another physical challenge beside the high specificity of PSMA with potential impact on PET quantification is the ^{68}Ga decay. Prompt gamma rays with an energy of 1077 keV are emitted simultaneously with positron emission. When the prompt gamma rays are scattered before detection, their energy level might fall into the energy window of the PET system, and thus a coincidence between prompt gamma rays and annihilation photons cannot be differentiated from a true coincidence. This might lead to scatter overestimations and hampers the PET quantification and image quality. However, it was shown that prompt gamma rays only have a limited effect on the appearance of the halo artifact in ^{68}Ga -PSMA PET/MRI [Heußner et al., 2017; Noto et al., 2017]. In addition, the prompt gamma branching fraction for ^{68}Ga is only 3%. Just a fraction of these will be detected in coincidences with the annihilation photons. Thus, the prompt gamma background for ^{68}Ga is low and does not have a significant impact on the absolute scatter compared to other isotopes like ^{82}Rb , where prompt correction has an inherent impact on PET quantification [Watson et al., 2008].

4.2.2 Lesion detection

The un-renormalized SC inherently improved PET image quality by reducing the presence of the halo artifact. However, the choice of SC method had no impact on lesion detection in this study. Independent of the choice of SC method, no lesion was missed out due to halo artifact. All lesions in all reconstructions could be detected with equal visibility ratings. The detected lesions in this patient cohort may not have been on the detection threshold, thus being not small or faint enough or close enough to the bladder, to be affected by the presence of the halo artifact.

In contrast to other studies in the past [Noto et al., 2017; Heußer et al., 2017], where the halo artifact impaired the lesion detection and visibility, in this study no impact on lesion detection with or without the presence of the halo artifact could be observed. A potential reason might be the different PET acquisition times, and thus count statistics. In previous studies, PET data was acquired for 4 minutes per bed station, while in this study the PET acquisition time for the pelvis was 10 minutes. A choice of different MR soft-tissue contrast (e.g. T1, T2 and diffusion-weighted imaging) was generated, and thus the prolonged MRI protocol allowed for extended PET data acquisition. The longer PET acquisition times are associated with better count statistics and may supported the detection of all lesions with equal visibility, even faint or small lesions, regardless of the presence of the halo artifact. Fig. 3.14 depicts the potential dependency of lesion visibility on PET acquisition time. Both PET time intervals, 4 minute and 10 minute, exhibited increased PET image quality using improved SC than standard SC. However, in the 10 minute PET time interval the marked lesion was visible equally despite the halo artifact around the bladder. In contrast to the 4 minute PET time interval, where the count statistic as expectable was inherently reduced. In this example, the overall lesion visibility decreased compared to the 10 minute PET time interval, especially using only the standard SC. Thus, the detection of faint or small lesions within the halo margin may be limited using short PET acquisition times in combination with non-optimized SC [Lindemann et al., 2019a].

In the context of fast PET/MRI, this potential dependency of lesion detection and PET acquisition time is an important aspect aiming at improved patient comfort with shorter PET/MRI acquisition times and optimized patient throughput. To ensure best possible image quality and accurate lesion detectability with reduced halo artifact even in short ^{68}Ga -PSMA PET/MRI protocols, an improved version of SC as presented in this study is mandatory.

4.3 Fast imaging

Generating various different MR soft-tissue contrasts dependent on the clinical indication, prolongs the overall PET/MR acquisition time. These rather long PET/MRI protocols inherently reduce the patient comfort patient throughput and were identified as the main limitation of PET/MRI compared to PET/CT [Gückel et al., 2015]. The trend towards fast whole-body PET/MRI eliminating redundant diagnostic information from MR contrast weightings runs the risk of decreased PET image quality and quantification. As shown in the last section 4.2, there is a potential dependency between PET acquisition time and lesion visibility. The aim for fast PET/MRI is to shorten the MR acquisition time, while maintaining diagnostic information and PET image quality. In this context and in preparation of future fast whole-body PET/MRI protocols, PET might be the time limiting factor in PET/MRI [Lindemann et al., 2018]. Thus, the aim of this study was to evaluate the impact of reduced PET acquisition times on PET image quality and PET quantification in whole-body ^{18}F -FDG PET/MRI.

4.3.1 Decreased PET image quality

As expected the PET image quality decreased with shorter PET acquisition times. The image noise increased, whereas SNR and CNR decreased from the 4 minute PET time interval to the 1 minute PET time interval. The image quality score also decreased with shorter PET acquisition time, but the 2 minute PET time interval was still rated as moderate, the second best out of four scores. Only the average image quality score from the 1 minute PET time interval was rated as poor. No significant changes in PET image quality was calculated between 4 and 3 minutes per bed. In contrast to the 1 minute per bed reconstruction, where PET image quality was inherently reduced. Regardless of decreasing image quality with shorter time intervals, no significant changes in SUVs were measurable. The image quality was sufficient to detect all congruent lesions in the 4, 3 and 2 minute PET time interval. Only in the 1 minute PET time interval, 2 lesions were missed out due to poor PET image quality. Thus, the 2 minute PET time interval permitted correct detection of all congruent lesions, and therefore, provides identical diagnostic information as the longer acquisition times of 3 and 4 minutes in this study [Lindemann et al., 2018].

The reconstruction of PET data with different time intervals allowed for a reproducible, controlled and systematic evaluation of PET image quality and quantity. Studies, which employ PET re-examination of patients, run the risk of numerous confounding factors when injecting radiotracer (e.g. different radiotracer wash-in and wash-out times, different tracer post injection times) making a systematic evaluation of

PET image quality at different time points challenging. However, the simple gating of PET list-mode data might be a limitation of this evaluation. Instead, the randomized under-sampling of list-mode data would additionally account for potential patient motion or cases, where high radiotracer kinetics are to be expected [Gatidis et al., 2016; Seith et al., 2017].

In recent studies [Kirchner et al., 2017b,a; Grueneisen et al., 2015b, 2016, 2017; Schwenzer et al., 2016], MR contrast weightings providing only redundant diagnostic information have been eliminated from the list of MR protocols to shorten the overall PET/MR acquisition time, while maintaining diagnostic information. Nevertheless, these PET/MRI acquisition time still lasts 4 minutes per bed position, thus simultaneous MRI could be considered as the time limiting factor. The ultimate short whole-body PET/MR protocol is the dual use of the Dixon-VIBE AC sequence also as anatomic MR imaging correlate without adding further diagnostic MR sequences, which was investigated by Eiber et al. [2011]. The conclusion of this study was that the Dixon-VIBE AC provides comparable results as a low-dose PET/CT [Eiber et al., 2011]. The diagnostic information gained from such a fast exam is, however, debatable. Theoretically, the duration of such a ultimate short PET/MRI protocol could be 19 seconds per bed position (acquisition time for a low spatial resolution Dixon-VIBE MR sequence). In such a scenario, PET might be the time limiting factor in PET/MR and arises the question of whether short PET data acquisition protocols in a whole-body multi-station context allow for reduced PET acquisition times, while providing adequate PET image quality and accurate PET quantification. This study showed, that 2 minutes PET acquisition per bed position is sufficient to provide accurate lesion detection and adequate image quality. Reducing the PET acquisition times further in a comparable setting may result in the loss of diagnostic information due to poor PET image quality [Lindemann et al., 2018].

4.3.2 Correlation with image quality determinants

Based on the evaluation of patient examples with consistent good or decreased image quality with reduced PET acquisition times, a implication of this study could be that a low BMI and a short time interval between radiotracer injection and PET/MRI examination are optimal conditions for obtaining high PET image quality even in short PET examinations. Considering factors like radiotracer half-time and count rate attenuation in tissue into account, these results are plausible. Tab. 3.6 also supports these conclusions. Besides the two key factors PET acquisition time and injected radiotracer activity, the BMI influences the PET image quality. Less injected radiotracer activity, long post injection times and a high BMI degrade the resulting PET image quality

by increasing the image noise and hence decreasing CNR and SNR values [Lindemann et al., 2018].

Also the interpretation of correlations between variance factors of some important biological image quality determinants yields that PET image quality is mainly influenced by two key factors: the PET acquisition time and the injected radiotracer activity (highly significant correlation, $p < 0.01$). The PET acquisition time and the applied radiotracer activity showed a positive correlation on CNR and SNR, while exhibiting a negative correlation on image noise. In contrast to that, the post injection time showed no significant correlation between any of the image quality parameters. In this study, if patients referred to a PET/MRI examination only or first underwent a clinically indicated PET/CT and subsequently an additional PET/MRI seems to have no impact on PET image quality. However, the post injection time in dependency from the half-life of the radiotracer, and thus the actual activity to the time of PET/MR acquisition, has an impact on PET image quality. With increased post injection times, the radiotracer decays and consequently, PET image quality decreased. The patients' BMI as a determinant also showed significant correlations on PET image quality. The BMI exhibited a negative correlation on SNR, while showing a positive correlation on image noise. A large BMI is often associated with overall large body dimensions, exceeding the constraints of the conventional MR FOV and causing AC problems as discussed in the section 4.1 above. The AC might partly compensate the image higher image noise in PET images, but there is a dependency of irradiated volume and scattered events. The larger the patients' volume (associated with a higher BMI) is, the higher the portion of scattered events is [Salomon et al., 2011]. Thus, PET image of patients with larger BMI tend to be noisier. According to the results of this present study, a higher BMI tends to reduce PET count statistics, and therefore decreases PET image quality. For patients with a higher BMI performing a 4 minute standard PET acquisition might be beneficial [Lindemann et al., 2018]. Patients with larger BMI might also benefit from additional post-processing reconstructions with noise correction functions or TOF information to reduce the PET image noise [Kueng et al., 2017; Rezaei et al., 2012].

4.3.3 Dose reduction

Another implication of this study might refer to radiotracer dose reduction in future whole-body ^{18}F -FDG PET/MRI examinations, without losses in PET image quality and accurate PET quantification. In general, two main key factors influence the PET image quality: PET acquisition time and applied radiotracer activity. In this context, the comparatively long PET/MRI acquisition times of current PET/MRI protocols

may be transformed into an advantage as longer PET acquisition times provide better count statistic, and thus increased PET image quality. Matching the prolonged MR protocol, PET acquisition time could be increased and may allow a decrease of injected radiotracer activity. In a systematic phantom study, Oehmigen et al. [2014] showed that reducing PET acquisition time by half provides equivalent PET image quality as doubling the PET acquisition time with half the applied radiotracer activity. In this context and according to the results of this present study, a reduction of radiotracer activity by a factor of two seems possible, when increasing the PET acquisition time from 2 to 4 minutes, while maintaining all other PET parameters and confounding factors [Lindemann et al., 2018].

5 Conclusions

The overall aim of this thesis was the development and evaluation of new methods and imaging concepts to extend the clinical application spectrum in PET/MRI. There are three technical main challenges in PET/MRI: 1. attenuation correction, 2. scatter correction and 3. fast imaging. Due to interactions with surrounding tissue, PET photons are attenuated and scattered on their way to the PET detector. To ensure best possible diagnostic image quality and accurate PET quantification, as well as lesion detection, AC and SC are essential steps in PET/MRI. A main limitation in MR-based AC in PET/MR is the limited MR FOV due to hardware restrictions, and thus truncation artifacts in the resulting AC-map. The SC relies on an accurate AC-map. Moreover, SC of radiotracers with a high specificity (e.g. ^{68}Ga -PSMA) may cause further problems with improper SC such as signal drop-outs (halo artifact) in prostate PET/MRI. The main disadvantage of PET/MRI over PET/CT are the prolonged acquisition times. In this context, the aim is the preparation of future fast PET/MR imaging protocols to increase patient comfort and throughput. Fast PET/MRI protocols run the risk of decreased PET image quality and quantification, thus the aim for fast PET/MRI is to shorten the MR acquisition time, while maintaining diagnostic information in PET/MRI.

In this thesis the implementation and evaluation of the MR-based truncation correction method HUGE to extend the MR FOV was presented. HUGE provides a robust and efficient method for truncation correction in whole-body PET/MRI and results in accurate body contouring. As a fully MR-based approach HUGE is independent of the choice of radiotracer. The robustness and the straightforward workflow presented in this thesis now allows for clinical use of HUGE truncation correction in various clinical applications in PET/MRI.

An accurate AC method is an essential precondition to provide quantitative PET data, especially for cardiac perfusion PET/MRI. Adding a bone model approach to the extended AC-map further improves MR-based AC in cardiac PET/MRI. The impact of improved AC including the presented HUGE truncation correction method and the additional bone segmentation was investigated in cardiac PET/MRI patient data and shows an overall gain in PET signal and a homogeneous PET signal distribution

over the entire myocardium. Thus, quantitative PET in cardiac PET/MRI could be enhanced, and thus might have clinical impact on cardiac PET/MRI and might be the basis of further research in quantitative PET/MRI.

The improved AC including HUGE truncation correction now also provides a proper base for SC algorithms especially in non-FDG radiotracers. PET/MR imaging of highly specific radiotracers like ^{68}Ga -PSMA is a challenge and depends on proper SC to ensure best possible diagnostic image quality and accurate PET qualification. An improved SC algorithm with un-renormalized absolute single Compton scatter simulation was tested in ^{68}Ga -PSMA PET/MRI of the prostate. The improved SC inherently reduces the halo artifact causing decreased PET signal around the urinary tract, and thus significantly increase PET image quality and quantification in PET/MRI of the prostate.

The results of the evaluation of improved SC exhibited a potential dependency between lesion visibility and PET acquisition time. In the context of fast PET/MRI it arises the question if the trend towards shorter PET/MRI examinations allows for adequate lesion detection. Therefore, the impact of reduced PET acquisition times on PET image quality and quantification on whole-body FDG PET/MRI was investigated. Despite the expected trend to lower PET image quality with shorter PET acquisition time, 2 minutes PET acquisition time per bed station is sufficient to provide accurate lesion detection and high image quality in a clinical PET/MRI setting. PET image quality is mainly affected by the two key factors acquisition time and applied radiotracer activity. Thus, another indication of this study might refer to radiotracer activity reduction in future PET/MRI without losses in in PET image quality and lesion visibility, when matching the PET acquisition times to the prolonged MR examination times.

6 Outlook

The results presented in this thesis provide various methods and imaging concepts for improving PET/MR hybrid imaging and PET quantification, and thus extend the range of clinical applications in PET/MRI. The implementation and evaluation of different methods including improved AC using HUGE truncation correction, improved SC using un-renormalized absolute scatter simulation and PET quantification in fast PET/MRI were published in peer review journals and are now available for the PET/MRI community. Especially the systematic development and testing of HUGE truncation correction combined with CTM has helped the manufacturer to reach product status for HUGE and this method for MR-based AC is now commercially implemented on the Siemens Biograph mMR PET/MRI system.

Further research might incorporate the extension of the MR FOV with HUGE not only in left-right direction, but also in vertical direction (anterior-posterior direction). Particularly the clinical application of PET/MRI in breast cancer imaging might benefit from further improvements in MR-based AC, as patients are raised in position on specific MR breast coils and AC-maps might be distorted at the patients' back. Moreover, the recently high interest in artificial intelligence combined with imaging modalities may yield further potential applications. For instance, the impact of radiotracer activity reduction on PET image quality in PET/MRI could be of particular interest for upcoming studies [Wang et al., 2018; Xiang et al., 2017]. Another approach of combining artificial intelligence and PET/MRI is the improvement of attenuation correction in PET/MRI. First studies on this topic deal with deep-learning networks, which synthesize pseudo-CT AC-maps based on the Dixon-VIBE images [Torrado-Carvajal et al., 2016, 2019].

Summary

For best possible positron emission tomography (PET) image quality and accurate PET quantification the correction for attenuated and scattered PET events is a main technical challenge in PET/magnetic resonance imaging (MRI). Thus, an aim of this thesis was the development and evaluation of new methods and imaging concepts for attenuation and scatter correction (AC, SC) to further extend the clinical application spectrum in PET/MRI. Another constrain in PET/MRI is the prolonged acquisition time. In the context of preparing future fast PET/MR protocols, another aim of this thesis was to analyse the impact of reduced PET acquisition times on PET image quality and quantification.

The first study of this thesis deals with the implementation and evaluation of a truncation correction method called HUGE (B_0 homogenisation using gradient enhancement) to extend the MR field-of-view, and thus to improve the AC in PET/MRI. HUGE was systematically tested in phantom measurements and 24 ^{18}F -FDG whole-body PET/MRI patient datasets. The mean AC-map volume was increased by 5.8 % and the mean standardized uptake value in the 24 primary lesions increased by 4.2 % over standard AC. The highest impact of HUGE on PET signal was quantified in lesions close to the truncated arms. HUGE provides a robust and efficient method for truncation correction and results in realistic body contouring. As a fully MR-based approach HUGE is independent of the choice of radiotracer.

The second study of this thesis deals with the clinical evaluation of improved AC including HUGE truncation correction and a bone model approach on 32 cardiac ^{18}F -FDG PET/MRI patient datasets. Polar plots exhibited a homogeneous gain of 6.1 % in PET signal distribution across the myocardium using HUGE and the bone model. Truncation artifacts in the standard AC-map tend to be stronger in patients with higher body mass index.

In the third study of this thesis the implementation of an improved SC method with un-renormalized absolute scaling was systematically tested in 100 ^{68}Ga -PSMA PET/MRI patients with prostate cancer. SC related artifacts (halo artifacts) could be inherently reduced using improved over standard SC, and thus, PET image quality could be increased. The mean standardized uptake value in 74 detected lesions increased by 12.4 % with improved SC. The mean standardized uptake value in the halo margin increased by 325.4 % with improved SC.

The fourth study of this thesis investigates the impact of reduced PET acquisition times on PET image quality and quantification on 51 ^{18}F -FDG whole-body PET/MRI patient datasets. Despite the expected trend to lower PET image quality with shorter PET acquisition time (increase in image noise and decrease of signal-to-noise-ratio), 2 minutes PET acquisition time per bed station is sufficient to provide accurate lesion detection and high image quality. 91 lesions were detected in the 4 to 2 minute PET time interval. 2 lesions were missed out in the 1 minute PET time interval due to poor image quality.

The results presented in this thesis provide various methods and imaging concepts for improving PET/MRI and PET quantification, and thus extend the range of clinical applications in PET/MRI.

Zusammenfassung

Eine technische Herausforderung der kombinierten Positronen-Emissions-Tomographie (PET)/Magnetresonanztomographie (MRT) stellt die Korrektur von abgeschwächten oder gestreuten PET-Photonen dar. Um bestmögliche PET-Bildqualität und korrekte PET-Quantifizierbarkeit zu gewährleisten, ist ein Ziel der vorliegenden Dissertation die Entwicklung und Evaluation neuer Methoden für die Schwächungs- und Streukorrektur (engl. attenuation correction AC, scatter correction SC) zur Erweiterung des klinischen Applikationsspektrums der PET/MR-Bildgebung. Eine weitere Einschränkung der PET/MRT ist die verhältnismäßig lange Akquisitionszeit. Um zukünftige schnellere PET/MR-Messprotokolle zu ermöglichen, ist ein weiteres Ziel dieser Dissertation, den Einfluss von kürzeren PET-Akquisitionszeiten auf die PET-Bildqualität und Quantifizierung zu analysieren.

In der ersten Studie wurde die Implementierung und Evaluation der Verzerrungskorrektur-Methode HUGE (engl. B_0 homogenisation using gradient enhancement) präsentiert, die das laterale MR-Sichtfeld erweitert und die AC in der PET/MRT verbessert. HUGE wurde systematisch in Phantom-Messungen und 24 Ganzkörper-PET/MR-Patientendaten untersucht. Der durchschnittliche Anstieg des AC-Volumens betrug 5.8 % und der durchschnittliche Anstieg in PET-Aktivität gegenüber der Standard-AC in den 24 detektierten Primär-Läsionen betrug 4.2 %. HUGE liefert eine robuste und effiziente Verzerrungskorrektur und als eine MR-basierte Methode ist HUGE unabhängig von der Wahl des Radiopharmazeutikums.

In der zweiten Studie wird der klinische Einfluss der verbesserten AC mit der Verzerrungskorrektur HUGE und einem zusätzlichen Knochenmodell anhand 32 kardialen PET/MR-Patientendaten analysiert. Polar-Diagramme zeigen einen gleichmäßig verteilte Erhöhung der PET-Aktivität über das gesamte Myokardium mit verbesserter AC. Verzerrungs-Artefakte in der Standard-AC sind tendenziell ausgeprägter mit steigendem Körpermassenindex der Patienten.

In der dritten Studie wurde die Implementierung einer verbesserten SC-Methode mit nicht-renormalisierter absoluter Skalierung in 100 PET/MR-Patienten mit Prostatakrebs untersucht. Die PET-Bildqualität konnte gegenüber der Standard-SC signifikant gesteigert und die SC-basierten Bildartefakte stark reduziert werden. Der durchschnittliche Anstieg der PET-Aktivität mit verbesserter SC in den 74 detektierten Läsionen betrug 12.4 % und in der Artefakt-Region sogar 325.4 %.

In der vierten Studie wurde der Einfluss der PET-Akquisitionszeit auf die PET-Bildqualität und Quantifizierung anhand 51 Ganzkörper-PET/MR-Patientendaten analysiert. Trotz des erwarteten Trends schlechterer PET-Bildqualität bei kürzeren PET-Akquisitionszeiten, sind 2 Minuten PET-Akquisition pro Bettstation ausreichend, um genaue Läsionsdetektion und ausreichende Bildqualität zu gewährleisten. Insgesamt konnten 91 Läsionen sowohl in der Standard-4-Minuten, als auch in der 2-Minuten PET-Rekonstruktion detektiert werden. Zwei Läsionen in der 1-Minuten PET-Rekonstruktion konnten wegen schlechter PET-Bildqualität nicht erkannt werden.

Die präsentierten Ergebnisse dieser Dissertation zeigen mehrere Methoden und Bildgebungskonzepte zur Verbesserung der PET/MR-Bildgebung und PET-Quantifizierung und erweitern somit das klinische Anwendungsspektrum in der PET/MR-Bildgebung.

References

- [1] Afshar-Oromieh, A., Avtzi, E., Giesel, F., Holland-Letz, T., Linhart, H., Eder, M., Eisenhut, M., Boxler, S., Hadaschik, B., Kratochwil, C., Weichert, W., Kopka, K., Debus, J., and Haberkorn, U. (2015):
The diagnostic value of PET/CT imaging with the (68)Ga-labelled PSMA ligand HBED-CC in the diagnosis of recurrent prostate cancer. *Eur. J. Nucl. Med. Mol. Imaging*, 42:197–209.
- [2] Afshar-Oromieh, A., Babich, J., Kratochwil, C., Giesel, F., Eisenhut, M., Kopka, K., and Haberkorn, U. (2016):
The rise of PSMA ligands for diagnosis and therapy of prostate cancer. *J. Nucl. Med.*, 57:79–89.
- [3] Afshar-Oromieh, A., Haberkorn, U., Schlemmer, H., Fenchel, M., Eder, M., Eisenhut, M., Hadaschik, B., Kopp-Schneider, A., and Röthke, M. (2014):
Comparison of PET/CT and PET/MRI hybrid systems using a 68Ga-labelled PSMA ligand for the diagnosis of recurrent prostate cancer: initial experience. *Eur. J. Nucl. Med. Mol. Imaging*, 41:887–897.
- [4] Afshar-Oromieh, A., Wolf, M., Haberkorn, U., Kachelrieß, M., Gnirs, R., Kopka, K., Schlemmer, H., and Freitag, M. (2017):
Effects of arm truncation on the appearance of the halo artifact in 68Ga-PSMA-11 (HBED-CC) PET/MRI. *Eur. J. Nucl. Med. Mol. Imaging*, 44:1636–1646.
- [5] Bakker, C., Moerland, M., Bhagwandien, R., and Beersma, R. (1992):
Analysis of machine-dependent and object-induced geometric distortion in 2DFT MR imaging. *Magn. Reson. Imaging*, 10:597–608.
- [6] Beyer, T., Lassen, M., Boellaard, R., Delso, G., Yaqub, M., Sattler, B., and Quick, H. (2016):
Investigating the state-of-the-art in whole-body MR-based attenuation correction: an intra-individual, inter-system, inventory study on three clinical PET/MR systems. *MAGMA*, 29:75–87.

- [7] Beyer, T. and Pichler, B. (2009):
A decade of combined imaging: from a PET attached to a CT to a PET inside an MR. *J. Nucl. Med.*, 36:Suppl. 1:1–2.
- [8] Beyer, T., Townsend, D., Brun, T., Kinahan, P., Charron, M., Roddy, R., Jerin, J., Young, J., Byars, L., and Nutt, R. (2000):
A combined PET/CT scanner for clinical oncology. *J. Nucl. Med.*, 41:1369–1379.
- [9] Bisdas, S., Ritz, R., Bender, B., Braun, C., Pfannenberger, C., Reimold, M., Naegele, T., and Ernemann, U. (2013):
Metabolic mapping of gliomas using hybrid MR-PET imaging: feasibility of the method and spatial distribution of metabolic changes. *Invest. Radiol.*, 48:295–301.
- [10] Blumhagen, J., Braun, H., Ladebeck, R., Fenchel, M., Faul, D., Scheffler, K., and Quick, H. (2014):
Field of view extension and truncation correction for MR-based human attenuation correction in simultaneous MR/PET imaging. *Med. Phys.*, 41:1–9.
- [11] Blumhagen, J., Ladebeck, R., Fenchel, M., and Scheffler, K. (2013):
MR-based field-of-view extension in MR/PET: B0 homogenization using gradient enhancement (HUGE). *Magn. Reson. Med.*, 70:1047–1057.
- [12] Boellaard, R., Hofman, M., Hoekstra, O., and Lammertsma, A. (2014):
Accurate PET/MR quantification using time of flight MLAA image reconstruction. *Mol. Imaging Biol.*, 16:469–477.
- [13] Boss, A., Bisdas, S., Kolb, A., Hofmann, M., Ernemann, U., Claussen, C., Pfannenberger, C., Pichler, B., Reimold, M., and Stegger, L. (2010):
Hybrid PET/MRI of intracranial masses: initial experiences and comparison to PET/CT. *J. Nucl. Med.*, 51:1198–1205.
- [14] Bouchelouche, K., Turkbey, B., Choyke, P., and Capala, J. (2010):
Imaging prostate cancer: an update on positron emission tomography and magnetic resonance imaging. *Curr. Urol. Rep.*, 11:180–190.
- [15] Braun, H., Ziegler, S., Lentschig, M., and Quick, H. (2014):
Implementation and performance evaluation of simultaneous PET/MR whole-body imaging with continuous table motion. *J. Nucl. Med.*, 55:161–168.
- [16] Braun, H., Ziegler, S., Paulus, D., and Quick, H. (2012):
Hybrid PET/MRI imaging with continuous table motion. *Med. Phys.*, 39:2735–2745.

- [17] Bravo, P., Bergmark, B., Vita, T., Taqueti, V., Gupta, A., Seidelmann, S., Christensen, T., Osborne, M., Shah, N., Ghosh, N., Hainer, J., Bibbo, C., Harrington, M., Costantino, F., Mehra, M., Dorbala, S., Blankstein, R., Desai, A., Stevenson, L., Givertz, M., and Di Carli, M. (2018): Diagnostic and prognostic value of myocardial blood flow quantification as non-invasive indicator of cardiac allograft vasculopathy. *Eur. Heart J.*, 39:316–323.
- [18] Carney, J., Townsend, D., Rappoport, V., and Bendriem, B. (2006): Method for transforming CT images for attenuation correction in PET/CT imaging. *Med. Phys.*, 33:976–983.
- [19] Catana, C., Wu, Y., Judenhofer, M., Qi, J., Pichler, B., and Cherry, S. (2006): Simultaneous acquisition of multislice PET and MR images: initial results with a MR-compatible PET scanner. *J. Nucl. Med.*, 47:1968–1976.
- [20] Cerqueira, M., Weissman, N., Dilsizian, V., Jacobs, A., Kaul, S., Laskey, W., Pennell, D., Rumberger, J., Ryan, T., and Verani, M. (2002): American Heart Association Writing Group on Myocardial Segmentation and Registration for Cardiac Imaging: Standardized myocardial segmentation and nomenclature for tomographic imaging of the heart. *American Heart Association, Circulation*, 105:539–542.
- [21] Delso, G., Fürst, S., Jakoby, B., Ladebeck, R., Ganter, C., Nekolla, S., Schwaiger, M., and Ziegler, S. (2011): Performance measurements of the Siemens mMR integrated whole-body PET/MR scanner. *J. Nucl. Med.*, 52:1914–1922.
- [22] Delso, G., Martinez-Möller, A., Bundschuh, R., Nekolla, S., and Ziegler, S. (2010): The effect of limited MR field of view in MR/PET attenuation correction. *Med. Phys.*, 37:2804–2812.
- [23] Drzezga, A., Souvatzoglou, M., Eiber, M., Beer, A., Fürst, S., Martinez-Möller, A., Nekolla, S., Ziegler, S., Ganter, C., Rummeny, E., and Schwaiger, M. (2012): First clinical experience with integrated whole-body PET/MR: comparison to PET/CT in patients with oncologic diagnoses. *J. Nucl. Med.*, 53:845–855.
- [24] Eiber, M., Herrmann, K., Calais, J., Hadaschik, B., Giesel, F., Hartenbach, M., Hope, T., Reiter, R., Maurer, T., Weber, W., and Fendler, W. (2018): Prostate cancer molecular imaging standardized evaluation (PROMISE): proposed miTNM classification for the interpretation of PSMA-ligand PET/CT. *J. Nucl. Med.*, 59:469–478.

- [25] Eiber, M., Martinez-Möller, A., Souvatzoglou, M., Holzapfel, K., Pickhard, A., Löffelbein, D., Santi, I., Rummeny, E., Ziegler, S., Schwaiger, M., Nekolla, S., and Beer, A. (2011):
Value of a Dixon-based MR/PET attenuation correction sequence for the localization and evaluation of PET-positive lesions. *Eur. J. Nucl. Med. Mol. Imaging*, 38:1691–1701.
- [26] Eiber, M., Nekolla, S., Maurer, T., Weirich, G., Wester, H., and Schwaiger, M. (2015a):
(68)Ga-PSMA PET/MR with multimodality image analysis for primary prostate cancer. *Abdom Imaging.*, 40:1769–1771.
- [27] Eiber, M., Weirich, G., Holzapfel, K., Souvatzoglou, M., Haller, B., Rauscher, I., Beer, A., Wester, H., Gschwend, J., Schwaiger, M., and Maurer, T. (2016):
Simultaneous 68Ga-PSMA HBED-CC PET/MRI improves the localization of primary prostate cancer. *Eur Urol.*, 70:829–836.
- [28] Eiber, M., Maurer, T., Souvatzoglou, M., Beer, A., Ruffani, A., Haller, B., Graner, F., Kübler, H., Haberkorn, U., Eisenhut, M., Wester, H., Gschwend, J., and Schwaiger, M. (2015b):
Evaluation of hybrid 68Ga-PSMA ligand PET/CT in 248 patients with biochemical recurrence after radical prostatectomy. *J. Nucl. Med.*, 56:668–674.
- [29] Gatidis, S., Würslin, C., Seith, F., Schäfer, J., la Fougère, C., Nikolaou, K., Schwenzer, N., and Schmidt, H. (2016):
Towards tracer dose reduction in PET studies: simulation of dose reduction by retrospective randomized undersampling of list-mode data. *Hell. J. Nucl. Med.*, 19:15–18.
- [30] Gückel, B., Gatidis, S., Enck, P., Schäfer, J., Bisdas, S., Pfannenber, C., and Schwenzer, N. (2015):
Patient comfort during positron emission tomography/magnetic resonance and positron emission tomography/computed tomography examinations: subjective assessments with visual analog scales. *Invest. Radiol.*, 50:726–732.
- [31] Grueneisen, J., Nagarajah, J., Buchbender, C., Hoffmann, O., Schaarschmidt, B., Poeppel, T., Forsting, M., Quick, H., Umutlu, L., and Kinner, S. (2015a):
Positron emission tomography/magnetic resonance imaging for local tumor staging in patients with primary breast cancer: a comparison with positron emission tomography/computed tomography and magnetic resonance imaging. *Invest. Radiol.*, 50:505–513.

- [32] Grueneisen, J., Sawicki, L., Schaarschmidt, B., Suntharalingam, S., von der Ropp, S., Wetter, A., Ruhlmann, V., Quick, H., Forsting, M., and Umutlu, L. (2016): Evaluation of a fast protocol for staging lymphoma patients with integrated PET/MRI. *PLoS One*, 11:1–13.
- [33] Grueneisen, J., Sawicki, L., Wetter, A., Kirchner, J., Kinner, S., Aktas, B., Forsting, M., Ruhlmann, V., and Umutlu, L. (2017): Evaluation of PET and MR datasets in integrated 18F-FDG PET/MRI: a comparison of different MR sequences for wholebody restaging of breast cancer patients. *Eur. J. Radiol.*, 89:14–19.
- [34] Grueneisen, J., Schaarschmidt, B., Heubner, M., Suntharalingam, S., Milk, I., Kinner, S., Heubner, A., Forsting, M., Lauenstein, T., Ruhlmann, V., and Umutlu, L. (2015b): Implementation of FAST-PET/MRI for whole-body staging of female patients with recurrent pelvic malignancies: a comparison to PET/CT. *Eur. J. Radiol.*, 84:2097–2102.
- [35] Hendrix, A. and Krempe, J. (2003): Magnete, Spins und Resonanzen - Eine Einführung in die Grundlagen der Magnetresonanztomographie. *Erlangen: Siemens AG*.
- [36] Heußner, T., Mann, P., Rank, C., Schäfer, M., Dimitrakopoulou-Strauss, A., Schlemmer, H., Hadaschik, B., Kopka, K., Bachert, P., Kachelrieß, M., and Freitag, M. (2017): Investigation of the halo-artifact in 68Ga-PSMA-11-PET/MRI. *PLoS One*, 12:1–19.
- [37] Huellner, M., de Galiza Barbosa, F., Husmann, L., Pietsch, C., Mader, C., Burger, I., Stolzmann, P., Delso, G., Frauenfelder, T., von Schulthess, G., and Veit-Haibach, P. (2016): TNM staging of non-small cell lung cancer: Comparison of PET/MR and PET/CT. *J. Nucl. Med.*, 57:21–26.
- [38] Hunter, C., Klein, R., Beanlands, R., and deKemp, R. (2016): Patient motion effects on the quantification of regional myocardial blood flow with dynamic PET imaging. *Med. Phys.*, 43:1829–1840.
- [39] Kinahan, P., Hasegawa, B., and Beyer, T. (2003): X-ray-based attenuation correction for positron emission tomography/computed tomography scanners. *Semin. Nucl. Med.*, 33:166–179.

- [40] Kirchner, J., Deuschl, C., Grueneisen, J., Herrmann, K., Forsting, M., Heusch, P., Antoch, G., and Umutlu, L. (2017a):
18F-FDG PET/MRI in patients suffering from lymphoma: how much MRI information is really needed? *Eur. J. Nucl. Med. Mol. Imaging*, 44:1005–1013.
- [41] Kirchner, J., Sawicki, L., Suntharalingam, S., Grueneisen, J., Ruhlmann, V., Aktas, B., Deuschl, C., Herrmann, K., Antoch, G., Forsting, M., and Umutlu, L. (2017b):
Whole-body staging of female patients with recurrent pelvic malignancies: ultra-fast 18F-FDG PET/MRI compared to 18F-FDG PET/CT and CT. *PLoS One*, 12:1–11.
- [42] Koesters, T., Friedman, K., Fenchel, M., Zhan, Y., Hermosillo, G., Babb, J., Jeleucu, I., Faul, D., Boada, F., and Shepherd, T. (2016):
Dixon sequence with superimposed model-based bone compartment provides highly accurate PET/MR attenuation correction of the brain. *J. Nucl. Med.*, 57:918–924.
- [43] Kueng, R., Driscoll, B., Manser, P., Fix, M., Stampanoni, M., and Keller, H. (2017):
Quantification of local image noise variation in PET images for standardization of noise-dependent analysis metrics. *Biomed. Phys. Engineering Express*, 3:1–12.
- [44] Lassen, M., Rasul, S., Beitzke, D., Stelzmüller, M., Cal-Gonzalez, J., Hacker, M., and Beyer, T. (2017):
Assessment of attenuation correction for myocardial PET imaging using combined PET/MRI. *J. Nucl. Cardiol.*, 10:1–12.
- [45] Lautamäki, R., George, R., Kitagawa, K., Higuchi, T., Merrill, J., Voicu, C., DiPaula, A., Nekolla, S., Lima, J., Lardo, A., and Bengel, F. (2009):
Rubidium-82 PET-CT for quantitative assessment of myocardial blood flow: validation in a canine model of coronary artery stenosis. *Eur. J. Nucl. Med. Mol. Imaging*, 36:576–586.
- [46] Lückerrath, K., Stuparu, A., Wei, L., Kim, W., Radu, C., Mona, C., Calais, J., Rettig, M., Reiter, R., Czernin, J., Slavik, R., Herrmann, K., Eiber, M., and Fendler, W. (2018):
Detection threshold and reproducibility of 68Ga-PSMA11 PET/CT in a mouse model of prostate cancer. *J. Nucl. Med.*, 59:1392–1397.

- [47] Lindemann, M., Guberina, N., Wetter, A., Fendler, W., Jakoby, B., and Quick, H. (2019a):
Improving ^{68}Ga -PSMA PET/MRI of the prostate with unrenormalized absolute scatter correction. *J. Nucl. Med.*, 11:1–7.
- [48] Lindemann, M., Nensa, F., and Quick, H. (2019b):
Impact of improved attenuation correction on ^{18}F -FDG PET/MR hybrid imaging of the heart. *PLoS One*, 14:1–16.
- [49] Lindemann, M., Oehmigen, M., Blumhagen, J., Gratz, M., and Quick, H. (2017):
MR-based truncation and attenuation correction in integrated PET/MR hybrid imaging using HUGE with continuous table motion. *Med. Phys.*, 44:4559–4572.
- [50] Lindemann, M., Stebner, V., Tschischka, A., Kirchner, J., Umutlu, L., and Quick, H. (2018):
Towards fast whole-body PET/MR: investigation of PET image quality versus reduced PET acquisition times. *PLoS One*, 13:1–15.
- [51] Lütje, S., Blex, S., Gomez, B., Schaarschmidt, B., Umutlu, L., Forsting, M., Jentzen, W., Bockisch, A., Poeppel, T., and Wetter, A. (2016):
Optimization of acquisition time of ^{68}Ga -PSMA-ligand PET/MRI in patients with local and metastatic prostate cancer. *PLoS One*, 11:1–14.
- [52] Martinez-Möller, A., Souvatzoglou, M., Delso, G., Bundschuh, R., Chefd’hotel, C., Ziegler, S., Navab, N., Schwaiger, M., and Nekolla, S. (2009):
Tissue classification as a potential approach for attenuation correction in whole-body PET/MRI: evaluation with PET/CT data. *J. Nucl. Med.*, 50:520–526.
- [53] Mehranian, A., Arabi, H., and Zaidi, H. (2016):
Vision 20/20: magnetic resonance imaging-guided attenuation correction in PET/MRI: challenges, solutions, and opportunities. *Med. Phys.*, 43:1130–1155.
- [54] Mehranian, A. and Zaidi, H. (2015):
Joint estimation of activity and attenuation in whole-body TOF PET/MRI using constrained gaussian mixture models. *IEEE Trans. Med. Imaging*, 34:1808–1821.
- [55] NEMA (2007):
National electrical manufacturers association (NEMA) standards publication NU 2–2007, performance measurements of positron emission tomographs. *Rosslyn, VA.*, page 26–33.

- [56] Nensa, F., Poeppel, T., Beiderwellen, K., Schelhorn, J., Mahabadi, A., Erbel, R., Heusch, P., Nassenstein, K., Bockisch, A., Forsting, M., and Schlosser, T. (2013): Hybrid PET/MR imaging of the heart: feasibility and initial results. *Radiology*, 268:366–373.
- [57] Nesterov, S., Han, C., Mäki, M., Kajander, S., Naum, A., Helenius, H., Lisinen, I., Ukkonen, H., Pietilä, M., Joutsiniemi, E., and Knuuti, J. (2009): Myocardial perfusion quantitation with ^{15}O -labelled water PET: high reproducibility of the new cardiac analysis software (Carimas). *Eur. J. Nucl. Med. Mol. Imaging*, 36:1594–1602.
- [58] Noto, B., Büther, F., Auf der Springe, K., Avramovic, N., Heindel, W., Schäfers, M., Allkemper, T., and Stegger, L. (2017): Impact of PET acquisition durations on image quality and lesion detectability in whole-body ^{68}Ga -PSMA PET-MRI. *EJNMMI Res.*, 7:1–12.
- [59] Nuyts, J., Dupont, P., Stroobants, S., Beninck, R., Mortelmans, L., and Suetens, P. (1999): Simultaneous maximum a posteriori reconstruction of attenuation and activity distributions from emission sonograms. *IEEE Trans. Med. Imaging*, 18:393–403.
- [60] Nuyts, J., Michel, C., Fenchel, M., Bal, G., and Watson, C. (2010): Completion of a truncated attenuation image from the attenuated PET emission data. *IEEE Nucl. Sci. Symp. Conf. Record.*, page 2123–2127.
- [61] O’Doherty, J., Chalampalakis, Z., Schleyer, P., Nazir, M., Chiribiri, A., and Marsden, P. (2017): The effect of high count rates on cardiac perfusion quantification in a simultaneous PET-MR system using a cardiac perfusion phantom. *EJNMMI Phys.*, 4:1–15.
- [62] Oehmigen, M., Lindemann, M., Gratz, M., Kirchner, J., Ruhlmann, V., Umutlu, L., Blumhagen, J., Fenchel, M., and Quick, H. (2017): Impact of improved attenuation correction featuring a bone atlas and truncation correction on PET quantification in whole-body PET/MR. *Eur. J. Nucl. Med. Mol. Imaging*, 45:642–653.
- [63] Oehmigen, M., Ziegler, S., Jakoby, B., Georgi, J., Paulus, D., and Quick, H. (2014): Radiotracer dose reduction in integrated PET/MR: implications from national electrical manufacturers association phantom studies. *J. Nucl. Med.*, 55:1361–1367.

- [64] Paulus, D., Oehmigen, M., Grüneisen, J., Umutlu, L., and Quick, H. (2016): Wholebody hybrid imaging concept for the integration of PET/MR into radiation therapy treatment planning. *Med. Phys. Biol.*, 61:3504–3520.
- [65] Paulus, D., Quick, H., Geppert, C., Fenchel, M., Zhan, Y., Hermosillo, G., Faul, D., Boada, F., Friedman, K., and Koesters, T. (2015): Whole-body PET/MR imaging: quantitative evaluation of a novel model-based MR attenuation correction method including bone. *J. Nucl. Med.*, 56:1061–1066.
- [66] Paulus, D., Thorwath, D., Schmidt, H., and Quick, H. (2014): Towards integration of PET/MR hybrid imaging into radiation therapy treatment planning. *Med. Phys.*, 41:1–14.
- [67] Pichler, B., Judenhofer, M., Catana, C., Walton, J., Kneilling, M., Nutt, R., Siegel, S., Claussen, C., and Cherry, S. (2006): Performance test of an LSO-APD detector in a 7-T MRI scanner for simultaneous PET/MRI. *J. Nucl. Med.*, 47:639–647.
- [68] Pichler, B., Judenhofer, M., and Wehrl, H. (2008a): PET/MRI hybrid imaging: devices and initial results. *Eur. Radiol.*, 18:1077–1086.
- [69] Pichler, B., Kolb, A., Nagele, T., and Schlemmer, H. (2010): PET/MRI: paving the way for the next generation of clinical multimodality imaging applications. *J. Nucl. Med.*, 51:333–336.
- [70] Pichler, B., Wehrl, H., Kolb, A., and Judenhofer, M. (2008b): Positron emission tomography/ magnetic resonance imaging: the next generation of multimodality imaging? *Semin. Nucl. Med.*, 38:199–208.
- [71] Quick, H. (2014): Integrated PET/MR. *J. Magn. Reson. Imaging*, 39:243–258.
- [72] Quick, H., von Gall, C., Zeilinger, M., Wiesmüller, M., Braun, H., Ziegler, S., Kuwert, T., Uder, M., Dörfler, A., Kalender, W., and Lell, M. (2013): Integrated whole-body PET/MR hybrid imaging: clinical experience. *Invest. Radiol.*, 48:280–289.
- [73] Rauscher, I., Maurer, T., Fendler, W., Sommer, W., Schwaiger, M., and Eiber, M. (2016): (68)Ga-PSMA ligand PET/CT in patients with prostate cancer: how we review and report. *Cancer Imaging*, 16:1–10.

- [74] Rezaei, A., Defrise, M., Bal, G., Michel, C., Conti, M., Watson, C., and Nuyts, J. (2012):
Simultaneous reconstruction of activity and attenuation in time-of-flight PET. *IEEE Trans. Med. Imaging*, 31:2224–2233.
- [75] Rischpler, C., Nekolla, S., Dregely, I., and Schwaiger, M. (2013):
Hybrid PET/MR imaging of the heart: potential, initial experiences, and future prospects. *J. Nucl. Med.*, 54:402–415.
- [76] Rischpler, C., Park, M., Fung, G., Javadi, M., Tsui, B., and Higuchi, T. (2012):
Advances in PET myocardial perfusion imaging: F-18 labeled tracers. *Ann. Nucl. Med.*, 26:1–6.
- [77] Rowe, S., Pienta, K., Pomper, M., and Gorin, M. (2018):
Proposal for a structured reporting system for prostate-specific membrane antigen-targeted PET imaging: PSMA-RADS version 1.0. *J. Nucl. Med.*, 59:479–485.
- [78] Saha, G. (2005):
Basics of PET imaging: Physics, chemistry and regulations. *Berlin: Springer-Verlag*.
- [79] Salomon, A., Goedicke, A., Schweizer, B., Aach, T., and Schulz, V. (2011):
Simultaneous reconstruction of activity and attenuation for PET/MR. *IEEE Trans. Med. Imaging*, 30:804–813.
- [80] Samarin, A., Burger, C., Wollenweber, S., Crook, D., Burger, I., Schmid, D., von Schulthess, G., and Kuhn, F. (2012):
PET/MR imaging of bone lesions - implications for PET quantification from imperfect attenuation correction. *Eur. J. Nucl. Med. Mol. Imaging*, 39:1154–1160.
- [81] Schaarschmidt, B., Buchbender, C., Gomez, B., Rubbert, C., Hild, F., Köhler, J., Grueneisen, J., Reis, H., Ruhlmann, V., Wetter, A., Quick, H., Antoch, G., and Heusch, P. (2015):
Thoracic staging of non-small-cell lung cancer using integrated (18)F-FDG PET/MR imaging: diagnostic value of different MR sequences. *Eur. J. Nucl. Med. Mol. Imaging*, 42:1257–1267.
- [82] Schindler, T. (2016):
Myocardial blood flow: putting it into clinical perspective. *J. Nucl. Cardiol.*, 23:1056–1071.

- [83] Schwarzenboeck, S., Rauscher, I., Bluemel, C., Fendler, W., Rowe, S., Pomper, M., Afshar-Oromieh, A., Herrmann, K., and Eiber, M. (2017): PSMA ligands for PET imaging of prostate cancer. *J. Nucl. Med.*, 58:1545–1552.
- [84] Schwenck, J., Rempp, H., Reischl, G., Kruck, S., Stenzl, A., Nikolaou, K., Pfannenberger, C., and la Fougère, C. (2017): Comparison of ^{68}Ga -labelled PSMA-11 and ^{11}C choline in the detection of prostate cancer metastases by PET/CT. *Eur. J. Nucl. Med. Mol. Imaging*, 44:92–101.
- [85] Schwenzer, N., Schmidt, H., and Claussen, C. (2012): Whole-body MR/PET: applications in abdominal imaging. *Abdom. Imaging*, 37:20–28.
- [86] Schwenzer, N., Seith, F., Gatidis, S., Brendle, C., Schmidt, H., Pfannenberger, C., la Fougère, C., Nikolaou, K., and Schraml, C. (2016): Diagnosing lung nodules on oncologic MR/PET imaging: comparison of fast T1-weighted sequences and influence of image acquisition in inspiration and expiration breath-hold. *Korean J. Radiol.*, 17:684–694.
- [87] Seith, F., Schmidt, H., Kunz, J., Küstner, T., Gatidis, S., Nikolaou, K., la Fougère, C., and Schwenzer, N. (2017): Simulation of tracer dose reduction in ^{18}F -FDG-positron emission tomography/magnetic resonance imaging (PET/MRI): effects on oncologic reading, image quality and artifacts. *J. Nucl. Med.*, 58:1699–1705.
- [88] Tabouret-Viaud, C., Botsikas, D., Delattre, B., Mainta, I., Amzalag, G., Rager, O., Vinh-Hung, V., Miralbell, R., and Ratib, O. (2015): PET/MR in breast cancer. *Semin. Nucl. Med.*, 45:304–321.
- [89] Tanner, S., Finnigan, D., Khoo, V., Mayles, P., Dearnaley, D., and Leach, M. (2000): Radiotherapy planning of the pelvis using distortion corrected mr images: the removal of system distortions. *Med. Phys. Biol.*, 48:2117–2132.
- [90] Torrado-Carvajal, A., Herraiz, J., Alcaín, E., Montemayor, A., Garcia-Canamaque, L., Hernandez-Tamames, J., Rozenholc, Y., and Malpica, N. (2016): Fast patchbased pseudo-CT synthesis from T1-weighted MR images for PET/MR attenuation correction in brain studies. *J. Nucl. Med.*, 57:136–143.

- [91] Torrado-Carvajal, A., Vera-Olmos, J., Izquierdo-Garcia, D., Catalano, O., Morales, M., Margolin, J., Soricelli, A., Salvatore, M., Malpica, N., and Catana, C. (2019):
Dixon- VIBE deep learning (DIVIDE) pseudo-CT synthesis for pelvis PET/MR attenuation correction. *J. Nucl. Med.*, 60:429–435.
- [92] Townsend, D. (2004):
Physical principles and technology of clinical PET imaging. *Ann. Acad. Med. Singap.*, 33:133–145.
- [93] Wang, Y., Yu, B., Wang, L., Zu, C., Lalush, D., Lin, W., Wu, X., Zhou, J., Shen, D., and Zhou, L. (2018):
3D conditional generative adversarial networks for high-quality PET image estimation at low dose. *Neuroimage*, 174:550–562.
- [94] Watson, C. (2000):
New, faster, image-based scatter correction for 3-D PET. *IEEE Trans. Nucl. Sci.*, 47:1587–1594.
- [95] Watson, C., Hayden, C., Casey, M., Hamill, J., and Bendriem, B. (2008):
Prompt gamma correction for improved quantification in 82Rb PET. *J. Nucl. Med.*, 49:64P.
- [96] Watson, C., Hu, J., and Zhou, C. (2018):
Extension of the SSS PET scatter correction algorithm to include double scatter. *IEEE Nucl. Sci. Symp. Medic. Conf. Record*, pages 1–4.
- [97] Watson, C., Newport, D., Casey, M., Dekemp, R., Beanlands, R., and Schmand, M. (1997):
Evaluation of simulation-based scatter correction for 3-D PET cardiac imaging. *IEEE Trans. Nucl. Sci.*, 44:90–97.
- [98] Wetter, A., Lipponer, C., Nensa, F., Beiderwellen, K., Olbricht, T., Rübber, H., Bockisch, A., Schlosser, T., Heusner, T., and Lauenstein, T. (2013):
Simultaneous 18F choline positron emission tomography/magnetic resonance imaging of the prostate: initial results. *Invest. Radiol.*, 48:256–262.
- [99] Wiesmüller, M., Quick, H., Navalpakkam, B., Lell, M., Uder, M., Ritt, P., Schmidt, D., Beck, M., Kuwert, T., and von Gall, C. (2013):
Comparison of lesion detection and quantitation of tracer uptake between PET from a simultaneously acquiring wholebody PET/MR hybrid scanner and PET from PET/CT. *Eur. J. Nucl. Med. Mol. Imaging*, 40:12–21.

- [100] Xiang, L., Qiao, Y., Nie, D., An, L., Wang, Q., and Shen, D. (2017):
Deep autocontext convolutional neural networks for standard-dose PET image
estimation from low-dose PET/MRI. *Neurocomputing*, 267:406–416.

List of abbreviations

$^{18}\text{F-FDG}$	18-fluor-labeled fluorodeoxyglucose
$^{68}\text{Ga-PSMA}$	68-gallium-labeled prostate-specific membrane antigen
^{124}I	124-iodine
AC	attenuation correction
ACF	attenuation correction factor
B_0	static main magnetic field
BMI	body mass index
CNR	contrast-to-noise-ratio
CT	computed tomography
CTM	continuous table movement
FA	flip angle
FOV	field-of-view
HASTE	half Fourier acquisition single shot turbo spin-echo
HUGE	B_0 homogenisation using gradient enhancement
IQ	image quality
IQS	image quality score
LAC	linear attenuation coefficient
MLAA	maximum likelihood estimation of activity and attenuation
MRI	magnetic resonance imaging
NAC	non attenuation corrected

OBR	organ-to-background-ratio
OP-OSEM	ordinary Poisson ordered-subsets expectation maximization
PET	positron emission tomography
RO	read-out
ROI	region-of-interest
SC	scatter correction
SD	standard deviation
SNR	signal-to-noise-ratio
SSS	single Compton scatter simulation
SUV	standardized uptake value
T1	spin-lattice relaxation time
T2	spin-spin relaxation time
TE	echo time
TOF	time-of-flight
TR	repetition time
VIBE	volumetric interpolated breath-hold examination
VOI	volume-of-interest

List of figures

1.1	Drawing of different detected coincidences.	8
1.2	Whole-body PET/MRI patient example.	9
1.3	Dixon-VIBE attenuation correction map and HUGE MR raw data. . .	12
1.4	⁶⁸ Ga-PSMA PET images of a patient example without and with scatter correction.	15
1.5	Flow chart of simultaneous multi-step PET/MR data acquisition. . . .	16
2.1	Flow chart of the main steps for an extended MR-based attenuation correction map	19
2.2	Phantom setup for HUGE measurements.	20
2.3	Attenuation correction maps, PET data in short axis view and polar plots of two patient examples.	24
2.4	Quantitative and qualitative impact of improved scatter correction. . .	27
3.1	Extended attenuation correction maps for the phantom setup and the quantitative impact on PET data.	30
3.2	Attenuation correction maps of three patients with a range of different BMI.	32
3.3	Volume deviations of the patients' arms in different attenuation correction maps compared to arms segmented in the non-AC PET data. . . .	33
3.4	Quantitative impact of truncation correction with the HUGE and the MLAA method.	34
3.5	Comparison between HUGE and MLAA truncation correction on AC map volume and SUV measurements.	35
3.6	Relative difference images in PET data of two patient examples.	36
3.7	Attenuation correction maps of a non-FDG patient example.	38
3.8	Statistical analysis of field-of-view extension and bone segmentation on global PET signal in the myocardium.	40
3.9	Relative difference polar plots between improved and standard Dixon-VIBE attenuation correction.	41
3.10	Different attenuation correction map artifacts.	42

3.11 Quantitative impact of a bone artifact in the attenuation correction map of a patient example.	43
3.12 Relative differences in SUV over all patients in different VOIs.	46
3.13 Quantitative impact of improved scatter correction in a patient example.	47
3.14 Evaluation of the impact of PET acquisition time on lesion visibility. .	48
3.15 Patient example of consistently good image quality.	51
3.16 Patient example of decreasing image quality.	52

List of tables

2.1	Statistically relevant data of the patient population for HUGE evaluation.	22
3.1	Comparison of the quantitative impact of HUGE and MLAA truncation correction compared to standard Dixon-VIBE attenuation correction. .	37
3.2	SUV measurements in a non-FDG patient example	38
3.3	Classification of different attenuation correction map artifacts.	42
3.4	Rating of the halo artifact.	44
3.5	Lesion characterization and image quality analysis for different PET list-mode data reconstruction intervals.	50
3.6	Quantitative impact of different determinants on PET image quality for different PET time intervals.	54
3.7	Correlation coefficients between the image quality determinants and PET image quality parameters.	55

Acknowledgements

I would like to thank...

... my advisor Prof. Dr. Harald Quick for giving me the opportunity to do my PhD in the exiting field of PET/MR hybrid imaging and his ongoing guidance and support. His door and email inbox was constantly open for questions and discussions.

... my college/desk neighbour Mark Oehmigen for being my “fellow sufferer” and steady discussion partner, for having a lot of patience with me and for joining me on daily coffee break.

... my favourite part-time college Marcel Gratz for guiding me through some nerve-racking IT stuff, for some excellent music suggestions and for being a steady discussion parter for work-related and not so much work-related topics.

... the Department of Nuclear Medicine and the Department of Diagnostic and Interventional Radiology and Neuroradiology of the University Hospital Essen for helping me out with the clinical assessment of my studies.

... our collaboration partner Siemens Healthcare for their technical support, new ideas and their time for discussion.

And last but not least, my sincere thanks go to my mum for her ongoing support in every aspect of my life and her patience with me. Her encouragement helped me to finish this dissertation thesis.

Curriculum vitæ

Der Lebenslauf ist in der Online-Version aus Gründen des Datenschutzes nicht enthalten.